

## ABSTRACT

MCCLURE, CHRISTINA DEVINE. Atomic Layer Deposition for the Modification of Polymers and Carbon Nanotubes. (Under the direction of Gregory N. Parsons).

Nanoscale materials such as polymer nanofibers and carbon nanotubes (CNTs) have unique mechanical, electrical and chemical properties. Polymer nanofibers and carbon nanotubes are widely studied for their use in filtration, tissue scaffolding, as catalyst supports, and are also used together as composite materials for reinforcement and increased conductivity among other uses. The functionalization of these materials is sometimes required to further enhance their properties for purposes such as sensor applications, increased biocompatibility, chemical resistance, and improved mechanical performance.

A variety of methods have been used to functionalize polymers and carbon nanotubes including wet chemical methods and vapor deposition methods. In this study, we focus on using atomic layer deposition (ALD) for the deposition of thin metal oxide films. Atomic layer deposition is a vapor phase method utilizing sequential self-limiting reactions to deposit uniform films with near monolayer control over thickness. The use of ALD with polymers and carbon nanotubes has been widely studied to understand growth mechanisms on these substrates. The work presented investigates unique methods of coating and containing carbon nanotubes for ALD which can also be used for other nanopowder materials. We also explore the effect of these thin films on the bulk mechanical properties of polymer films and nanofibers including the effect the substrate chemistry, precursor chemistry, and processing parameters. A key conclusion from our studies is that the ALD processing conditions and substrate chemistry have a great impact on the surface and subsurface growth of the resulting film and the mechanical performance of the substrate.

© Copyright 2013 Christina Devine McClure

All Rights Reserved

Atomic Layer Deposition for the Modification of Polymers and Carbon Nanotubes

by  
Christina Devine McClure

A dissertation submitted to the Graduate Faculty of  
North Carolina State University  
in partial fulfillment of the  
requirements for the degree of  
Doctor of Philosophy

Chemical Engineering

Raleigh, North Carolina

2013

APPROVED BY:

---

Dr. Gregory N. Parsons  
Committee Chair

---

Dr. Saad Khan

---

Dr. Jan Genzer

---

Dr. James Bonner

## **DEDICATION**

To my loving family and amazing husband, without your support  
and guidance this would not be possible.

## **BIOGRAPHY**

Christina McClure was born in Cedar Rapids, Iowa to Bill and Patty Devine. She graduated from George Washington High School in 2002. After graduation she attended the University of Iowa and decided to pursue Chemical Engineering as a major in 2004. She graduated in spring of 2008 and began her graduate work at North Carolina State University in the fall.

## ACKNOWLEDGMENTS

I would first like to acknowledge my advisor Dr. Gregory Parsons for all of his support and guidance. His expansive knowledge has been invaluable to my research and education. I am also thankful to my committee members Dr. Saad Khan, Dr. Jan Genzer, and Dr. James Bonner for their insight and advice.

I would like to acknowledge past and present group members. Specifically, Dr. Jesse Jur and Dr. Christopher Oldham for all of their advice, guidance, and support throughout my research studies. Past group members, Dr. Qing Peng, Dr. Joseph Spagnola, and Dr. Bo Gong were very helpful and instructive in getting acquainted with research and atomic layer deposition. I also want to thank current member Do Han Kim, Kyoungmi Lee, Will Sweet, Berc Kalanyan, Moataz Mousa, Sarah Atanasov, Junjie Zhao, Paul Lemaire, Zack Mundy and Erinn Dandley for contributing to a fun and productive work atmosphere.

I also must acknowledge all of my family and friends for all of their support. I am thankful to my family for their unwavering support. I am so thankful to my husband, Josh for being my best friend and making me laugh when I need it most and for his overall love of science. I am also thankful for my lunch buddy, Alina Highman. Her positive attitude and spunky attitude have been helped make graduate school so much fun. I am thankful to Heath Johnson for his amazing raps and sense of humor, to Sara Arvidson for her education in all things culinary and mentorship, to Christina Tang for her dry sense of humor and knowledge on absolutely everything, and to Stephanie Lam for her optimism and friendship. Finally, to Will and Phil, I am forever thankful the introduction to “bear dances”.

## TABLE OF CONTENTS

<b>LIST OF TABLES .....</b>	<b>x</b>
<b>LIST OF FIGURES .....</b>	<b>xi</b>
<b>CHAPTER 1. Introduction .....</b>	<b>1</b>
1.1 Sol-Gel .....	2
1.2 Layer by Layer Growth.....	3
1.3 Electroless Plating.....	4
1.4 Liquid Phase Deposition .....	5
1.5 Physical Vapor Deposition .....	7
1.6 Chemical Vapor Deposition.....	8
1.7 Atomic Layer Deposition.....	9
1.8 Atomic Layer Deposition on Polymers.....	12
1.9 Carbon Nanotubes.....	15
1.10 ALD on Carbon Nanotubes .....	15
1.11 Brief Overview of Work .....	18
References.....	23
<b>CHAPTER 2. Experimental Tools .....</b>	<b>36</b>
2.1 Atomic Layer Deposition.....	36
2.2 Material Preparation.....	37
2.2.1 Electrospinning .....	37
2.2.2 Melt Pressing .....	37
2.2.3 Carbon Nanotube Preparation.....	38
2.3 Mechanical Testing.....	39
2.3.1 Instron Tensile Testing .....	39
2.3.2 Nanoindentation by Atomic Force Microscopy.....	39
2.4 Materials Characterization .....	40
2.4.1 Fourier Transform Infrared Spectroscopy .....	40
2.4.2 X-Ray Photoelectron Spectroscopy .....	40
2.4.3 Transmission Electron Microscopy .....	40
2.4.4 Scanning Electron Microscopy .....	41

2.4.5 Ellipsometry.....	41
References.....	44
<b>CHAPTER 3. Overview of Key Results of the Dissertation.....</b>	<b>45</b>
3.1 Fiber Containment for Improved Laboratory Handling and Uniform Nanocoating of Milligram Quantities of Carbon Nanotubes by Atomic Layer Deposition.....	45
3.2 Atomic Layer Deposition of Zinc Oxide on Multiwall Carbon Nanotubes.....	46
3.3 Large Effect of Titanium Precursor on Surface Reactivity and Mechanical Strength of Electrospun Nanofibers Coated with TiO <sub>2</sub> by Atomic Layer Deposition.....	48
3.4. AFM Nanoindentation on ALD Coated Electrospun Nylon Nanofibers.....	49
3.5 Effect of ALD Processing Parameters on Film Growth and Mechanical Properties of Polymer Films.....	50
<b>CHAPTER 4. Fiber Encapsulation for Improved Laboratory Handling and Uniform Nanocoating of Milligram Quantities of Carbon Nanotubes by Atomic Layer Deposition.....</b>	<b>61</b>
Abstract.....	62
4.1 Introduction.....	63
4.2 Experimental Methods.....	66
4.2.1 Multiwall Carbon Nanotube Preparation and Containment for ALD Coating.....	66
4.2.2 Preparation of Nanotube Control Samples.....	67
4.2.3 Porosity of the Fiber Mats.....	68
4.2.4 ALD Film Coating.....	69
4.2.5 Characterization of Coated CNTs.....	70
4.3 Results.....	72
4.3.1 Fiber Bundle Method.....	72
4.3.2 Fiber Basket Method.....	73
4.3.3 ALD on MWNTs on TEM Grids.....	76
4.3.4 ALD on Other Types of CNTs.....	77
4.4 Discussion and Conclusions.....	78
Acknowledgments.....	80
References.....	94
<b>CHAPTER 5. Atomic Layer Deposition of Zinc Oxide on Multiwall Carbon Nanotubes.....</b>	<b>97</b>

Abstract.....	97
5.1 Introduction.....	98
5.2 Experimental Methods.....	99
5.2.1 Multiwall Carbon Nanotube Preparation and Containment for ALD Coating .....	99
5.2.2 Preparation of Nanotube Control Samples .....	100
5.2.3 ALD Film Coating .....	100
5.2.4 Characterization of Coated CNTs.....	101
5.3 Results.....	101
5.4 Discussion.....	103
5.5 Conclusion .....	105
References.....	112
<b>CHAPTER 6. Large Effect of Titanium Precursor on Surface Reactivity and Mechanical Strength of Electrospun Nanofibers Coated with TiO<sub>2</sub> by Atomic Layer Deposition .....</b>	<b>115</b>
Abstract.....	116
6.1 Introduction.....	117
6.2 Experimental.....	118
6.2.1 Electrospun polymer fiber preparation .....	118
6.2.2 Fiber treatment and surface modification .....	119
6.2.3 Morphology and chemical characterization.....	120
6.2.4 Mechanical Analysis.....	122
6.3 Results.....	123
6.3.1 Nanofiber Morphology .....	123
6.3.2 FTIR.....	124
6.3.3 X-ray Photoelectron Spectroscopy .....	125
6.3.4 Mechanical Response.....	126
6.4 Discussion.....	129
6.5 Conclusion .....	131
Acknowledgments.....	132
References.....	143

<b>Chapter 7. Determination of Elastic Modulus of Electrospun Nylon 6 Nanofibers Coated by Atomic Layer Deposition using AFM Nanoindentation .....</b>	<b>146</b>
Abstract .....	146
7.1 Introduction.....	147
7.2 Experimental.....	148
7.2.1 Materials and Electrospinning .....	148
7.2.2 Nanofiber Functionalization .....	149
7.2.3 Atomic Force Microscopy .....	149
7.3 Results.....	150
7.4 Conclusions.....	154
References.....	160
<b>Chapter 8. Modulation of Bulk Mechanical Properties of Polymers by Vapor-Phase Treatments using Atomic Layer Deposition of Al<sub>2</sub>O<sub>3</sub> and TiO<sub>2</sub>.....</b>	<b>164</b>
Abstract.....	164
8.1 Introduction.....	165
8.2 Experimental.....	167
8.2.1 Melt-Pressing.....	167
8.2.2 Atomic Layer Deposition.....	167
8.2.3 Instron Testing .....	168
8.2.4 Water Testing.....	169
8.3 Results.....	169
8.3.1 TEM.....	169
8.3.2 FTIR.....	172
8.3.3 Effect on Mechanical Data.....	173
8.3.4 Effect of Molecular Weight .....	176
8.3.5 Water Resistance.....	179
8.4 Conclusion .....	180
References.....	195
<b>APPENDIX.....</b>	<b>198</b>
<b>APPENDIX A1. Co-Authored Works.....</b>	<b>199</b>

A1.1 “Sequential Vapor Infiltration of Metal Oxides into Sacrificial Polyester Fibers: Shape Replication and Controlled Porosity of Microporous/Mesoporous Oxide Monoliths” .....	199
A1.2 “Stable anatase TiO <sub>2</sub> coating on quartz fibers by atomic layer deposition for photoactive light-scattering in dye-sensitized solar cells” .....	199
A1.3 “Oxygen Electroreduction on Ti- and Fe-Containing Carbon Fibers” .....	199
A1.4 “Solid Electrolyte Interphase on Lithium-ion Carbon Nanofiber Electrodes by Atomic and Molecular Layer Deposition” .....	199
A1.5 “Atomic Layer Deposition Coating of Multi-Walled Carbon Nanotubes with Aluminum Oxide Alters Innate Immune Responses of Human Macrophages In vitro” ..	199
References .....	200

## LIST OF TABLES

<b>Table 3.1:</b> Film thicknesses measured on polymer samples after 200 cycles of either ALD or ALD-Holds as measured by TEM and the film thicknesses on the silicon wafer monitor measured by ellipsometry. ....	60
<b>Table 6.1:</b> Dosing and purging times used to coat the nylon nanofibers samples for aluminum oxide, zinc oxide, and titanium dioxide coatings. ....	135
<b>Table 8.1:</b> Film thicknesses measured on polymer samples after 200 cycles of either ALD or ALD-holds as measured by TEM and the film thicknesses on the silicon wafer monitor measured by ellipsometry. ....	184
<b>Table 8.2:</b> FTIR peak assignments for the P55D spectra shown in Figure 8.3.....	186
<b>Table 8.3:</b> Mass increase for high molecular PEO samples after treatment with ALD and ~30 minutes after water resistance testing. ....	193

## LIST OF FIGURES

<b>Figure 1.1:</b> Reaction sequence for one ALD cycle of TMA/H <sub>2</sub> O for the deposition of aluminum oxide. ....	19
<b>Figure 1.2:</b> Different types of substrate dependent ALD growth models.....	20
<b>Figure 1.3:</b> Diagram of the various graphene derivatives, C <sub>60</sub> , carbon nanotubes and graphite <sup>70</sup> .....	21
<b>Figure 1.4:</b> Schematic of a fluidized bed reactor used to coat nanopowders <sup>80</sup> .....	22
<b>Figure 2.1:</b> Schematic of hot-walled viscous flow reactor used for ALD of metal oxide thin films. ....	42
<b>Figure 2.2:</b> Growth rate of ALD deposited zinc oxide, aluminum oxide, and titanium dioxide via TiCl <sub>4</sub> or TIP thin films on silicon at 105°C. For all precursors the growth is linear as is expected for ALD. ....	43
<b>Figure 3.1:</b> TEM images of MWNTs coated with a) 25; b) 50; c) 100; and d) 200 cycles Al <sub>2</sub> O <sub>3</sub> ALD at 90°C using the cotton wrapped basket method. The coating thickness increased linearly with cycle number. Several uncoated or broken ends were observed as shown in panel (d). In other images (not shown), the number of visible broken ends increases as the coating thickness increases. ....	53
<b>Figure 3.2:</b> Graph comparing ALD growth on Si wafers and MWNTs where the substrates (Si and nanotubes) are encased in cotton fiber baskets. The plot also includes thickness measured on silicon when the substrate is directly wrapped in cotton (without the basket) (labeled “Si / cotton”) and when no fiber containment is present (labeled “Si / open”). The growth increases linearly with cycle number at about the same rate observed for fibers encased in polypropylene. The film thickness on all substrates follows a similar trend, with some deviation present for larger number of cycles. ....	54
<b>Figure 3.3:</b> TEM images of MWCNTs coated with (a) 25, (b) 40, (c) 50, (d) 80, (e) 100, and (f) 150 cycles of ZnO by atomic layer deposition. Nucleation is occurring after 25 cycles and the film begins to coalesce as the number of ALD cycles increases. The film surface is rough and even with 150 cycles some portions of the nanotubes remained uncoated.....	55
<b>Figure 3.4:</b> The (a) ultimate strain and (b) Young’s Modulus versus cycle number for nylon nanofibers coated with TiCl <sub>4</sub> /H <sub>2</sub> O and TIP/H <sub>2</sub> O ALD at 105°C (solid symbols) and 50°C (open symbols), as well as results from nylon coated with ALD Al <sub>2</sub> O <sub>3</sub> and ZnO at 105°C. As the number of ALD cycles increases, the ultimate strain decreases and Young’s Modulus increases for the aluminum oxide and TiCl <sub>4</sub> /H <sub>2</sub> O coated samples, consistent with increased brittleness. The TIP/H <sub>2</sub> O and zinc oxide samples show trends similar to the uncoated nylon nanofibers.....	56
<b>Figure 3.5:</b> Modulus measured by AFM nanoindentation on (a) nylon 6 nanofibers and (b) silicon substrate. The modulus increases after the deposition of 100 ALD cycles of	

aluminum oxide and titanium dioxide using  $\text{TiCl}_4/\text{H}_2\text{O}$ . The modulus was unchanged after 400 cycles of  $\text{TiCl}_4/\text{H}_2\text{O}$ , as anticipated according to previous results. .... 57

**Figure 3.6:** AM/FM AFM image of the cross-section of a nylon 6 nanofiber mat coated with 100 cycles of  $\text{TiCl}_4/\text{H}_2\text{O}$  ALD. This technique is sensitive to the stiffness of the underlying substrate as indicated by the change in dissipation as the cantilever interacts with the nanofibers compared to the stiffer surrounding epoxy. .... 58

**Figure 3.7:** Cross-sectional TEM images of aluminum oxide coated nylon (a, d, g), polypropylene (b, e, h), and P55D (c, f, i). Samples (a)-(c) were coated at  $50^\circ\text{C}$  with 200 ALD cycles whereas samples (d)-(f) were coated at  $100^\circ\text{C}$ . The ALD-Hold recipe with longer precursor exposures were used for panels (g)-(I) which were coated with 200 ALD-Hold cycles at  $50^\circ\text{C}$ . .... 59

**Figure 4.1:** (a)-(d) Carbon nanotubes contained in fiber bundles. Image (a) shows a cotton ball loaded with CNTs prior to ALD processing. (b) After ALD coating the CNTs were rinsed from the cotton balls using methanol, but large amounts of CNTs remained. (c) Quartz wool fiber bundle after being loaded with CNTs and prior to ALD processing. (d) After coating and rinsing, fewer CNTs remained in the quartz wool compared to cotton. Images (e) and (f) show CNTs contained in cotton and polypropylene fiber baskets, respectively. Panel (g) shows the materials used to create the baskets. .... 81

**Figure 4.2:** TEM Images of MWNTs coated with a) 25 cycles of  $\text{Al}_2\text{O}_3$  ALD and b) 80 cycles  $\text{Al}_2\text{O}_3$  ALD at  $90^\circ\text{C}$  from fiber bundle method. Image a) shows a continuous but not conformal coating with the coating thickness varying from 3.5 to 4.5 nm. Image b) has a continuous and conformal coating with a thickness of only 4.3 nm, similar to the 25 cycle coating. .... 82

**Figure 4.3:** TEM images of MWNTs coated with a) 25; b) 50; c) 100; and d) 200 cycles of  $\text{Al}_2\text{O}_3$  ALD at  $90^\circ\text{C}$  using the polypropylene basket method. The coatings were continuous and conformal and the film thickness increase linearly with the number of ALD cycles. .... 83

**Figure 4.4:** Graph comparing film thickness on different Si controls and MWNTs using the PP fiber mat. Thickness was measured on silicon directly wrapped in cotton (“Si / PP”), in a PP basket (“Si / PP basket”), and for no fiber containment (“Si / open”). The film thickness increases with linearly with cycle number, and the growth rate is nearly the same on all silicon samples and on the CNTs. .... 84

**Figure 4.5:** TEM images of MWNTs coated with a) 25; b) 50; c) 100; and d) 200 cycles  $\text{Al}_2\text{O}_3$  ALD at  $90^\circ\text{C}$  using the cotton wrapped basket method. The coating thickness increased linearly with cycle number. Several uncoated or broken ends were observed as shown in panel (d). In other images (not shown), the number of visible broken ends increases as the coating thickness increases. .... 85

**Figure 4.6:** TEM images of MWNTs coated with a) 10 and b) 15 cycles  $\text{Al}_2\text{O}_3$  ALD at  $90^\circ\text{C}$  using the cotton wrapped basket method. Growth of nuclei had begun by 10 cycles and these nuclei were beginning to grow together at 15 cycles. .... 86

**Figure 4.7:** Graph comparing ALD growth on Si wafers and MWNTs where the substrates (Si and nanotubes) are encased in cotton fiber baskets. The plot also includes thickness measured on silicon when the substrate is directly wrapped in cotton (without the basket) (labeled “Si / cotton”) and when no fiber containment is present (labeled “Si / open”). The growth increases linearly with cycle number at about the same rate observed for fibers encased in polypropylene (Figure 4.4). The film thickness on all substrates follows a similar trend, with some deviation present for larger number of cycles..... 87

**Figure 4.8:** TEM images of MWNTs coated using the basket method with a cotton fiber wrapping. These nanotubes were coated with 50 cycles of Al<sub>2</sub>O<sub>3</sub> ALD at 90°C using a recipe of 1s TMA/30s N<sub>2</sub>/1s H<sub>2</sub>O/30s N<sub>2</sub>. This recipe resulted in nanotubes with a range of film thicknesses from a) no coating to b) coatings up to approximately 4 nm. The variation in film conformality is likely due to inadequate diffusion of precursor gases through the cotton fiber wrap..... 88

**Figure 4.9:** Raman spectra of MWNTs treated with a) 0 cycles b) 25 cycles c) 50 cycles and d) 100 cycles of Al<sub>2</sub>O<sub>3</sub> ALD. The spectra show peak locations typically associated with MWNTs..... 89

**Figure 4.10:** TEM images from MWNTs mounted on grids prior to deposition. (a) After 10 cycles of Al<sub>2</sub>O<sub>3</sub> ALD, nodular nuclei are readily seen. (b) After 15 cycles, the nuclei have grown into a rough but cohesive film coating. (c) After 100 and (d) 200 cycles, a smooth and conformal film coating is achieved. This trend follows closely that shown in Figures 4.3 and 4.5, obtained when the same type of nanotubes are coated using the fiber basket method.... 90

**Figure 4.11:** (a) SWNTs as received; and (b) after coating with 100; and (c) 200 cycles of Al<sub>2</sub>O<sub>3</sub> ALD. Samples were mounted onto a TEM grid prior to deposition. The coating thickness is approximately 8 ± 2 nm after 100 cycles and 20 ± 3 nm after 200 cycles. The rope-like aggregates were coated with a relatively uniform coating, whereas individual single-walled nanotubes demonstrated nodular growth. After 200 cycles, the nodules began to grow together into a cohesive film. .... 91

**Figure 4.12:** TEM images of DWNTs (a) uncoated; (b) and after 100; and (c) 200 cycles of Al<sub>2</sub>O<sub>3</sub> ALD coating. The DWNTs showed nodular growth at 100 cycles. By 200 cycles some of the nodules had grown together to form a more continuous coating, however, many uncoated regions remained. The nodule radius was approximately 10 ± 2 nm for the 100 cycle sample. The film thickness for the 200 cycle sample had increased to approximately 21 ± 3 nm for the coated portions of the 200 cycle sample. This is consistent with nucleation on defects, followed by facile film growth with little additional film nucleation on this particular nanotube type..... 92

**Figure 4.13:** TEM images of (a) uncoated functionalized MWNTs (b) functionalized MWNTs coated with 100 cycles of Al<sub>2</sub>O<sub>3</sub> ALD and (c) functionalized MWNTs coated with 200 Al<sub>2</sub>O<sub>3</sub> ALD. The coating thickness was approximately 11.8 ± 0.6 nm for the 100 cycle sample and 23 ± 2 nm for the 200 cycle sample. The coatings were smooth and conformal for both the 100 and 200 cycle samples..... 93

<b>Figure 5.1:</b> TEM images of MWCNTs coated with (a) 25, (b) 40, (c) 50, (d) 80, (e) 100, and (f) 150 cycles of ZnO by atomic layer deposition. Nucleation is occurring after 25 cycles and the film begins to coalesce as the number of ALD cycles increases. The film surface is rough and even with 150 cycles some portions of the nanotubes remained uncoated.....	106
<b>Figure 5.2:</b> Film thickness varies linearly with the number of ALD cycles with a growth rate of $\sim 2 \text{ \AA/cycle}$ , very similar to growth rates seen on planar samples at $100^\circ\text{C}$ . The silicon sample wrapped in cotton simulated the film (Cotton Si) has film thicknesses very similar to the unwrapped silicon control (Si).....	107
<b>Figure 5.3:</b> TEM images of MWCNTs coated with (a) 25, (b) 50, (c) 100, and (d) 200 cycles of ZnO ALD at $100^\circ\text{C}$ . The nucleation and growth is similar to the basket coated samples with nucleation occurring at 25 cycles, however the growth is slower on the grid loaded samples. ....	108
<b>Figure 5.4:</b> Film thickness by cycle number as determined by TEM for MWCNTs coated using the basket method and coated on the TEM grids. The growth is linear for both methods; however, the growth rate is much higher using the basket method. ....	109
<b>Figure 5.5:</b> Multiwall carbon nanotubes coated with 50 cycles of ZnO using short soak and hold times. Some nanotubes showed films $\sim 11 \text{ nm}$ thick (a) while others only had sparse ZnO nuclei (b).....	110
<b>Figure 5.6:</b> Raman spectra of uncoated MWNTs and MWNTs coated with 50 and 100 cycles of ZnO by ALD. The carbon nanotube structure is unchanged after the ZnO deposition.....	111
<b>Figure 6.1:</b> Example of an uncoated nylon nanofiber sample mounted on a cardstock frame using double sided Kapton tape prior to stress-strain testing. ....	133
<b>Figure 6.2:</b> Schematic of the home built hot-wall viscous flow reactor used to coat the nylon nanofibers.....	134
<b>Figure 6.3:</b> Film thickness vs. ALD cycle number for the silicon wafer monitors coated at a deposition temperature of (a) $105^\circ\text{C}$ and (b) $50^\circ\text{C}$ . The wafers were placed in the reactor while the nanofibers were being coated to monitor film growth. ....	136
<b>Figure 6.4:</b> Representative SEM images showing the morphology of (a) uncoated nylon nanofibers, approximately $200 \text{ nm}$ in diameter with smaller nanofibrils dispersed throughout the mat. The morphology of the nanofibers was not changed after coating with either 100 cycles of (b) $\text{Al}_2\text{O}_3$ , (c) ZnO, (d) $\text{TiO}_2$ using $\text{TiCl}_4/\text{H}_2\text{O}$ or (e) $\text{TiO}_2$ using $\text{TIP}/\text{H}_2\text{O}$ . The nanofibrils are more apparent after $\text{Al}_2\text{O}_3$ and $\text{TiO}_2$ via $\text{TiCl}_4/\text{H}_2\text{O}$ . ....	137
<b>Figure 6.5:</b> Cross-sectional TEM images of nylon nanofibers that were (a-b) uncoated, (c-d) coated using 200 cycles of $\text{TiCl}_4/\text{H}_2\text{O}$ and (e-f) coated using 200 cycles of $\text{TIP}/\text{H}_2\text{O}$ . All coatings were performed at $50^\circ\text{C}$ . The uncoated nanofibers show little TEM contrast relative to the epoxy, whereas there is a clearly defined shell around the titania coated nanofibers. The film is very uniform on the $\text{TiCl}_4/\text{H}_2\text{O}$ coated fibers, but coating is thinner and less well-defined for the $\text{TIP}/\text{H}_2\text{O}$ process. ....	138

**Figure 6.6:** FTIR difference spectra of the titanium dioxide coated nylon nanofibers for coating using (a), (c)  $\text{TiCl}_4/\text{H}_2\text{O}$  and (b), (d)  $\text{TIP}/\text{H}_2\text{O}$ . Spectra in (a) show  $\text{TiO}_2$  modes after ~100  $\text{TiCl}_4/\text{H}_2\text{O}$  cycles, whereas spectra in (b) show minimal  $\text{TiO}_2$  features after 400 cycles of  $\text{TIP}/\text{H}_2\text{O}$ . Under a more magnified absorbance scale in (c) and (d),  $\text{TiO}_2$  features become apparent for  $\text{TIP}/\text{H}_2\text{O}$  samples. .... 139

**Figure 6.7:** (a) The XPS survey scan for uncoated nylon shows oxygen, nitrogen and carbon signals. After 100 cycles of  $\text{TiCl}_4/\text{H}_2\text{O}$ , only trace amount of nitrogen are detected, whereas a nitrogen peak is still visible for the  $\text{TIP}/\text{H}_2\text{O}$  sample. Figures (b) and (c) show the atomic percentages based on film thickness for titanium and oxygen for  $\text{TiCl}_4/\text{H}_2\text{O}$  and  $\text{TIP}/\text{H}_2\text{O}$  samples, respectively. .... 140

**Figure 6.8:** Stress-strain data from one representative nylon nanofiber sample coated with titanium dioxide using (a)  $\text{TiCl}_4/\text{H}_2\text{O}$ , (b)  $\text{TIP}/\text{H}_2\text{O}$ , (c) aluminum oxide, and (d) zinc oxide. The initial slope of the stress-strain curves increase with increasing cycle numbers for the samples coated with either (a)  $\text{TiCl}_4/\text{H}_2\text{O}$  or (c) aluminum oxide, indicating more ceramic behavior. The (b)  $\text{TIP}/\text{H}_2\text{O}$  and (d) zinc oxide coated samples show properties similar to the uncoated nylon nanofibers even at higher cycle number. .... 141

**Figure 6.9:** The (a) ultimate strain and (b) Young's Modulus versus cycle number for nylon nanofibers coated with  $\text{TiCl}_4/\text{H}_2\text{O}$  and  $\text{TIP}/\text{H}_2\text{O}$  ALD at  $105^\circ\text{C}$  (solid symbols) and  $50^\circ\text{C}$  (open symbols), as well as results from nylon coated with ALD  $\text{Al}_2\text{O}_3$  and  $\text{ZnO}$  at  $105^\circ\text{C}$ . As the number of ALD cycles increases, the ultimate strain decreases and Young's Modulus increases for the aluminum oxide and  $\text{TiCl}_4/\text{H}_2\text{O}$  coated samples, consistent with increased brittleness. The  $\text{TIP}/\text{H}_2\text{O}$  and zinc oxide samples show trends similar to the uncoated nylon nanofibers. .... 142

**Figure 7.1:** Force-indentation graph comparing the force curves for a silicon substrate and a nylon 6 nanofiber. The AFM cantilever experiences a greater amount of force for a more shallow indentation depth for the stiffer silicon substrate compared to the more pliant nylon nanofiber. .... 155

**Figure 7.2:** AFM images showing the (a) uncoated nylon 6 nanofibers on a silicon substrate, (b) the nanofibers and Si coated with 100 cycles of  $\text{TiO}_2$  coated using  $\text{TiCl}_4/\text{H}_2\text{O}$ , and (c) the nanofibers coated with 100 cycles of aluminum oxide. The numbers indicate the substrate modulus in GPa as measured by the Igor program. .... 156

**Figure 7.3:** Modulus measured by AFM nanoindentation on (a) nylon 6 nanofibers and (b) silicon substrate. The modulus increases after the deposition of 100 ALD cycles of aluminum oxide and titanium dioxide using  $\text{TiCl}_4/\text{H}_2\text{O}$ . The modulus was unchanged after 400 cycles of  $\text{TIP}/\text{H}_2\text{O}$ , as anticipated according to previous results. .... 157

**Figure 7.4:** A Nylon 6 nanofiber coated with 100 cycles of titanium dioxide via  $\text{TiCl}_4/\text{H}_2\text{O}$  and its corresponding force curve after being depressed with the AFM cantilever. The force of the cantilever broke through the titanium dioxide coating and into the nanofiber, leaving the shape of the cantilever imprinted on the nanofiber. .... 158

**Figure 7.5:** AM-FM AFM image of the cross-section of a nylon 6 nanofiber mat coated with 100 cycles of  $\text{TiCl}_4/\text{H}_2\text{O}$  ALD. This technique is sensitive to the stiffness of the underlying substrate as indicated by the change in dissipation as the cantilever interacts with the nanofibers compared to the stiffer surrounding epoxy. .... 159

**Figure 8.1:** Melt-pressed (a) polypropylene (b) P55D and (c) nylon 6 and the beads used for melt-pressing ..... 182

**Figure 8.2:** Cross-sectional TEM images of aluminum oxide coated nylon (a, d, g), polypropylene (b, e, h), and P55D (c, f, i). Samples (a)-(c) were coated at  $50^\circ\text{C}$  with 200 ALD cycles whereas samples (d)-(f) were coated at  $100^\circ\text{C}$ . Longer precursor exposures were used for panels (g)-(I) which were coated with 200 ALD-hold cycles at  $50^\circ\text{C}$ . .... 183

**Figure 8.3:** FTIR difference spectra of P55D coated with aluminum oxide using ALD at  $50^\circ\text{C}$ . A large change occurs after the first 10 ALD cycles, but the precursors continue to react with the P55D even after 100 cycles. The bare spectrum has been normalized by a factor of 0.1 compared to the coated spectra. .... 185

**Figure 8.4:** Examples of stress-strain curves from uncoated (a) nylon 6, (b) polypropylene and (c) P55D. Several uncoated nylon 6 and polypropylene samples necked during testing as shown in panel (a). .... 187

**Figure 8.5:** Young's modulus for (a) nylon 6, (b) polypropylene and (c) P55d after being treated with either ALD or ALD-holds at  $50^\circ\text{C}$  and  $100^\circ\text{C}$ . The ALD-hold treated samples have a larger increase in modulus compared to the ALD treated samples. The P55D samples have the largest increase with the modulus being more than doubled after 100 ALD-hold cycles at  $50^\circ\text{C}$ . .... 188

**Figure 8.6:** Comparison in Young's Modulus for (a) nylon 6 and (b) polypropylene treated using a microdose (MD) method versus ALD-holds and heat treated (HT) samples. The microdose method is as effective at the hold method with nearly equivalent increases in modulus with less processing time. While the heat treatment had little effect on the nylon 6, the modulus of polypropylene was largely increased. .... 189

**Figure 8.7:** Strain at break for (a) nylon 6, (b) polypropylene, and (c) P55D for all treatments. The strain at break for nylon 6 and polypropylene has large error bars for the uncoated sample due to necking during testing. As the number film thickness as measured on silicon increased, the occurrence of necking decreased leading to smaller error bars. The aluminum oxide coatings have little effect on the strain at break for the P55D samples indicating that they retain their flexibility. .... 190

**Figure 8.8:** Percent change in (a) elastic modulus and (b) strain at break for low and high molecular weight PEO. The aluminum oxide increases the modulus and decreases the strain at break for the low molecular weight PEO, but has little effect on the high molecular weight PEO. .... 191

**Figure 8.9:** Percent change in (a) elastic modulus and (b) strain at break for low and high molecular weight PP. Little change in modulus and strain at break is observed for both samples..... 192

**Figure 8.10:** The uncoated high molecular weight sample for water resistance testing is much lighter than the sample coated with 200 cycles of an aluminum oxide seed layer followed by 600 cycles of titanium dioxide. After water testing the samples swelled..... 194

## CHAPTER 1. Introduction

Polymers have been widely researched for their unique physical and chemical properties and are found in many different areas of research and industry. For example, specially designed polymers are used in aircraft and aerospace design, for energy devices, as well as in vehicles as components of bumpers, doors and hoods. Polymers may be processed to form films, tubing, molds, and fibers. One particularly interesting form of polymer processing is the emergence of electrospinning, which has allowed for the creation of polymer fibers with diameters on the nanoscale. Due to small fiber diameters, electrospun polymer mats have been used in filtration,<sup>1</sup> tissue scaffolding,<sup>2</sup> protein delivery,<sup>3</sup> sensing applications,<sup>4</sup> and for functional textiles.<sup>5,6</sup> In addition to polymer nanofibers, there are a wide variety of other nanomaterials such as carbon nanotubes (CNTs) that are also of interest. Similar to polymers, carbonaceous nanomaterials may possess nanoscale dimensions and have unique mechanical, thermal and electrical properties which allow them to be used for applications such as electrochemical devices,<sup>7,8</sup> reinforcements for composite materials,<sup>9</sup> sensors,<sup>10</sup> and field emission devices.<sup>11</sup> The addition of carbon nanomaterials, such as CNTs, to polymers for reinforcement is widely studied.<sup>12</sup> For example, polymer-CNT composite materials are used for transparent conductive coatings and have greater flammability resistance.<sup>13</sup> However, in spite of the individually unique properties that polymers and carbon nanotubes have, surface modification by the addition of metals, metal-oxides, etc. is desired to further enhance the functionality of these materials and more finely-tune the performance.

A variety of methods have been employed to functionalize carbonaceous and non-carbon nanomaterials, such as polymers by the deposition of thin films. Here-in, two broad

categories are discussed; wet chemical methods and vapor deposition methods. For the first category, the wet chemical methods discussed include sol-gel, layer-by-layer, electroless plating, dip coating, and spraying. For the second category, the vapor treatments discussed include physical vapor deposition (PVD), chemical vapor deposition (CVD), and a more specific type of CVD, atomic layer deposition (ALD). These two broad categories contain thin film deposition methods that have their own advantages and disadvantages. Often times, coating thermally sensitive materials and complex 3D structures proves to be difficult. Atomic layer deposition is considered to be a facile method for circumventing temperature and surface area coating challenges, while simultaneously achieving high control over film thickness and morphology.

## **1.1 Sol-Gel**

The sol-gel process gets its name from combining “sols” or dispersions of colloidal particles and “gels” which are interconnected, porous, rigid networks.<sup>14</sup> Sol-gels are made using a solution of dispersed colloidal particles or by using alkoxide precursors that undergo hydrolysis and polycondensation. There are several steps in the production of sol-gels. First the sol is created by mixing colloidal particles or alkoxide particles and a hydrolyzing agent, usually water. The hydrolysis and polycondensation reaction between the alkoxide precursor and hydrolyzing agent forms polymer chains that act as colloidal particles. The size of the colloidal particles and the degree of cross-linking between them will depend on the pH of the solution and the ratio of hydrolyzing agent to precursor. The sol can then be cast into a mold where after time gelation will occur. Gelation is marked by a significant increase in

viscosity. Next the gel is aged to increase the strength of the material and dried to remove any liquid in the pores. The drying process is very important in determining the pore size and degree of porosity in the final gel. It is also very important to control porosity to prevent cracking in the resulting material. The material can then be chemically stabilized by further dehydration to remove any chemisorbed hydroxyl groups in the pores. Finally the material can be heat-treated to remove pores in a process called densification.<sup>14,15</sup> A number of unique materials have been derived using the sol-gel process including a variety of metal oxides,<sup>15</sup> silica monoliths,<sup>14</sup> as well as coatings containing biomolecules.<sup>8,16</sup>

One particularly interesting application of the sol-gel method is utilizing polymer fibers and textiles,<sup>17</sup> membranes,<sup>18</sup> and carbon nanotubes<sup>19</sup> as sacrificial templates. For example, the sol-gel process has been used to coat electrospun poly(L-lactide) fibers with titanium dioxide. In this study, the coated fibers were calcined to remove the poly(L-lactide) fibers leaving behind titanium dioxide microtubes.<sup>20</sup> However, it is difficult to fully coat the complex polymer network in fibers and while some control over thickness is possible, careful control of processing parameters is required and most-often time-consuming.<sup>21</sup> Furthermore, the temperature sensitivity of various polymers limits the drying processes if the polymeric material is to be retained.

## **1.2 Layer by Layer Growth**

Layer-by-layer growth is a thin film growth method that utilizes oppositely charged polyelectrolytes. A substrate with a charged surface is first exposed to an oppositely charged polyelectrolyte, either a polyanion or polycation. The polyelectrolyte ionically bonds to

cover the surface, and the remaining polyelectrolyte is rinsed away to control film thickness. Next, the substrate is exposed to the oppositely charge polyelectrolyte and then the excess is again rinsed away and the process is repeated to grow the thin film. The layer-by-layer method has been used to successful coat many different substrates. For example, polymer nanoparticles<sup>22,23</sup>, acid functionalized carbon nanotubes,<sup>24</sup> and nanorods.<sup>25</sup> In addition, it is also possible to incorporate different materials such as metal oxides,<sup>22</sup> clays,<sup>26</sup> and proteins<sup>27</sup> in to the polyelectrolyte thin film. One advantage of the layer-by-layer growth method is a slight control over film thickness. By carefully rinsing between steps it is possible to obtain linear growth by varying the cycle number. Moreover, the layer-by-layer method has been shown to be successful even with only a weakly charged surface.<sup>28</sup> Additionally, the thickness is similar with different substrates, indicating the growth is dependent on the polyanion/polycation chosen.<sup>28</sup> The major disadvantages of the layer-by-layer growth technique are the time-consuming adsorption and rinsing steps, as well as the coating materials being limited to polyelectrolytes.<sup>29</sup> Additionally and as previously mentioned, the large polymer chains in the polyelectrolyte make it difficult to fully coat complicated 3D networks such as electrospun nanofiber mats.

### **1.3 Electroless Plating**

Electroless plating is a wet chemical method in which metal salts are reduced in solution to form a thin film on a substrate of interest. For example, electroless plating may be used to deposit metallic films on nonconductive substrates. In particular, the substrate of choice is placed in a temperature controlled bath containing the reducing agent, metal ion

component, along with several other additives.<sup>30</sup> The additives promote film growth and stabilize the electroless plating solution. A variety of coatings may be deposited and include copper, nickel, silver, and various other alloys.<sup>30,31</sup> Electroless plating is a proven method for depositing thin films on polymer materials and nanotubes. For example, Adachi et al. deposited a thin film of a nickel-phosphorous alloy on polyamide 6 disks after impregnating the polymer with palladium catalyst particles using super critical carbon dioxide as a plasticizer.<sup>32</sup> In a different study, special surface preparation was also needed to create reactive centers on carbon nanotubes for the deposition of thin films by electroless plating. Kong et al. sensitized and activated the surface of MWNTs by treatment with  $\text{SnCl}_2$  followed by treatment with  $\text{PdCl}_2$  to create Pd reactive sites for the electroless deposition of nickel films.<sup>33</sup> Other methods of preparing the substrate surface include etching and plasma pretreatment.<sup>30,34</sup> However, it is worth mentioning that the addition of pre-processing steps may alter the uniquely desirable properties of the various polymers and/or nanotubes.

#### **1.4 Liquid Phase Deposition**

Example liquid phase deposition methods include spraying and dip coating. Spraying allows one to deposit a liquid material onto the substrate followed by evaporation at room temperature or in a heated inert atmosphere. Foitzik et al. compared several methods of depositing polypyrrole onto wool substrates in an effort to increase the electronic conductivity, which included solution and vapor chemical polymerization, as well as spray coating.<sup>35</sup> The solution polymerized sample had the highest initial conductivity, whereas the spray coated sample showed similar conductivity, as well as good abrasion resistance.<sup>35</sup> Dip

coating is a different liquid phase deposition method. Dip coating is more simple than spraying and works by dipping a substrate into a liquid solution followed by careful removal. The removal speed of the sample/substrate will affect the uniformity of the film. After removal the solution can then be evaporated or heated to control the subsequent film thickness. Sojka-Ledakowicz et al. utilized a dip-coating method to deposit nanostructural titanium dioxide on a polyester nonwoven fabric.<sup>36</sup> Titanium dioxide and aminosilane-grated titanium dioxide was dispersed in aqueous solutions containing PEG and HEC. The polyester samples were dipped into the solution and then squeezed at a nip pressure of 30 kG/cm<sup>2</sup> followed by drying at 100°C. The titanium coated samples showed increased UV resistance compared to the unmodified material.<sup>36</sup> While both spraying and dip-coating methods can be used for polymers and carbon nanotubes, it is difficult to control film thickness and uniformity.

There are also a wide variety of other liquid-based deposition methods, including hydrothermal synthesis, chemical bath deposition, electroplating, and several others. Metal oxide nanostructures are grown using hydrothermal synthesis by mixing metal oxide precursors such as metal salts or alkoxides and water in a pressurized vessel at elevated temperatures.<sup>37</sup> Hydrothermal synthesis can deposit a variety of materials including vanadium oxide,<sup>38</sup> zinc oxide,<sup>39</sup> iron oxide and nickel oxide<sup>40</sup> among others. Chemical bath deposition is an inexpensive process where substrates are immersed in a solution containing the chemical precursors needed to precipitate and form the film.<sup>41</sup> The chemical precursors used, the composition of the solution, solution temperature, and pH all affect the deposited film.<sup>41,42</sup> Electrodeposition is capable of depositing metals and metal oxides on conductive

substrates. The electroplating set-up uses a cathode (the substrate to be deposited on) and an anode placed in solution of metal salts. A current is passed through the system and the metal salts will reduce and deposit on the substrate.<sup>43</sup>

## 1.5 Physical Vapor Deposition

Physical vapor deposition methods include sputtering and evaporation techniques. Physical vapor deposition is a physical process that delivers atoms or atom clusters to a surface to form a thin film. The general process involves particles entering the gas phase by bombardment, in the form of the sputtering process, or by heat in the form of the evaporation method. As a result, the gas phase particles become physisorbed to the substrate surface.<sup>44</sup> Specifically and for the sputtering process, inert atoms such as argon are ionized and accelerated towards a target material. The target atoms are vaporized and deposit on the substrate.<sup>45</sup> The target material can be a metal such as gold or a metal oxide.<sup>46</sup> Sputtering is a common method for coating polymer films and fibers with a conductive layer of particles (e.g. Au or Pd) to prevent charging during imaging by scanning electron microscopy. In some cases, reactive gases can be added to the growth zone to promote desired reactions. For example oxygen can be added during sputter deposition of silicon to produce SiO<sub>2</sub>.<sup>47</sup>

Different from sputtering, evaporation works by heating or applying other forms of energy (e.g. an electron beam) to a target material to the point where atoms evaporate from the surface. The evaporated atoms then recondense on the substrate of interest. Deng et al. used the evaporation process to deposit gas diffusion barriers on polymers.<sup>48</sup> However, sputtering and evaporation deposition methods are only capable of functionalizing the

surface of the substrate within line-of-sight and therefore cannot penetrate fibrous or complex 3D substrates. Therefore, the non-uniform coating created by physical vapor deposition may not provide reproducible and repeatable thin films on polymer fibers or carbon nanotube powders. Evaporation can also damage the surface of the substrate through etching.<sup>49</sup>

## **1.6 Chemical Vapor Deposition**

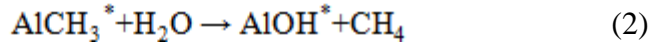
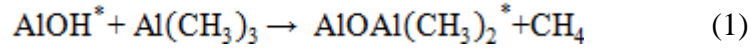
Chemical vapor deposition (CVD) delivers chemical species (such as metal-organic precursors, oxygen molecules, etc.) in the gas phase to promote surface reactions that form thin films. The chemical reaction processes, in part, distinguish it from physical vapor deposition methods. Typically, the surface is heated during CVD to initiate chemical dissociation of the precursors in the vapor zone adjacent to the growth surface. For many systems, low substrate temperatures are desired, and plasma excitation or incident radiation are used in place of thermal energy to promote the chemical vapor deposition reactions.<sup>50</sup> Homogeneous reactions or reactions occurring between the gaseous precursors form a powder product that may potentially deposit on the substrate. Heterogeneous reactions occur between the gaseous precursors and the substrate to form a film. The promotion of heterogeneous or homogeneous reactions can be affected by controlling the process pressure, temperature and vapor transport conditions (e.g. molecular, laminar or turbulent). When homogeneous reactions are minimized, surface reactions promote dense films with well controlled growth rates, whereas a mixture of heterogeneous and homogeneous reactions leads to lower density, porous films<sup>51</sup> that often have undesirable electronic or physical properties. A significant benefit to CVD, in contrast to physical vapor deposition, is that the

surface chemical interactions can allow for conformal and uniform coatings over complex 3D structures. This is particularly important for electronic device manufacturing, where coatings often have to be maintained uniform over highly irregular surface contours.<sup>52</sup> The thickness of the film may also be controlled by tuning the CVD parameters including substrate temperature, operating pressure, and the chemistry and composition of the precursors.<sup>50</sup> A variety of materials can be deposited by CVD including metals, metal oxides, carbides, nitrides, III-V, and II-VI materials.<sup>51,53</sup> While CVD is usually done at elevated temperatures, using plasma enhanced CVD allows film deposition at temperatures adequate for thermally sensitive polymers. However, plasma bombardment can also damage the substrate surface and the deposited film.<sup>50</sup>

### **1.7 Atomic Layer Deposition**

Atomic layer deposition (ALD) is a form of chemical vapor deposition that uses sequential, self-limiting reactions to deposit inorganic films with near monolayer control over thickness.<sup>54</sup> The self-limiting reactions often proceed through a two-step binary cycle of “half-reactions”. The cyclic reaction produces a partial monolayer of deposited film, so that controlling the number of cycles allows the resulting film thickness can be carefully tuned. Furthermore, ALD provides a technique capable of producing conformal and uniform films on a variety of substrates. Atomic layer deposition has been widely used in the semiconductor industry to apply thin films; however, the applications are expanding to gas diffusion barriers, conductive coatings, and for use in electrochemical systems.

The most widely studied ALD reaction system is the trimethyl aluminum (TMA)/water reaction pair. The sequential reactions between TMA and water form an aluminum oxide coating. The two half reactions are as follows:



where the asterisks indicate the respective species adsorbed to the surface.<sup>54</sup> Film growth begins when the substrate is exposed to the first precursor gas, in this case TMA as shown in Figure 1.1. During the first half-reaction, the TMA reacts with –OH species on the substrate surface to produce surface-bound O-Al-CH<sub>3</sub> groups and methane vapor as a byproduct. After the precursor dose, the methane and any unreacted precursor gas are purged out of the reactor by an inert gas. After purging, water vapor is dosed into the reactor for the second half-reaction, where it reacts with surface O-Al-CH<sub>3</sub> to produce O-Al-OH surface termination (along with methane vapor). This termination allows the first half-reaction to be repeated to start the next ALD cycle. The TMA and water exposure sequence defines one ALD cycle, with the reactive surface species being regenerated after each half cycle.

The ALD reaction between TMA and water on a substrate surface is self-limiting in that increasing the exposure time beyond the saturation point does not produce any additional film growth. To achieve this, the surface temperature must be controlled at a point where the thermal energy is sufficient to avoid condensation and promote reaction, but not sufficient to allow precursor decomposition or direct desorption. This leads to the concept of the “ALD

temperature window”, which depends on the precursor, reactant, and in some cases, the substrate surface. Additionally, for ALD to be successfully applied, the byproduct of the reaction must be a gaseous product so that it may be purged from the reactor chamber and not affect the growing film. Ideally, during each ALD cycle one partial monolayer of material is deposited, however, that may change depending on the substrate and also on the reaction conditions. When using ALD to coat materials such as polymers and carbon nanotubes, it is important to understand how the substrate surface affects deposition. Specifically, Figure 1.2 shows how the growth per cycle is affected by the substrate. Linear growth occurs when the substrate has the same number of reactive sites as the growing film so the growth remains constant throughout the process. Substrate-enhanced growth occurs when the initial substrate has more reactive sites than the deposited film so the growth will appear to be greater in the beginning of the reaction. In substrate-inhibited growth the growing film has more reactive sites than the initial substrate so the growth per cycle will increase as the reaction continues. For substrate-inhibited growth, type 2 film thickness goes through a maximum before decreasing and reaching a steady state.<sup>55</sup> Other factors affecting ALD growth include the dosing, purging times and the reactor temperature. A requirement for the dosing time is to ensure that the precursor gases do not get depleted during the dose. If the precursor gases are not provided in a sufficient quantity, the half-reaction would not reach completion and the substrate would not be uniformly coated. Additionally if the purge time is too short excess precursor gas molecules may still remain in the reaction chamber leading to reactant mixing and CVD growth as described in Section 1.6. The ALD temperature range of interest usually occurs at elevated temperatures; however, there has

been a trend towards low temperature ALD for thermally sensitive substrates such as polymers and biomaterials.<sup>54-56</sup>

There are three main growth models used to describe ALD deposition: Weber-Volmer, Frank-Van der Merwe, and Stranski-Krastanov. The Frank-Van der Merwe model describes ideal layer-by-layer growth in which one monolayer of material is deposited at a time. In the Weber-Volmer model, island growth occurs with the material preferentially depositing on the growing film as opposed to the substrate. For the Stranski-Krastanov model, the growth changes during deposition, i.e. the growth may begin according to the layer-by-layer method up to a certain thickness and then change to island growth or in any combined fashion. In another model, random growth may occur in which each site on the substrate and growing coating has an equal probability of reacting.<sup>55</sup> Ultimately, the method of growth will vary depending on the substrate and the substrate's chemistry, as well as the deposited and growing film. Moreover, ALD growth on polymers and carbon nanotubes is complicated by the non-uniformity of bulk polymer composites and/or carbon nanotubes. The growth models and mechanisms using various polymeric substrates and carbon nanotubes are discussed in the subsequent section.

## **1.8 Atomic Layer Deposition on Polymers**

Atomic layer deposition is an excellent technique for coating polymer fiber mats, thereby potentially modifying the mechanical and electrical properties. Atomic layer deposition is capable of coating each polymer fiber with uniform and highly conformal nanoscale inorganic or organic-inorganic thin films.<sup>57-61</sup> Atomic layer deposition is widely used in the

semiconductor industry and has also been applied to polymer substrates to create diffusion barriers,<sup>62</sup> alter wettability,<sup>63</sup> and increase conductivity.<sup>64</sup> One benefit of ALD on fibrous substrates is that the precursors can diffuse throughout the fiber mat, thereby depositing a uniform film on each fiber.<sup>57-59,61</sup> Moreover, ALD has been used with polymers for extra added functionality. For example, Sweet et al. increased the effective conductivity of nonwoven polypropylene fiber mats up to 63 S/cm by depositing a bi-layer of aluminum oxide and zinc oxide.<sup>64</sup> An all fiber capacitor was made by Jur et al. using polypropylene nonwoven fibers and tungsten ALD coated quartz fibers.<sup>6</sup> Moreover, metal or metal oxide nanoparticles, nanotubes, and microtubes can be formed by coating polymers as sacrificial templates.<sup>57,59,65</sup>

Uniform growth and smooth films have been deposited on polymers such as nylon<sup>61</sup> and PVA.<sup>57</sup> The film growth has been shown to be highly dependent on temperature and precursor choice. Spagnola et al. used a quartz crystal microbalance (QCM) to more closely study atomic layer deposition on different polymers. The authors report a large initial mass uptake for polymers with reactive species such as nylon and PVA with a relatively smaller uptake for inert polypropylene.<sup>61</sup> This increased mass uptake was ascribed to precursor diffusion into the subsurface region of the polymers. The relative increase in mass uptake is also likely due to the reactivity of the polymer toward the ALD precursor being used for the desired coating. Using quantitative FTIR analysis, Gong et al.<sup>66</sup> measured the relative reaction between various polymers and TMA. Gong et al. observed that the polyvinyl alcohol (PVA) fibers were more reactive than polypropylene (PP) fibers,<sup>66</sup> and the degree of reactivity is believed to be linked to the QCM mass uptake. Moreover, the degree of

subsurface diffusion is sensitive to the deposition temperature. For example, less subsurface film growth has been observed at lower temperatures for both PP<sup>61,67</sup> and nylon 6.<sup>61,68</sup> In addition to deposition temperature, Spagnola et al. showed that altering dosing conditions promotes diffusion of the ALD precursor into polymer of interest, as well as increase the amount of inorganic within the polymer network.<sup>61,67</sup> Gong et al.<sup>65</sup> created a metal oxide monolith by exposing fibers to a longer TMA dosing time, which allowed the precursor to diffuse throughout the fiber. Therefore, the dosing time plays an important role in diffusion throughout fiber and polymer substrates. In addition, it is important to understand how the various growth modes on polymers will affect their bulk mechanical performance. For example, the exposure time between the substrate and the ALD precursors affects the degree to which mechanical properties such as Young's modulus are altered. While Lee et al. found enhanced mechanical properties for spider silk,<sup>69</sup> we have found that treating electrospun nylon nanofibers with ALD precursors such as trimethyl aluminum (TMA) or titanium tetrachloride (TiCl<sub>4</sub>) can make the mats more brittle while also increasing the elastic modulus. As a result of the aforementioned study, it was found that the chemistry between the substrate and precursor produces profound effects on the mechanical properties. By coating nylon nanofibers using titanium isopropoxide (TIP) in place of TiCl<sub>4</sub> for a titanium dioxide thin film, the elastic modulus and strain at break for the coated mats were unchanged even after 400 ALD cycles. In addition, the increased modulus of fiber mats is further supported for studies on single fibers via AFM nanoindentation experimentation. By understanding the interactions between various polymer substrates and by controlling the

precursor, exposure timing and dosing order it may be possible to tune the mechanical properties of polymers.

## **1.9 Carbon Nanotubes**

Carbon nanotubes (CNTs) are graphene sheets rolled into cylinders. Graphene is a 2-dimensional (2D) allotrope of carbon arranged in a honeycomb structure of hexagons with a characteristic hexagonal lattice and  $sp^2$  hybridized bonds. Different types of carbon structures are made from graphene including fullerene  $C_{60}$ , carbon nanotubes (1D) and graphite (3D). Figure 1.3 shows various allotropes of carbon derived from graphene.<sup>70</sup> Due to the unique mechanical and electrical properties of CNTs, a wide array of applications may potentially utilize CNTs. One application for carbon nanotubes is for use as part of various composite materials for the aircraft and sporting goods industries.<sup>71</sup> Inorganic-nanotube hybrids have also been investigated for new applications such as electrochemical sensors, catalyst supports, field emission devices, as well as for photochemical applications.<sup>72</sup> While the thin film deposition methods described above have been used to coat carbon nanotubes, ALD allows for better control over film thickness for ultra thin films.

## **1.10 ALD on Carbon Nanotubes**

Carbon nanotubes are manufactured in a variety of ways with the most popular being arc-discharge, laser ablation, and chemical vapor deposition.<sup>73</sup> Many of these manufacturing methods use metal catalyst particles such as cobalt, iron, and nickel. However, the use of metallic catalyst particles requires post-processing and purification steps in order to remove the metallic catalyst particles. One method of purification is to chemically treat the

nanotubes using and acid bath. Most often, the purification process creates more defective carbon nanotubes compared to the carbon nanotubes before purification.<sup>74</sup> As a result, the defective sites act as reactive centers on an otherwise unreactive surface. In addition to creating defective sites, a curved CNT surface experiences greater strain resulting in a more reactive surface.<sup>73</sup> Regardless of the method of defect creation, the defect sites themselves act as reactive surface sites for the nucleation and growth of various ALD deposited thin films.

Cavanagh et al. showed atomic layer deposition on carbon nanotubes can result in non-uniform growth due to the relatively inert nanotubes surface.<sup>75</sup> Liyanage et al. coated single walled nanotubes with hafnium oxide and observed island nucleation at the defect sites which began to coalesce as the number of cycles increased.<sup>76</sup> Therefore, a variety of functionalization methods have been used to increase the number of reactive surface species on carbon nanotubes, thereby providing a more reactive surface for uniform growth. For example, typical methods include acidic or basic treatments to create hydroxyl and carboxylic acid terminated reactive sites.<sup>77</sup> A different approach includes using gas phase functionalization. Farmer et al. used gas phase functionalization in which  $\text{NO}_2$  physisorbs to the surface of the nanotubes and dose TMA molecules are attracted to the oxygen groups and physisorb to form a  $\text{NO}_2$ -TMA complex. The  $\text{NO}_2$ -TMA complexes can then react with incoming water. The use of gas-phase functionalization has also been shown to be successful in creating uniform ALD films.<sup>75,78</sup> However, the degree of functionalization required depends on the defect density of the nanotubes. That is, single and double-walled nanotubes

tend to have fewer defects than multi-walled carbon nanotubes (MWCNTs) so they require more functionalization for uniform ALD coatings.

Uniform and conformal growth on pristine carbon nanotubes is difficult due to the surface chemistry. Also, agglomeration of CNTs into bundles creates an additional complexity for coating. That is, carbon nanotubes tend to agglomerate due to strong van der Waals forces. To overcome agglomeration, several different reactor designs have been used to agitate or fluidize the powders. Cavanagh et al. and McCormick et al. built a rotary reactor to coat nanoparticles and nanotubes.<sup>75,79</sup> The rotary reactor design has a porous cylindrical reaction chamber, which is loaded with nanomaterials such as carbon nanotubes<sup>75</sup> or zirconium oxide nanoparticles.<sup>79</sup> The reactor is rotated during coating to fluidize the particles and prevent coalescence. Another type of reactor that mitigates CNT agglomeration is the fluidized bed reactor. Figure 1.4 illustrates a particular fluidized bed reactor that is designed to coat nanopowders. In this fluidized bed reactor design, carrier and precursor gases are dosed into the bottom of a vertical reactor to fluidize the particles. A mechanical agitator in the reactor chamber is used to enhance fluidization and prevent particle coalescence.<sup>80</sup> There are a variety of reactor designs and methods available for uniformly coating nanomaterials and powders, however many of these designs are considered expensive and difficult to design. As an alternative, we established a new method of coating carbon nanotubes in a viscous flow reactor using polymer fiber mats as containment.

### **1.11 Brief Overview of Work**

The objective of this work is to create a process for uniformly coating polymers (i.e. nanofibers and bulk films) and carbon nanotubes. A viscous-flow reactor was used to deposit metal oxide thin films on polymer and carbon nanotube substrates. In what follows, we describe a new method for coating powders and carbon nanotubes using fibrous containment. We also investigate the resulting mechanical properties of polymer substrates after coating with thin metal oxide films.

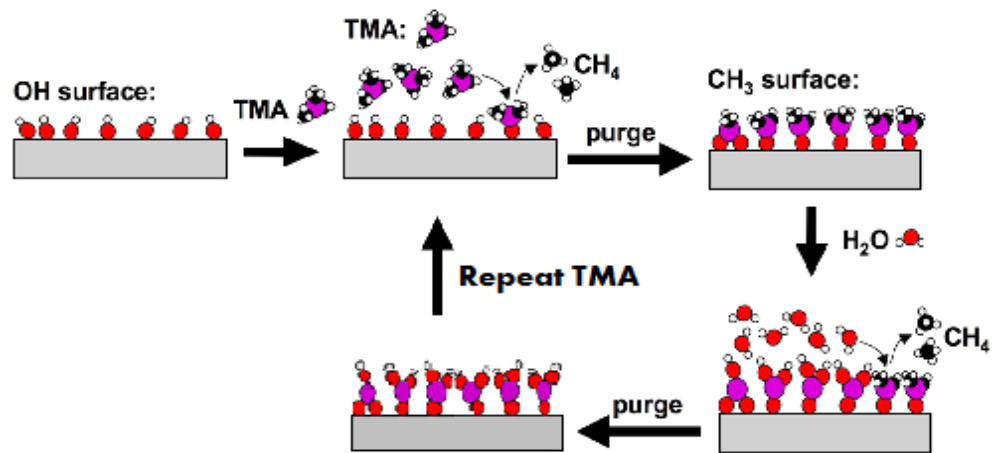


**Figure 1.1:** Reaction sequence for one ALD cycle of TMA/H<sub>2</sub>O for the deposition of aluminum oxide.

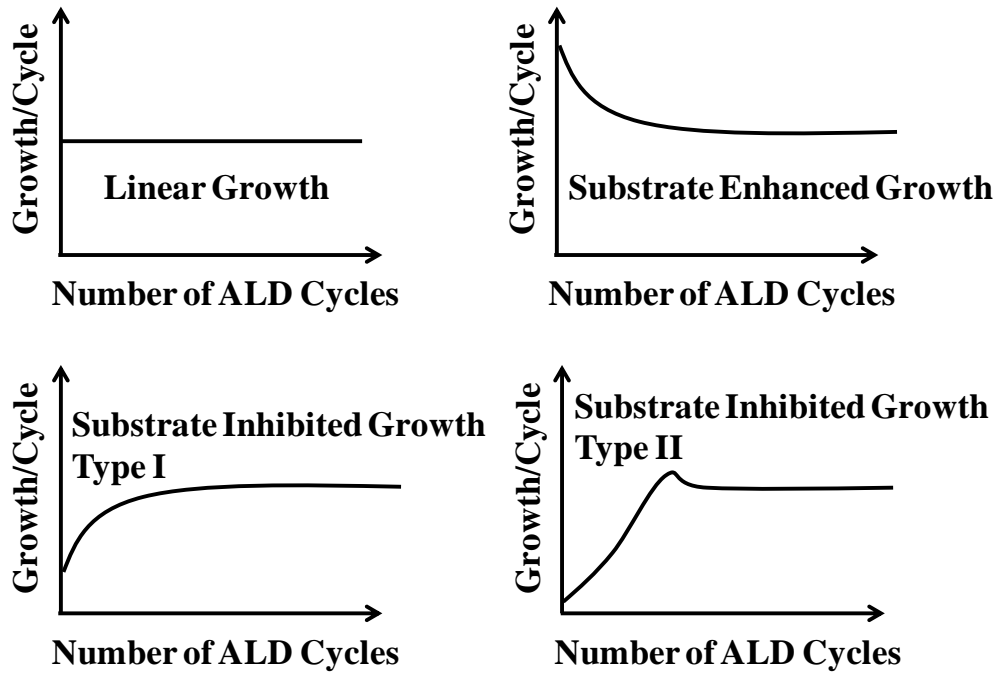


**Figure 1.2:** Different types of substrate dependent ALD growth models.

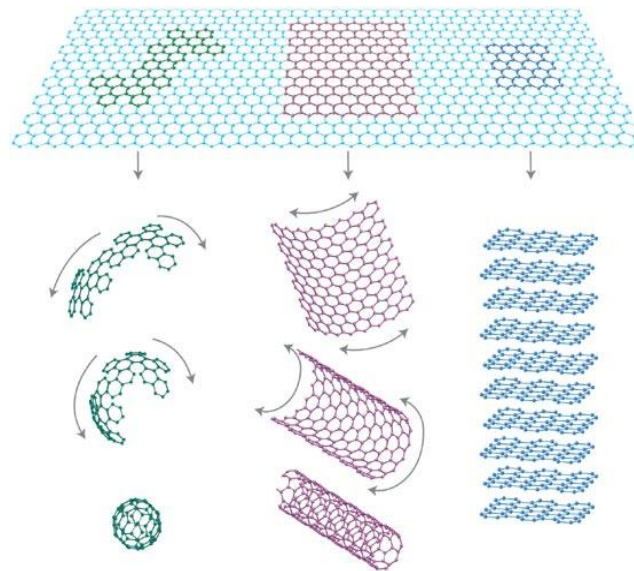


**Figure 1.3:** Diagram of the various graphene derivatives, C<sub>60</sub>, carbon nanotubes and graphite<sup>70</sup>.

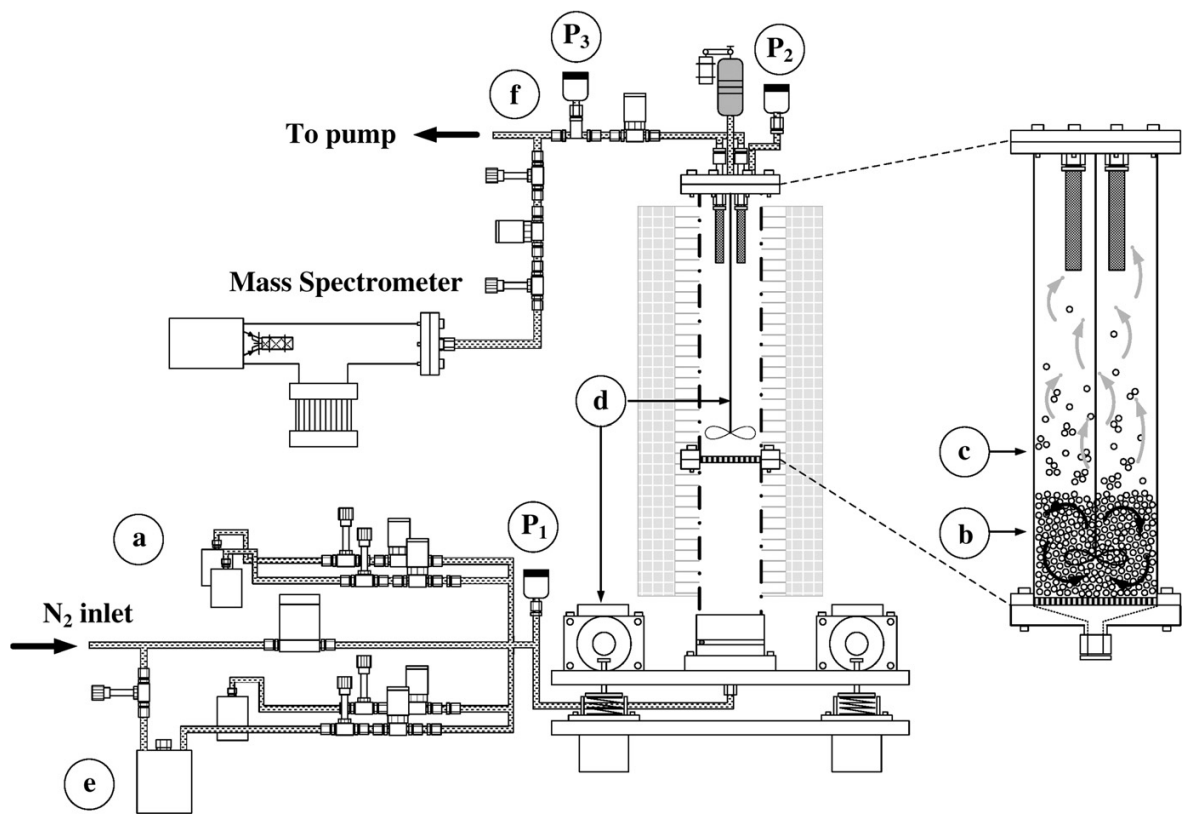


**Figure 1.4:** Schematic of a fluidized bed reactor used to coat nanopowders<sup>80</sup>.

## References

- 1 R. Gopal, S. Kaur, Z. W. Ma, C. Chan, S. Ramakrishna, and T. Matsuura, "Electrospun nanofibrous filtration membrane," *J. Membr. Sci.* **281** (1-2), 581-586 (2006); P. Gibson, H. Schreuder-Gibson, and D. Rivin, "Transport properties of porous membranes based on electrospun nanofibers," *Colloid Surf. A-Physicochem. Eng. Asp.* **187**, 469-481 (2001).
- 2 F. Chen, C. N. Lee, and S. H. Teoh, "Nanofibrous modification on ultra-thin poly(epsilon-caprolactone) membrane via electrospinning," *Mater. Sci. Eng. C-Biomimetic Supramol. Syst.* **27** (2), 325-332 (2007); H. S. Yoo, T. G. Kim, and T. G. Park, "Surface-functionalized electrospun nanofibers for tissue engineering and drug delivery," *Adv. Drug Deliv. Rev.* **61** (12), 1033-1042 (2009).
- 3 J. Zeng, A. Aigner, F. Czubayko, T. Kissel, J. H. Wendorff, and A. Greiner, "Poly(vinyl alcohol) nanofibers by electrospinning as a protein delivery system and the retardation of enzyme release by additional polymer coatings," *Biomacromolecules* **6** (3), 1484-1488 (2005).
- 4 D. Bhattacharyya, K. Senecal, P. Marek, A. Senecal, and K. K. Gleason, "High Surface Area Flexible Chemiresistive Biosensor by Oxidative Chemical Vapor Deposition," *Adv. Funct. Mater.* **21** (22), 4328-4337 (2011); S. Z. Ji, Y. Li, and M. J. Yang, "Gas sensing properties of a composite composed of electrospun poly(methyl methacrylate) nanofibers and in situ polymerized polyaniline," *Sens. Actuator B-Chem.* **133** (2), 644-649 (2008).

- 5 J. S. Jeong, S. Y. Jeon, T. Y. Lee, J. H. Park, J. H. Shin, P. S. Alegaonkar, A. S. Berdinsky, and J. B. Yoo, "Fabrication of MWNTs/nylon conductive composite nanofibers by electrospinning," *Diam. Relat. Mat.* **15** (11-12), 1839-1843 (2006); Z. M. Huang, Y. Z. Zhang, M. Kotaki, and S. Ramakrishna, "A review on polymer nanofibers by electrospinning and their applications in nanocomposites," *Compos. Sci. Technol.* **63** (15), 2223-2253 (2003).
- 6 J. S. Jur, W. J. Sweet, C. J. Oldham, and G. N. Parsons, "Atomic Layer Deposition of Conductive Coatings on Cotton, Paper, and Synthetic Fibers: Conductivity Analysis and Functional Chemical Sensing Using "All-Fiber" Capacitors," *Adv. Funct. Mater.* **21** (11), 1993-2002 (2011).
- 7 Shaojun Guo, Jing Li, Wen Ren, Dan Wen, Shaojun Dong, and Erkang Wang, "Carbon Nanotube/Silica Coaxial Nanocable as a Three-Dimensional Support for Loading Diverse Ultra-High-Density Metal Nanostructures: Facile Preparation and Use as Enhanced Materials for Electrochemical Devices and SERS," *Chemistry of Materials* **21** (11), 2247-2257 (2009).
- 8 Veronika Urbanova, Mathieu Etienne, and Alain Walcarius, "One Step Deposition of Sol-Gel Carbon Nanotubes Biocomposite for Reagentless Electrochemical Devices," *Electroanalysis* **25** (1), 85-93 (2013).
- 9 M. Cadek, J. N. Coleman, V. Barron, K. Hedicke, and W. J. Blau, "Morphological and mechanical properties of carbon-nanotube-reinforced semicrystalline and amorphous polymer composites," *Appl. Phys. Lett.* **81** (27), 5123-5125 (2002); C.

- Y. Wei, "Adhesion and reinforcement in carbon nanotube polymer composite," *Appl. Phys. Lett.* **88** (9) (2006).
- 10 Qing Cao and John A. Rogers, "Ultrathin Films of Single-Walled Carbon Nanotubes for Electronics and Sensors: A Review of Fundamental and Applied Aspects," *Adv. Mater.* **21** (1), 29-53 (2009); J. Kong, M. G. Chapline, and H. J. Dai, "Functionalized carbon nanotubes for molecular hydrogen sensors," *Adv. Mater.* **13** (18), 1384-1386 (2001).
- 11 T. Y. Tsai, C. Y. Lee, N. H. Tai, and W. H. Tuan, "Transfer of patterned vertically aligned carbon nanotubes onto plastic substrates for flexible electronics and field emission devices," *Appl. Phys. Lett.* **95** (1) (2009); Jeong Hoon Byeon and Jang-Woo Kim, "Aerosol assisted fabrication of carbon nanotube/zinc oxide arrays for a field emission device," *Journal of Colloid and Interface Science* **393**, 397-401 (2013).
- 12 Mohammad Moniruzzaman and Karen I. Winey, "Polymer nanocomposites containing carbon nanotubes," *Macromolecules* **39** (16), 5194-5205 (2006).
- 13 Karen I. Winey, Takashi Kashiwagi, and Minfang Mu, "Improving electrical conductivity and thermal properties of polymers by the addition of carbon nanotubes as fillers," *Mrs Bulletin* **32** (4), 348-353 (2007).
- 14 L. L. Hench and J. K. West, "THE SOL-GEL PROCESS," *Chem. Rev.* **90** (1), 33-72 (1990).
- 15 B. L. Cushing, V. L. Kolesnichenko, and C. J. O'Connor, "Recent advances in the liquid-phase syntheses of inorganic nanoparticles," *Chem. Rev.* **104** (9), 3893-3946 (2004).

- 16 I. Gill and A. Ballesteros, "Encapsulation of biologicals within silicate, siloxane, and hybrid sol-gel polymers: An efficient and generic approach," *Journal of the American Chemical Society* **120** (34), 8587-8598 (1998).
- 17 B. Mahltig, H. Haufe, and H. Bottcher, "Functionalisation of textiles by inorganic sol-gel coatings," *J. Mater. Chem.* **15** (41), 4385-4398 (2005).
- 18 R. A. Caruso and J. H. Schattka, "Cellulose acetate templates for porous inorganic network fabrication," *Adv. Mater.* **12** (24), 1921-+ (2000).
- 19 B. C. Satishkumar, A. Govindaraj, M. Nath, and C. N. R. Rao, "Synthesis of metal oxide nanorods using carbon nanotubes as templates," *J. Mater. Chem.* **10** (9), 2115-2119 (2000).
- 20 R. A. Caruso, J. H. Schattka, and A. Greiner, "Titanium dioxide tubes from sol-gel coating of electrospun polymer fibers," *Adv. Mater.* **13** (20), 1577-+ (2001).
- 21 I. Ichinose, H. Senzu, and T. Kunitake, "A surface sol-gel process of TiO<sub>2</sub> and other metal oxide films with molecular precision," *Chemistry of Materials* **9** (6), 1296-& (1997).
- 22 R. A. Caruso, A. Susha, and F. Caruso, "Multilayered titania, silica, and Laponite nanoparticle coatings on polystyrene colloidal templates and resulting inorganic hollow spheres," *Chemistry of Materials* **13** (2), 400-409 (2001).
- 23 E. Donath, G. B. Sukhorukov, F. Caruso, S. A. Davis, and H. Mohwald, "Novel hollow polymer shells by colloid-templated assembly of polyelectrolytes," *Angew. Chem.-Int. Edit.* **37** (16), 2202-2205 (1998).

- 24 A. A. Mamedov, N. A. Kotov, M. Prato, D. M. Guldi, J. P. Wicksted, and A. Hirsch, "Molecular design of strong single-wall carbon nanotube/polyelectrolyte multilayer composites," *Nature Materials* **1** (3), 190-194 (2002).
- 25 Stephanie Vial, Isabel Pastoriza-Santos, Jorge Perez-Juste, and Luis M. Liz-Marzan, "Plasmon coupling in layer-by-layer assembled gold nanorod films," *Langmuir* **23** (8), 4606-4611 (2007).
- 26 F. Hua, T. H. Cui, and Y. M. Lvov, "Ultrathin cantilevers based on polymer-ceramic nanocomposite assembled through layer-by-layer adsorption," *Nano Lett.* **4** (5), 823-825 (2004).
- 27 Y. Lvov, K. Ariga, I. Ichinose, and T. Kunitake, "ASSEMBLY OF MULTICOMPONENT PROTEIN FILMS BY MEANS OF ELECTROSTATIC LAYER-BY-LAYER ADSORPTION," *Journal of the American Chemical Society* **117** (22), 6117-6123 (1995).
- 28 G. Decher, "Fuzzy nanoassemblies: Toward layered polymeric multicomposites," *Science* **277** (5330), 1232-1237 (1997).
- 29 C. S. Peyratout and L. Dahne, "Tailor-made polyelectrolyte microcapsules: From multilayers to smart containers," *Angew. Chem.-Int. Edit.* **43** (29), 3762-3783 (2004).
- 30 Jothi Sudagar, Jianshe Lian, and Wei Sha, "Electroless nickel, alloy, composite and nano coatings - A critical review," *Journal of Alloys and Compounds* **571**, 183-204 (2013).
- 31 V. M. Dubin, Y. ShachamDiamand, B. Zhao, P. K. Vasudev, and C. H. Ting, "Selective and blanket electroless copper deposition for ultralarge scale integration,"

- J. Electrochem. Soc. **144** (3), 898-908 (1997); Y. Kobayashi, V. Salgueirino-Maceira, and L. M. Liz-Marzan, "Deposition of silver nanoparticles on silica spheres by pretreatment steps in electroless plating," *Chemistry of Materials* **13** (5), 1630-1633 (2001).
- 32 H. Adachi, K. Taki, S. Nagamine, A. Yusa, and M. Ohshima, "Supercritical carbon dioxide assisted electroless plating on thermoplastic polymers," *Journal of Supercritical Fluids* **49** (2), 265-270 (2009).
- 33 F. Z. Kong, X. B. Zhang, W. Q. Xiong, F. Liu, W. Z. Huang, Y. L. Sun, J. P. Tu, and X. W. Chen, "Continuous Ni-layer on multiwall carbon nanotubes by an electroless plating method," *Surf. Coat. Technol.* **155** (1), 33-36 (2002).
- 34 G. H. Yang, E. T. Kang, K. G. Neoh, Y. Zhang, and K. L. Tan, "Surface graft copolymerization of poly(tetrafluoroethylene) films with N-containing vinyl monomers for the electroless plating of copper," *Langmuir* **17** (1), 211-218 (2001).
- 35 R. C. Foitzik, A. Kaynak, and F. M. Pfeffer, "Application of soluble poly (3-alkylpyrrole) polymers on textiles," *Synthetic Metals* **156** (7-8), 637-642 (2006).
- 36 Jadwiga Sojka-Ledakowicz, Joanna Lewartowska, Marcin Kudzin, Marcin Leonowicz, Teofil Jesionowski, Katarzyna Siwinska-Stefanska, and Andrzej Krysztafkiewicz, "Functionalization of textile materials by alkoxy silane-grafted titanium dioxide," *Journal of Materials Science* **44** (14), 3852-3860 (2009).
- 37 S. H. Feng and R. R. Xu, "New materials in hydrothermal synthesis," *Accounts of Chemical Research* **34** (3), 239-247 (2001).

- 38 T. Chirayil, P. Y. Zavalij, and M. S. Whittingham, "Hydrothermal synthesis of vanadium oxides," *Chemistry of Materials* **10** (10), 2629-2640 (1998).
- 39 J. G. Yu and X. X. Yu, "Hydrothermal synthesis and photocatalytic activity of zinc oxide hollow spheres," *Environmental Science & Technology* **42** (13), 4902-4907 (2008).
- 40 M. M. Titirici, M. Antonietti, and A. Thomas, "A generalized synthesis of metal oxide hollow spheres using a hydrothermal approach," *Chemistry of Materials* **18** (16), 3808-3812 (2006).
- 41 T. Ben Nasr, N. Kamoun, M. Kanzari, and R. Bennaceur, "Effect of pH on the properties of ZnS thin films grown by chemical bath deposition," *Thin Solid Films* **500** (1-2), 4-8 (2006).
- 42 P. K. Ghosh, M. K. Mitra, and K. K. Chattopadhyay, "ZnS nanobelts grown in a polymer matrix by chemical bath deposition," *Nanotechnology* **16** (1), 107-112 (2005); C. H. Ku, H. H. Yang, G. R. Chen, and J. J. Wu, "Wet-chemical route to ZnO nanowire-layered basic zinc acetate/ZnO nanoparticle composite film," *Crystal Growth & Design* **8** (1), 283-290 (2008); D. S. Dalavi, M. J. Suryavanshi, D. S. Patil, S. S. Mali, A. V. Moholkar, S. S. Kalagi, S. A. Vanalkar, S. R. Kang, J. H. Kim, and P. S. Patil, "Nanoporous nickel oxide thin films and its improved electrochromic performance: Effect of thickness," *Appl. Surf. Sci.* **257** (7), 2647-2656 (2011).

- 43 YuliyD Gamburg and Giovanni Zangari, "Introduction to Electrodeposition: Basic Terms and Fundamental Concepts", in *Theory and Practice of Metal Electrodeposition* (Springer New York, 2011), pp. 1-25.
- 44 K. Reichelt and X. Jiang, "THE PREPARATION OF THIN-FILMS BY PHYSICAL VAPOR-DEPOSITION METHODS," *Thin Solid Films* **191** (1), 91-126 (1990).
- 45 K. Sarakinos, J. Alami, and S. Konstantinidis, "High power pulsed magnetron sputtering: A review on scientific and engineering state of the art," *Surf. Coat. Technol.* **204** (11), 1661-1684 (2010).
- 46 V. S. Smentkowski, "Trends in sputtering," *Progress in Surface Science* **64** (1-2), 1-58 (2000).
- 47 Q. H. Fan, L. Q. Zhou, and D. Stevenson, "High rate sputtering deposition of silicon oxide thin films from new SiO<sub>2</sub>:Si target composition," *J. Vac. Sci. Technol. A* **27** (4), 979-985 (2009).
- 48 C. S. Deng, H. E. Assender, F. Dinelli, O. V. Kolosov, G. A. D. Briggs, T. Miyamoto, and Y. Tsukahara, "Nucleation and growth of gas barrier aluminium oxide on surfaces of poly(ethylene terephthalate) and polypropylene: Effects of the polymer surface properties," *J. Polym. Sci. Pt. B-Polym. Phys.* **38** (23), 3151-3162 (2000).
- 49 Y. Dietzel, W. Przyborowski, G. Nocke, P. Offermann, F. Hollstein, and J. Meinhardt, "Investigation of PVD arc coatings on polyamide fabrics," *Surf. Coat. Technol.* **135** (1), 75-81 (2000).
- 50 Anthony C. Jones and Michael L. Hitchman (eds), *Chemical Vapour Deposition: Precursors, Processes and Applications*. (RSC Publishing, 2009).

- 51 K. L. Choy, "Chemical vapour deposition of coatings," *Progress in Materials Science* **48** (2), 57-170 (2003).
- 52 Schwartz Geraldine Cogin, "Methods/Principles of Deposition and Etching of Thin Films", in *Handbook of Semiconductor Interconnection Technology, Second Edition* (CRC Press, 2006), pp. 1-62.
- 53 M. J. Hampdensmith and T. T. Kodas, "CHEMICAL-VAPOR-DEPOSITION OF METALS .1. AN OVERVIEW OF CVD PROCESSES," *Chem. Vapor Depos.* **1** (1), 8-23 (1995).
- 54 S. M. George, "Atomic Layer Deposition: An Overview," *Chem. Rev.* **110** (1), 111-131 (2010).
- 55 R. L. Puurunen, "Surface chemistry of atomic layer deposition: A case study for the trimethylaluminum/water process," *J. Appl. Phys.* **97** (12), 52 (2005).
- 56 M. Knez, K. Niesch, and L. Niinisto, "Synthesis and surface engineering of complex nanostructures by atomic layer deposition," *Adv. Mater.* **19** (21), 3425-3438 (2007);  
M. D. Groner, F. H. Fabreguette, J. W. Elam, and S. M. George, "Low-temperature Al<sub>2</sub>O<sub>3</sub> atomic layer deposition," *Chemistry of Materials* **16** (4), 639-645 (2004).
- 57 Q. Peng, X. Y. Sun, J. C. Spagnola, G. K. Hyde, R. J. Spontak, and G. N. Parsons, "Atomic layer deposition on electrospun polymer fibers as a direct route to Al<sub>2</sub>O<sub>3</sub> microtubes with precise wall thickness control," *Nano Lett.* **7** (3), 719-722 (2007).
- 58 C. J. Oldham, B. Gong, J. C. Spagnola, J. S. Jur, K. J. Senecal, T. A. Godfrey, and G. N. Parsons, "Encapsulation and Chemical Resistance of Electrospun Nylon

- Nanofibers Coated Using Integrated Atomic and Molecular Layer Deposition," *J. Electrochem. Soc.* **158** (9), D549-D556 (2011).
- 59 E. Santala, M. Kemell, M. Leskela, and M. Ritala, "The preparation of reusable magnetic and photocatalytic composite nanofibers by electrospinning and atomic layer deposition," *Nanotechnology* **20** (3) (2009).
- 60 W. S. Kim, B. S. Lee, D. H. Kim, H. C. Kim, W. R. Yu, and S. H. Hong, "SnO<sub>2</sub> nanotubes fabricated using electrospinning and atomic layer deposition and their gas sensing performance," *Nanotechnology* **21** (24) (2010).
- 61 J. C. Spagnola, B. Gong, S. A. Arvidson, J. S. Jur, S. A. Khan, and G. N. Parsons, "Surface and sub-surface reactions during low temperature aluminium oxide atomic layer deposition on fiber-forming polymers," *J. Mater. Chem.* **20** (20), 4213-4222 (2010).
- 62 M. D. Groner, S. M. George, R. S. McLean, and P. F. Carcia, "Gas diffusion barriers on polymers using Al<sub>2</sub>O<sub>3</sub> atomic layer deposition," *Appl. Phys. Lett.* **88** (5) (2006);  
A. A. Dameron, S. D. Davidson, B. B. Burton, P. F. Carcia, R. S. McLean, and S. M. George, "Gas diffusion barriers on polymers using multilayers fabricated by Al<sub>2</sub>O<sub>3</sub> and rapid SiO<sub>2</sub> atomic layer deposition," *J. Phys. Chem. C* **112** (12), 4573-4580 (2008).
- 63 K. Lee, J. S. Jur, D. H. Kim, and G. N. Parsons, "Mechanisms for hydrophilic/hydrophobic wetting transitions on cellulose cotton fibers coated using Al<sub>2</sub>O<sub>3</sub> atomic layer deposition," *J. Vac. Sci. Technol. A* **30** (1) (2012); G. K. Hyde, G. Scarel, J. C. Spagnola, Q. Peng, K. Lee, B. Gong, K. G. Roberts, K. M.

- Roth, C. A. Hanson, C. K. Devine, S. M. Stewart, D. Hojo, J. S. Na, J. S. Jur, and G. N. Parsons, "Atomic Layer Deposition and Abrupt Wetting Transitions on Nonwoven Polypropylene and Woven Cotton Fabrics," *Langmuir* **26** (4), 2550-2558 (2010).
- 64 W. J. Sweet, J. S. Jur, and G. N. Parsons, "Bi-layer Al<sub>2</sub>O<sub>3</sub>/ZnO atomic layer deposition for controllable conductive coatings on polypropylene nonwoven fiber mats," *J. Appl. Phys.* **113** (19) (2013).
- 65 B. Gong, Q. Peng, J. S. Jur, C. K. Devine, K. Lee, and G. N. Parsons, "Sequential Vapor Infiltration of Metal Oxides into Sacrificial Polyester Fibers: Shape Replication and Controlled Porosity of Microporous/Mesoporous Oxide Monoliths," *Chemistry of Materials* **23** (15), 3476-3485 (2011).
- 66 B. Gong and G. N. Parsons, "Quantitative in situ infrared analysis of reactions between trimethylaluminum and polymers during Al<sub>2</sub>O<sub>3</sub> atomic layer deposition," *J. Mater. Chem.* **22** (31), 15672-15682 (2012).
- 67 J. S. Jur, J. C. Spagnola, K. Lee, B. Gong, Q. Peng, and G. N. Parsons, "Temperature-Dependent Subsurface Growth during Atomic Layer Deposition on Polypropylene and Cellulose Fibers," *Langmuir* **26** (11), 8239-8244 (2010).
- 68 H. I. Akyildiz, R. P. Padbury, G. N. Parsons, and J. S. Jur, "Temperature and Exposure Dependence of Hybrid Organic-Inorganic Layer Formation by Sequential Vapor Infiltration into Polymer Fibers," *Langmuir* **28** (44), 15697-15704 (2012).
- 69 S. M. Lee, E. Pippel, U. Gosele, C. Dresbach, Y. Qin, C. V. Chandran, T. Brauniger, G. Hause, and M. Knez, "Greatly Increased Toughness of Infiltrated Spider Silk," *Science* **324** (5926), 488-492 (2009).

- 70 A. K. Geim and K. S. Novoselov, "The rise of graphene," *Nature Materials* **6** (3), 183-191 (2007).
- 71 H. Qian, E. S. Greenhalgh, M. S. P. Shaffer, and A. Bismarck, "Carbon nanotube-based hierarchical composites: a review," *J. Mater. Chem.* **20** (23), 4751-4762 (2010).
- 72 D. Eder, "Carbon Nanotube-Inorganic Hybrids," *Chem. Rev.* **110** (3), 1348-1385 (2010); W. D. Zhang, B. Xu, and L. C. Jiang, "Functional hybrid materials based on carbon nanotubes and metal oxides," *J. Mater. Chem.* **20** (31), 6383-6391 (2010).
- 73 Peter J.F. Harris, *Carbon Nanotube Science*. (Cambridge University Press, New York, 2009).
- 74 Zhidong Han and Alberto Fina, "Thermal conductivity of carbon nanotubes and their polymer nanocomposites: A review," *Progress in Polymer Science* **36** (7), 914-944 (2011).
- 75 Andrew S. Cavanagh, Christopher A. Wilson, Alan W. Weimer, and Steven M. George, "Atomic layer deposition on gram quantities of multi-walled carbon nanotubes," *Nanotechnology* **20** (25) (2009).
- 76 Luckshitha Suriyasena Liyanage, Daire J. Cott, Annelies Delabie, Sven Van Elshocht, Zhenan Bao, and H. S. Philip Wong, "Atomic layer deposition of high-k dielectrics on single-walled carbon nanotubes: a Raman study," *Nanotechnology* **24** (24) (2013).
- 77 Lifei Chen and Huaqing Xie, "Surfactant-free nanofluids containing double- and single-walled carbon nanotubes functionalized by a wet-mechanochemical reaction," *Thermochimica Acta* **497** (1-2), 67-71 (2010); Ting Shu, Shi-Jun Liao, Chien-

- Te Hsieh, Anup Kumar Roy, Yung-Ying Liu, Dong-Ying Tzou, and Wei-Yu Chen, "Fabrication of platinum electrocatalysts on carbon nanotubes using atomic layer deposition for proton exchange membrane fuel cells," *Electrochimica Acta* **75**, 101-107 (2012).
- 78 D. B. Farmer and R. G. Gordon, "Atomic layer deposition on suspended single-walled carbon nanotubes via gas-phase noncovalent functionalization," *Nano Lett.* **6** (4), 699-703 (2006).
- 79 J. A. McCormick, B. L. Cloutier, A. W. Weimer, and S. M. George, "Rotary reactor for atomic layer deposition on large quantities of nanoparticles," *J. Vac. Sci. Technol. A* **25** (1), 67-74 (2007).
- 80 David M. King, Joseph A. Spencer, II, Xinhua Liang, Luis F. Hakim, and Alan W. Weimer, "Atomic layer deposition on particles using a fluidized bed reactor with in situ mass spectrometry," *Surf. Coat. Technol.* **201** (22-23), 9163-9171 (2007).

## CHAPTER 2. Experimental Tools

### 2.1 Atomic Layer Deposition

Atomic layer deposition was done in homebuilt hot-walled viscous flow reactors. Figure 2.1 shows a schematic of the reactor. The reactants used were trimethyl aluminum (TMA, STREM Chemicals, 98%), diethyl zinc (DEZ, STREM Chemicals, 95%), titanium tetrachloride ( $\text{TiCl}_4$ , Gelest, 99%), and titanium (IV) isopropoxide (TIP, Acros Organics, 98%). The oxidizing precursor was deionized water. The operating pressure was  $\sim 3$  Torr. Nitrogen ( $\text{N}_2$ , 99.999%) was used as a carrier gas. The carrier gas was further purified to remove any remaining water by passing it through an Aeronex Gatekeeper gas purification system. A typical ALD recipe for TMA/ $\text{H}_2\text{O}$  and  $\text{TiCl}_4/\text{H}_2\text{O}$  was 0.1/45/0.1/30s corresponding to TMA or  $\text{TiCl}_4/\text{N}_2/\text{H}_2\text{O}/\text{N}_2$ . The precursor doses were increased to 0.2s for the deposition of zinc oxide. All precursors were stored in separate steel bottles, except for TIP which was in a glass bubbler. The TIP recipe included a preparation step in which carrier gas was dosed into the bubbler to volatize the TIP before dosing. The addition of the preparation step changed the recipe to 2/0.5/30/0.1/30s corresponding to TIP Prep/TIP/ $\text{N}_2/\text{H}_2\text{O}/\text{N}_2$ . Hold steps were also used when coating carbon nanotubes and for the promotion of precursor diffusion into polymer substrates. In the hold steps, precursors were dosed to the reactor chamber and then the reactor was isolated from the pump for a certain hold time before being purged. The ALD valves were controlled using Lab View software. The reactor was heated using heating tape (Omega) controlled using several variacs.

The graph of the growth rate for the chemistries deposited at 105°C is shown in Figure 2.2. The growth rate as measured by ellipsometry on silicon wafers, was  $1.190 \pm 0.005$ ,  $1.6 \pm 0.2$ ,  $0.45 \pm .07$ ,  $0.26 \pm .03$  Å/cycle for aluminum oxide, zinc oxide, and titanium dioxide using  $\text{TiCl}_4/\text{H}_2\text{O}$  and  $\text{TIP}/\text{H}_2\text{O}$  respectfully. The ALD film thicknesses versus the number of ALD cycles all show linear trends as would be expected for the self-limiting nature of the chemistry.

## **2.2 Material Preparation**

### **2.2.1 Electrospinning**

A NESSE electrospinning set-up from Innovative Systems Design was used to create nanofibers. The high voltage power supply was set to 20 kV, and the syringe pump was set to approximately 250  $\mu\text{L}$  to keep a pressure of 2-3 psi on the solution. A 26-gauge needle with a blunt end was used for electrospinning. The distance between the high voltage needle and the grounded 10" diameter collector plate was  $\sim 5.5$ ". The collector plate was wrapped with Reynolds Wrap Nonstick aluminum foil for fiber collection. Dry gas was set to flow parallel to the needle, and the flow rate was approximately 2-3 liters/min. In addition to the dry gas, a jet gas flow was directed at the point of the tip at an angle of approximately 45°, and the flow rate was 4-5 liter/min. The jet gas can be used to direct the fiber stream to ensure the entire collector is being coated.

### **2.2.2 Melt Pressing**

Polymer beads were melt-pressed into dog bone shapes for mechanical testing. The dog bones were shaped according to ASTM standard D638 and had a thickness of  $\sim 0.345$

mm. Nylon 6, high molecular weight polypropylene and Pellethane 2363-55D were pressed at 210°C. Low molecular weight polypropylene was pressed at 160°C. Polyethylene oxide was melt pressed at 90°C and 100°C for low and high molecular weight respectively. After pressing the samples were cooled between metal plates.

### **2.2.3 Carbon Nanotube Preparation**

Two different approaches were explored for supporting and containing the nanotubes for deposition: (i) fiber bundle and (ii) fiber basket (or fiber wrapping) carrier structures. For the fiber bundle approach, carbon nanotubes were suspended in a 0.5 wt % carbon nanotubes were suspended in a methanol solution and sonicated for ~15 min until uniformly dispersed by visual inspection. Using a syringe, approximately 6mL of the suspension was dripped onto ~250mg quartz wool bundles (Leco Corporation) or cosmetic-grade cotton fiber balls. Upon loading the fiber bundles with nanotubes, the bundles visibly changed from bright white to black in the regions wetted by solution. After being loaded, the fiber bundles were allowed to dry at room temperature for more than 24 h before being transferred to the ALD reactor. For the fiber basket method, a screen made of metal wires with ~0.7 mm diameter in a 1.5 mm square grid pattern was formed into a cylindrical scaffold that was approximately 3 cm long and 2 cm in diameter and then wrapped with either a nonwoven polypropylene (PP) fiber mat or a woven cotton fiber cloth. The nonwoven PP fiber materials were obtained from NC State College of Textiles, and the cotton was obtained from Textile Innovators. They were used as received. The fiber sheet and Kapton tape secure the nanotubes in the basket. Each basket was loaded with approximately 30-50 mg of nanotubes before being enclosed using polyimide film tape. To avoid user exposure to nanotubes, all carbon nanotube

handling, storage, and transfer to the fiber carriers was performed in a benchtop nitrogen purged glovebox (LC Technology Solutions).

## **2.3 Mechanical Testing**

### **2.3.1 Instron Tensile Testing**

The mechanical properties of the polymer dog bones were measured using an Instron 5943 Tensile tester equipped with a 1 kN load cell and pneumatic grips. The gauge length was 2.5 cm and the crosshead speed was set to 25 mm/min. The samples were strained until failure which the stress was measured. For each data point 5 samples were tested.

Mechanical tensile testing of the fiber mats was done using same Instron equipped with a 10 N load cell. The crosshead speed was set to 10 mm/min. The gauge length was 2.5 cm. The nylon mats were loaded onto the grips, the sides of the cardstock frame were cut and then mats were measured under strain until failure. The modulus of the tested samples was calculated by measuring the slope of the initial linear portion of the stress strain curve. The collected tensile data is normalized to the mass of the starting fiber mat.

### **2.3.2 Nanoindentation by Atomic Force Microscopy**

Imaging and nanoindentation was done using a Cypher AFM from Asylum. The nanoindentation was done while in contact mode. Diamond coated AFM tips purchased from Nanoworld were used for indentation. The spring constant for the tips was determined using the Sader method<sup>1</sup>. The IGOR software using the Hertz model was used to calculate the modulus from the force curves collected. The poisson ratio for nylon was assumed to be 0.35<sup>2</sup> and that for the indenter and the silicon to be 0.2. The modulus for the indenter was

estimated to be 865 GPa with a radius of 81 nm. The tip property values were calibrated using nanoindentation on a quartz substrate with a known modulus. The force curves were generally collected using a trigger point of 1V. The amplitude modulated frequency modulated (AM-FM) force mapping was done using an Asylum MFP-3D.

## **2.4 Materials Characterization**

### **2.4.1 Fourier Transform Infrared Spectroscopy**

The chemical composition of the nylon fiber mats was assessed using Fourier transform infrared spectroscopy (FTIR) and X-ray photoelectron spectroscopy (XPS). The FTIR used was a Thermo Nicolet Magna 750, equipped with a nonpolarized IR beam, a KBr beamsplitter, and a deuterated triglycine sulfate detector. To see how each processing step affected the chemical composition of the samples, the spectrum from the previous step was subtracted from the current step.

### **2.4.2 X-Ray Photoelectron Spectroscopy**

The surface of the fibers was analyzed with X-ray photoelectron spectroscopy (XPS) using either a Riber XPS-3000 or a SPECS XPS, both equipped with an Mg anode source. The scans were calibrated by referencing to adventitious carbon at ~285 eV. The XPS studies were done at the AIF at NC State University.

### **2.4.3 Transmission Electron Microscopy**

Cross-sectional transmission electron microscopy (TEM) images of nanofibers and films were collected at the Analytical Instrumentation Facility (AIF) at North Carolina State

University. The samples were first microtomed at AIF and then imaged with a Hitachi HF2000 TEM was used with an accelerating voltage of 200 kV and a FE Tungsten source. TEM images of carbon nanotubes were collected using a Tecnai G<sup>2</sup> Twin or a Hitachi HF2000 equipped with an Oxford Link INCA energy-dispersive spectroscopy system.

#### **2.4.4 Scanning Electron Microscopy**

The morphology of nanofiber was analyzed using scanning electron microscopy (SEM). The SEM images were obtained at the NC State University Analytical Instrumentation Facility using a JEOL 6400F field emission SEM and at the Shared Materials Instrumentation Facility at Duke University using a FEI XL30 SEM. Before imaging, the fibers were sputter coated using a Quorum Technologies Mini Sputter Coater (Model SC7620) equipped with a gold/palladium target. The current was set to ~20 mA and the samples were sputtered for approximately 90 seconds.

#### **2.4.5 Ellipsometry**

Ellipsometry was used to measure the ALD film thickness on the silicon wafers used to monitor film growth. The ellipsometer used was a variable angle Alpha-SE from J.A. Woollam Co., Inc.

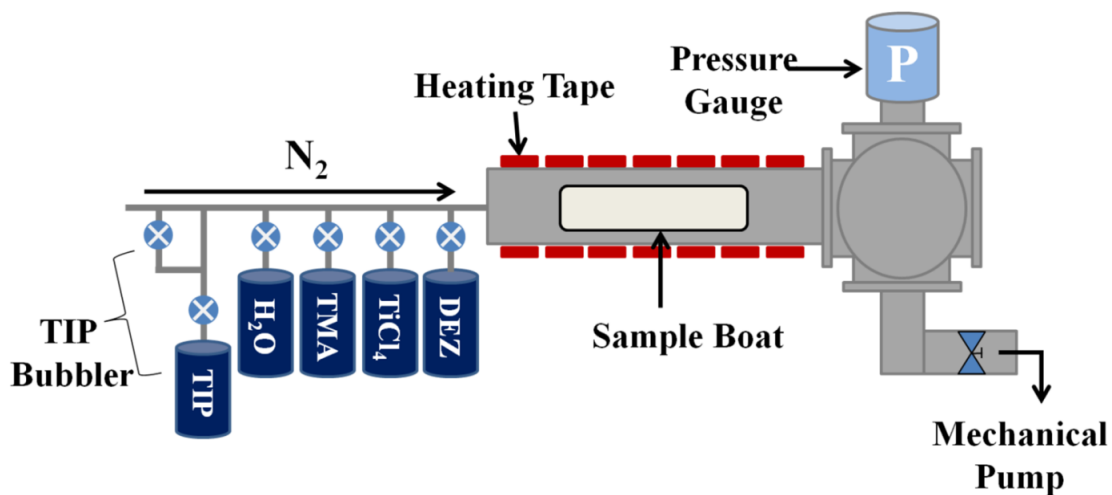


**Figure 2.1:** Schematic of hot-walled viscous flow reactor used for ALD of metal oxide thin films.

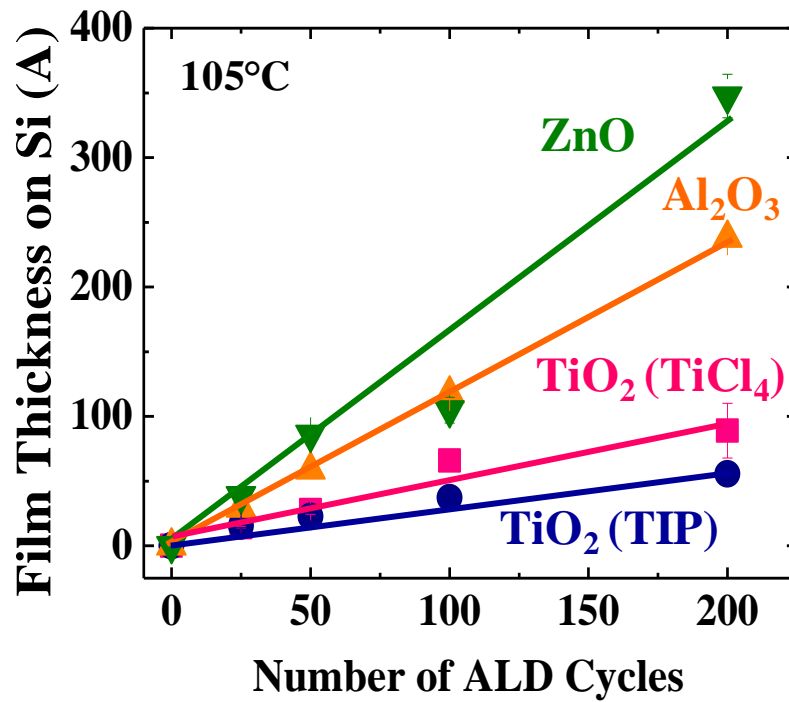


**Figure 2.2:** Growth rate of ALD deposited zinc oxide, aluminum oxide, and titanium dioxide via TiCl<sub>4</sub> or TIP thin films on silicon at 105°C. For all precursors the growth is linear as is expected for ALD.

## References

- 1 J. E. Sader, J. W. M. Chon, and P. Mulvaney, "Calibration of rectangular atomic force microscope cantilevers," *Rev. Sci. Instrum.* 70 (10), 3967-3969 (1999).
- 2 L. Shen, W. C. Tjiu, and T. X. Liu, "Nanoindentation and morphological studies on injection-molded nylon-6 nanocomposites," *Polymer* 46 (25), 11969-11977 (2005).

## **CHAPTER 3. Overview of Key Results of the Dissertation**

This dissertation explores using atomic layer deposition to coat carbon nanotubes and polymer materials including nanofibers and films. The growth and nucleation of thin films deposited using atomic layer deposition was explored as well as the effect of these thin films on the mechanical properties of the substrates. The effects of precursor choice, precursor exposure time, and substrate chemistry were investigated to understand how the mechanical properties of ALD functionalized materials may be tuned for advanced performance.

### **3.1 Fiber Containment for Improved Laboratory Handling and Uniform Nanocoating of Milligram Quantities of Carbon Nanotubes by Atomic Layer Deposition**

This work focused on the importance of safe practices for nanomaterials handling and investigating new methods of coating nanopowders with atomic layer deposition. We explored both fiber bundles and fiber baskets as possible containment methods and conclude that the baskets are more suitable for coating studies. For the basket approach polypropylene or cotton fiber mats are wrapped around a metal grid scaffold to contain carbon nanotubes for ALD coating. The procedure yields uniform coatings on milligram quantities of nanotubes using a conventional viscous flow reactor system, circumventing the need for specialized fluidized bed or rotary ALD reactors for laboratory-scale studies. Extended precursor dose and soak periods consisting of a 5s TMA dose, a 60s soak, and a 90s purge were required to allow the gases to diffuse through the fiber containment to uniformly coat the carbon nanotubes. Multiwall carbon nanotubes coated using the cotton wrapped basket method and extended doses are pictured in Figure 3.1. The films are uniform and conformal on the

nanotube surface without the requirement of added functionalization. The film thickness scaled linearly with the number of ALD cycles as shown in Figure 3.2. Thicker coatings were deposited using the extended precursor dose and soak periods compared to typical doses on CNT controls not encased in the fibers, suggesting some effects due to the extended reactant dose. When using the basket approach with a traditional ALD recipe of 1/30/1/30s corresponding to TMA/N<sub>2</sub>/H<sub>2</sub>O/N<sub>2</sub>, the film thickness was not uniform indicating the longer dose and soak sequence may be required for uniform film thickness. The nanotubes coated with 50 cycles of the traditional ALD recipe had coatings ranging from 0-4 nm compared to the uniform film thickness of 5 nm seen when using extended precursor dose and soak periods. Film growth was compared on a range of single-walled NTs, double-walled NTs, and acid-functionalized multiwall NTs, and we found that ultrathin coatings were most readily controlled on the multiwall NTs. The single-walled and double-walled NTs showed nodular growth of aluminum oxide. The alumina nodules likely nucleated at the defect sites on the nanotubes. The acid functionalized nanotubes had uniform growth similar to the multiwall nanotubes.

This work is described in detail in Chapter 4, and was published as C. K. Devine, C. J. Oldham, J. S. Jur, B. Gong and G. N. Parsons, *Langmuir* **27** (23), 14497-14507 (2011).

### **3.2 Atomic Layer Deposition of Zinc Oxide on Multiwall Carbon Nanotubes**

The fiber containment methods outlined in section 3.1 were used to coat MWCNTs with zinc oxide (ZnO) using diethyl zinc (DEZ) and water. The precursor doses were 5s and the soak and purge steps were elongated to 120s. The average film thickness scaled linearly

with the number of ALD cycles with a growth rate of  $\sim 2 \text{ \AA}/\text{cycle}$ . The deposited films have rough surfaces as shown in Figure 3.3. The ZnO nucleates at the defect sites of the nanotubes and as the number of ALD cycles is increased the nuclei coalesce to form a roughened film. The ZnO growth on the nanotubes is variable, with some nanotubes exhibiting no growth, some in the nucleation stage, and others with full thick films. As a control, MWCNTs were also loaded onto TEM grids and coated using a 2/50/2/50s recipe corresponding to DEZ/N<sub>2</sub>/H<sub>2</sub>O/N<sub>2</sub>. The growth rate on the grid loaded samples was  $\sim 1.5 \text{ \AA}/\text{cycle}$  and the ZnO film growth is uniform with all nanotubes having the same degree of coating. The difference in growth rate indicates that the fiber wrapping is causing elevated growth. While a growth rate of  $\sim 2 \text{ \AA}/\text{cycle}$  is typical for ZnO on planar substrates such as silicon, the CNTs do not have the same density of reactive sites as silicon and we would expect the growth rate to be delayed. Additionally, the lack of film variability on the grid loaded samples indicates the basket method may be preventing the ALD precursors from diffusing throughout the CNT powder. The larger size of the DEZ molecule compared to the TMA studied in section 3.1 may hinder diffusion through the cotton fiber wrapping or through the CNT powder. Altering the ALD recipe by increasing the soak period or using multiple DEZ dose/soak periods followed by the water sequence may improve uniformity by adding excess precursor and increasing the time for diffusion. Decreasing the quantity of nanotubes coated in each deposition may also facilitate movement by decreasing the packing density in the basket.

This work is described in more detail in the thesis in Chapter 5. The Chapter may be revised for publication in the future.

### **3.3 Large Effect of Titanium Precursor on Surface Reactivity and Mechanical Strength of Electrospun Nanofibers Coated with TiO<sub>2</sub> by Atomic Layer Deposition**

In this work, the mechanical properties of bare and ALD coated electrospun nylon nanofibers were explored. We deposited aluminum oxide, zinc oxide, and titanium dioxide on the nylon fibers. Two titania precursors were used for coating, titanium isopropoxide (TIP) or titanium tetrachloride (TiCl<sub>4</sub>). The deposition of aluminum oxide and titanium dioxide via the TiCl<sub>4</sub>/H<sub>2</sub>O reaction greatly increased the modulus of the nanofibers as shown in Figure 3.4. The increase in modulus with these coatings was also accompanied by a decrease in the amount of strain they could withstand until breaking. The zinc oxide and titanium dioxide film using TIP/H<sub>2</sub>O did not change the modulus and only slightly decreased the strain at break for the fiber mats. An increase in modulus and decrease in the strain at break would be expected for the addition of metal oxide coating as it is more ceramic in nature compared to the polymer. The difference in the mechanical properties is ascribed to the different chemical interactions between the precursors. Using FTIR, a large chemical change was observed after only 10 cycles of TiCl<sub>4</sub>/H<sub>2</sub>O ALD compared to the TIP treated fibers. The Ti-O FTIR peaks were not detected until 100 cycles of TIP/H<sub>2</sub>O ALD indicating decreased reactivity when compared to TiCl<sub>4</sub>. Using XPS it was observed that after 100 ALD cycles the nitrogen signal is near the XPS sensitivity limit (~0.5%) for the nylon coated using TiCl<sub>4</sub>/H<sub>2</sub>O, whereas N is readily observed after coating with TIP/H<sub>2</sub>O. This indicates that after 100 cycles the TiCl<sub>4</sub>/H<sub>2</sub>O coated samples have a TiO<sub>2</sub> film thick enough so that the XPS cannot detect the nitrogen signal from the underlying polymer, whereas it requires more than 200 cycles for the TIP/H<sub>2</sub>O treated fibers to mask the nitrogen signal. This is consistent

with the IR results showing more coating using  $\text{TiCl}_4/\text{H}_2\text{O}$  compared to  $\text{TIP}/\text{H}_2\text{O}$  ALD. Using TEM, it was seen that the  $\text{TiCl}_4$  diffused into the nylon-6 and reacted subsurface, whereas the titanium isopropoxide tended to react on the surface producing a more abrupt organic/inorganic interface. Results show that precursor choice is an important factor when designing thin film coating processes on polymeric substrates.

In the thesis, Chapter 6 covers this work more completely. It is being published as C. D. McClure, C. J. Oldham, H. J. Walls, and G. N. Parsons, (in press) *J. Vac. Sci. Technol.*, A.

### **3.4. AFM Nanoindentation on ALD Coated Electrospun Nylon Nanofibers**

In this work, nylon 6 fibers were electrospun onto silicon wafers for AFM nanoindentation. The samples were coated with either aluminum oxide or titanium dioxide using atomic layer deposition. For titanium dioxide deposition either titanium tetrachloride ( $\text{TiCl}_4$ ) or titanium isopropoxide (TIP) were used as the titanium containing precursor. Aluminum oxide was deposited using TMA and water as the precursors. The elastic modulus of the nanofibers and the silicon substrates was measured using AFM nanoindentation. Figure 3.5 shows the results for the change in elastic modulus with increasing metal oxide film thickness. The elastic modulus of the nylon nanofibers increases with increasing cycle number for the samples coated with aluminum oxide and for the samples coated with titanium dioxide via  $\text{TiCl}_4/\text{H}_2\text{O}$ . The elastic modulus for the samples coated with titanium dioxide via  $\text{TIP}/\text{H}_2\text{O}$  does not increase. The results in Figure 3.5 correlate well with the results shown in section 3.3. The results for the elastic modulus on

the silicon substrates are also shown in Figure 3.5. The modulus for the  $\text{TiCl}_4/\text{H}_2\text{O}$  coated sample show an increase in elastic modulus, however more data points are require to determine the validity of this trend. It was also possible to indent through the ALD film, causing plastic deformation and leave a cantilever tip-shaped form in the nanofibers. By carefully controlling the AFM parameters it may be possible to measure the force required for film cracking using this method. This work also demonstrates the ability for AFM to map the stiffness of a sample cross-section using Amplitude-Modulated Frequency-Modulated (AMFM) AFM methods. The AMFM map of the cross-section of a sample coated with 100 cycles of  $\text{TiCl}_4/\text{H}_2\text{O}$  is shown in Figure 3.6 along with the energy dissipation graph associated with the image. The sample was embedded in epoxy before microtoming. The softer nylon nanofibers are the darker circles in the sample and are surrounded by a bright white coating associated with the stiff titania layer. The color change in the image correlates well to the dissipation graph below, with peaks and dips corresponding to the titania coating and polymer respectively. Using this technique may be an excellent method for accessing subsurface growth and coating uniformity.

This work is described in more detail in the thesis in Chapter 7. The Chapter may be revised for publication in the future.

### **3.5 Effect of ALD Processing Parameters on Film Growth and Mechanical Properties of Polymer Films**

In this work subsurface growth was investigated using polymers with reactive centers, nylon 6 and Pellethane 2363-55D (P55D) as well as relatively inert polypropylene as

substrates. The polymers were coated with aluminum oxide using TMA and water as precursors. Three ALD recipes were used to coat the polymer substrates. The traditional ALD recipe consists of short precursor exposures separated by an inert gas purge. A recipe with extended precursor exposures and soaks was used termed an ALD-Hold recipe. The third recipe was a multipulse recipe in which the sample was exposed to a short dose of TMA followed by a soak and purge period. The TMA dose was repeated 9 times and then followed by one dose, soak, and purge cycle of water. The 9 TMA exposures followed by 1 H<sub>2</sub>O exposure constitute one multipulse cycle. The different recipes were used to analyze the effect of the precursor exposure on growth in the polymer subsurface region as well as the effect on the mechanical properties of the polymer films. The subsurface growth was analyzed using cross-sectional TEM as shown in Figure 3.7 and listed in Table 3.1. The subsurface growth on the substrates treated with the traditional ALD recipe is easily visible and change depending on temperature. The ALD precursors diffused the farthest into the P55D samples and showed the most distinct interface. No subsurface growth is observed with the samples treated using the hold recipe with extended precursor doses and soaks. The lack of visible subsurface growth could indicate that reactions occurred at the surface preventing diffusion or more likely, that the precursors diffused through the sample making it difficult to see in the contrast of the TEM images.

The elastic modulus increases with increasing film thickness for nylon treated with the traditional ALD recipe. Similar results are seen for polypropylene treated at 100°C and P55D. The samples treated with the ALD-Hold recipe show similar trends but have a greater increase in the case of both nylon and polypropylene. The elastic modulus for P55D is

dependent on temperature with the samples treated at 50°C for the traditional ALD and ALD-Hold recipe having the largest increase. The nylon and polypropylene samples treated using the multipulse recipe have results nearly equivalent to the samples treated using the hold recipe. The multipulse recipe requires less processing time and may be an easier method of achieving the same increase in mechanical performance.

We also investigated the effect of polymer molecular weight on the mechanical properties of ALD treated polypropylene and polyethylene oxide (PEO). The samples were coated with aluminum oxide using the traditional ALD recipe. The elastic modulus increases with increasing film thickness for low molecular weight PEO, but there is little change for the higher molecular weight PEO. In the case of the polypropylene, there was little change for either low or high molecular weight. The TMA likely reacts with the PEO polymer chains which may lead to chain scission compared to PP in which very little reaction occurs. The low molecular weight has shorter polymer chains, indicating a greater number of reactive hydroxyl chain ends. It is likely that with more reactive sites available there will be more aluminum oxide deposition in the case of the low molecular weight PEO and a correspondingly greater affect on the mechanical properties.

Chapter 8 describes this work more fully, and the text in Chapter 8 is currently being edited in preparation for publication.

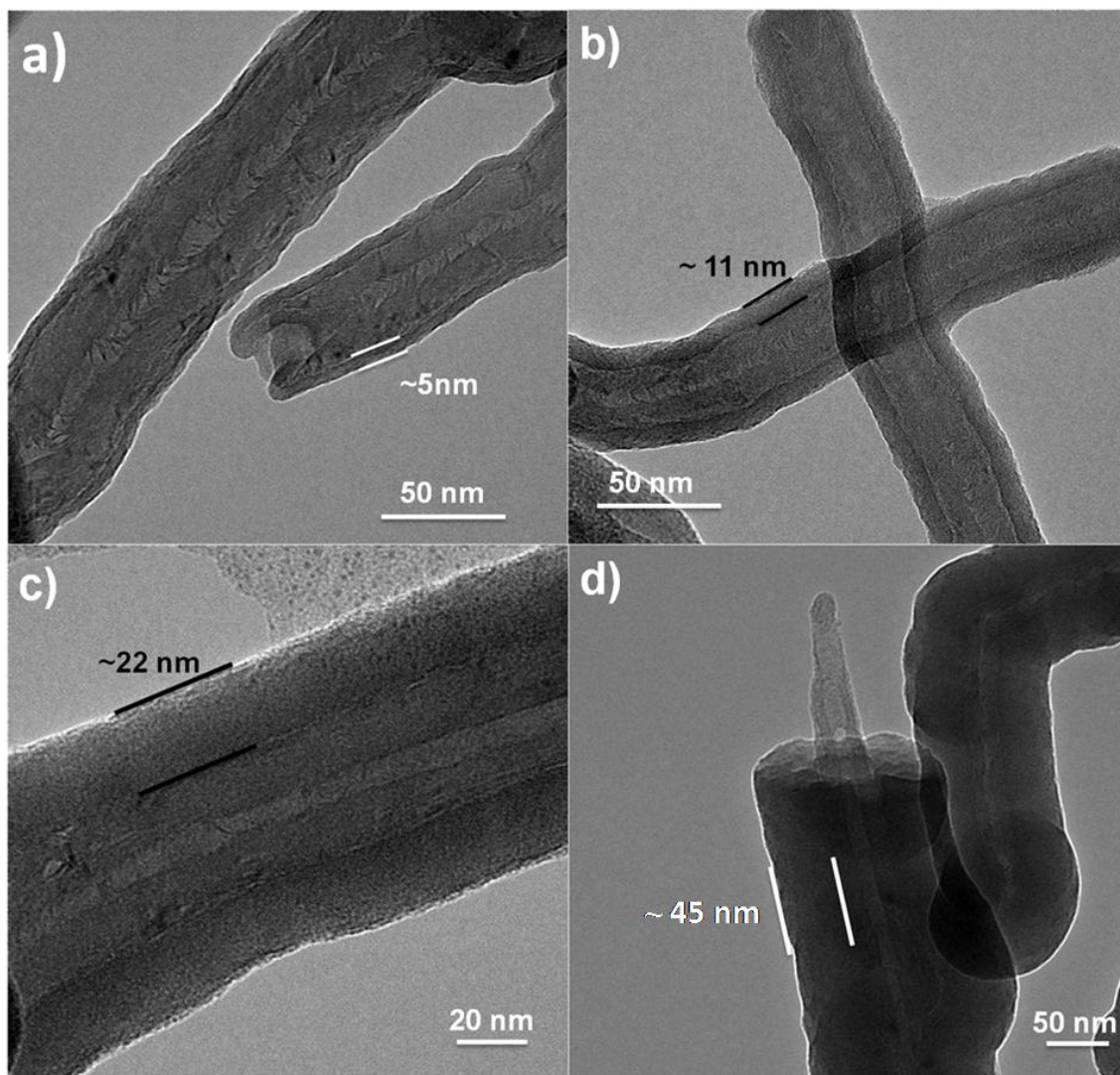


**Figure 3.1:** TEM images of MWNTs coated with a) 25; b) 50; c) 100; and d) 200 cycles Al<sub>2</sub>O<sub>3</sub> ALD at 90°C using the cotton wrapped basket method. The coating thickness increased linearly with cycle number. Several uncoated or broken ends were observed as shown in panel (d). In other images (not shown), the number of visible broken ends increases as the coating thickness increases.

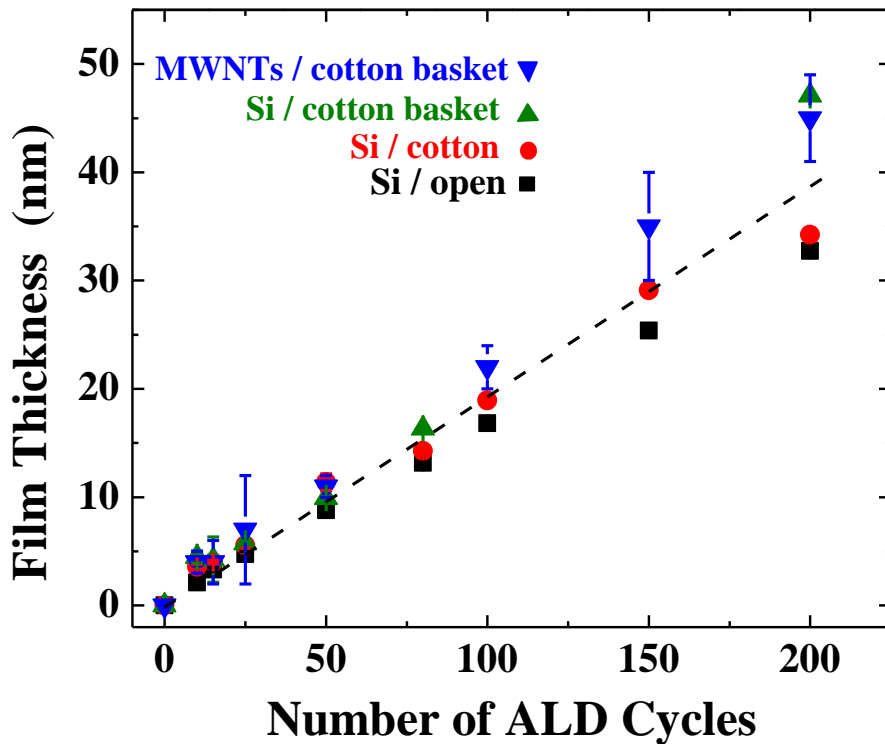


**Figure 3.2:** Graph comparing ALD growth on Si wafers and MWNTs where the substrates (Si and nanotubes) are encased in cotton fiber baskets. The plot also includes thickness measured on silicon when the substrate is directly wrapped in cotton (without the basket) (labeled “Si / cotton”) and when no fiber containment is present (labeled “Si / open”). The growth increases linearly with cycle number at about the same rate observed for fibers encased in polypropylene. The film thickness on all substrates follows a similar trend, with some deviation present for larger number of cycles.

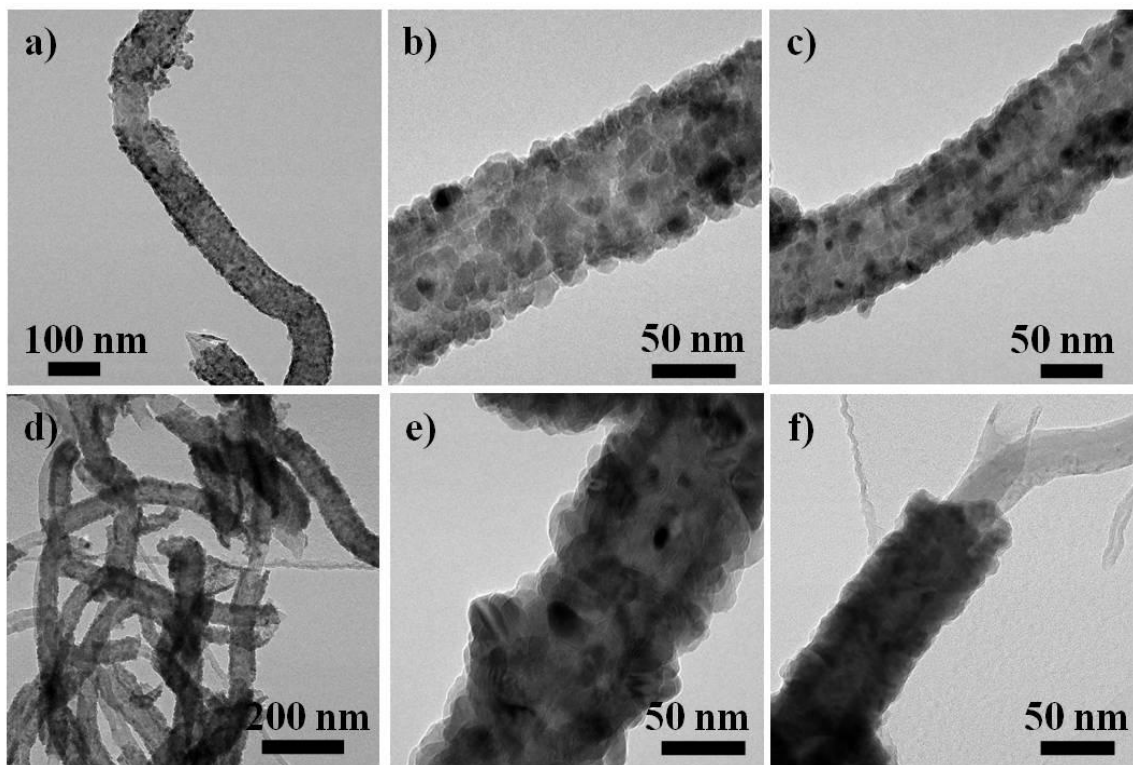


**Figure 3.3:** TEM images of MWCNTs coated with (a) 25, (b) 40, (c) 50, (d) 80, (e) 100, and (f) 150 cycles of ZnO by atomic layer deposition. Nucleation is occurring after 25 cycles and the film begins to coalesce as the number of ALD cycles increases. The film surface is rough and even with 150 cycles some portions of the nanotubes remained uncoated.

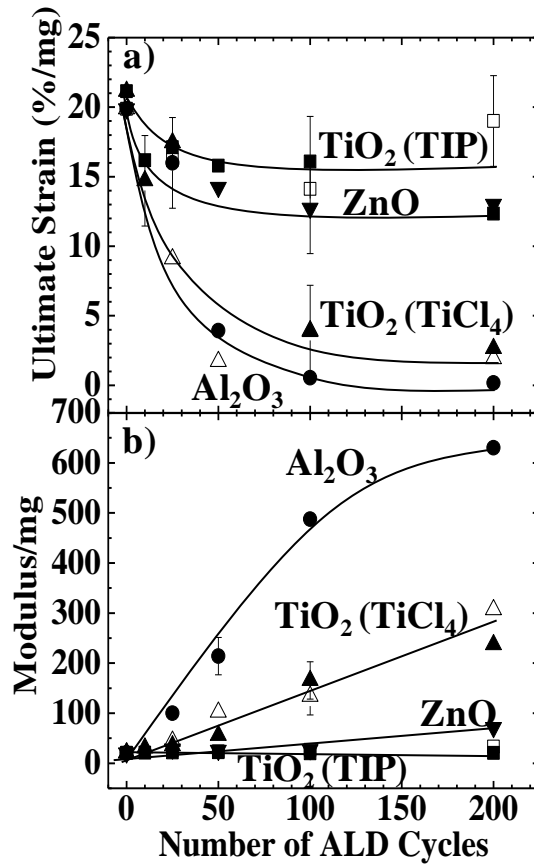


**Figure 3.4:** The (a) ultimate strain and (b) Young's Modulus versus cycle number for nylon nanofibers coated with TiCl<sub>4</sub>/H<sub>2</sub>O and TIP/H<sub>2</sub>O ALD at 105°C (solid symbols) and 50°C (open symbols), as well as results from nylon coated with ALD Al<sub>2</sub>O<sub>3</sub> and ZnO at 105°C. As the number of ALD cycles increases, the ultimate strain decreases and Young's Modulus increases for the aluminum oxide and TiCl<sub>4</sub>/H<sub>2</sub>O coated samples, consistent with increased brittleness. The TIP/H<sub>2</sub>O and zinc oxide samples show trends similar to the uncoated nylon nanofibers.

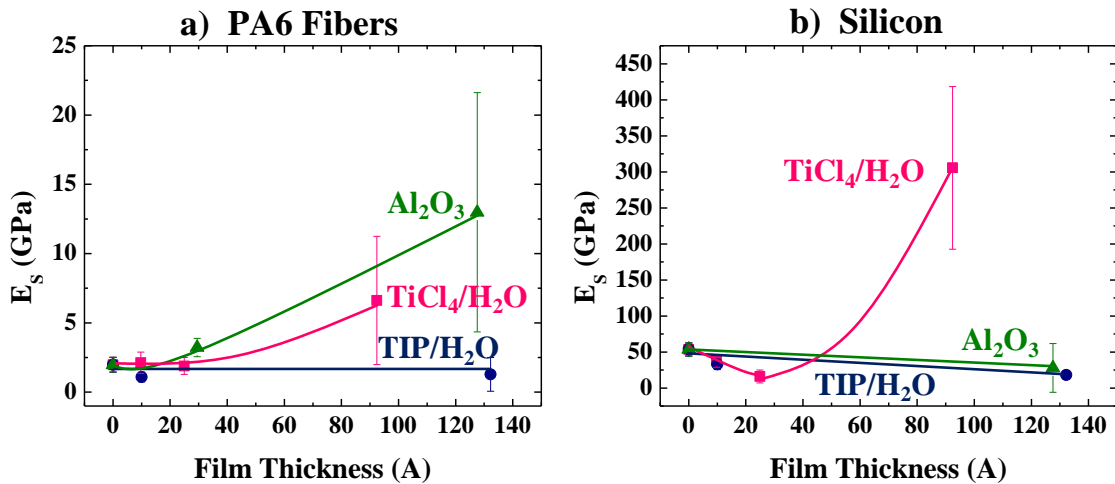


**Figure 3.5:** Modulus measured by AFM nanoindentation on (a) nylon 6 nanofibers and (b) silicon substrate. The modulus increases after the deposition of 100 ALD cycles of aluminum oxide and titanium dioxide using  $TiCl_4/H_2O$ . The modulus was unchanged after 400 cycles of  $TIP/H_2O$ , as anticipated according to previous results.

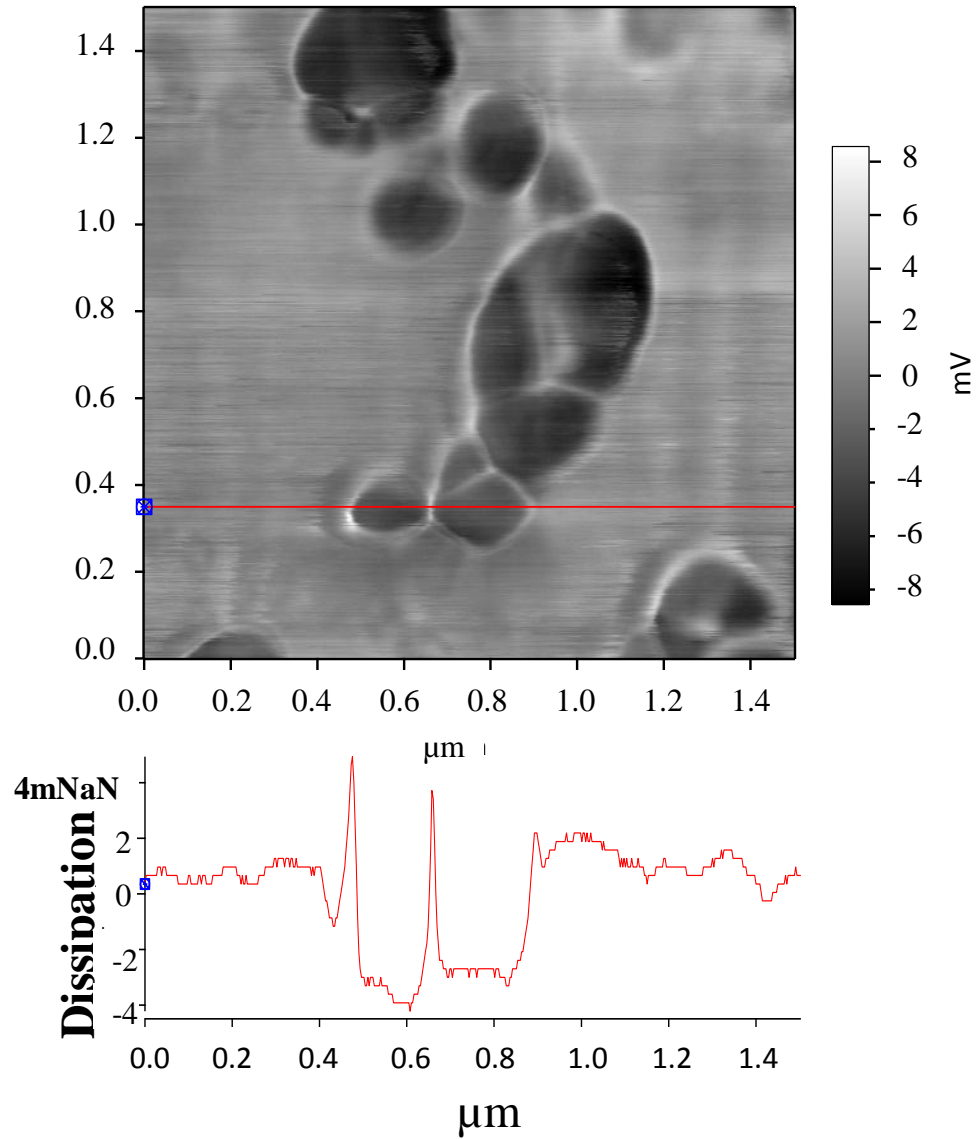


**Figure 3.6:** AM/FM AFM image of the cross-section of a nylon 6 nanofiber mat coated with 100 cycles of  $\text{TiCl}_4/\text{H}_2\text{O}$  ALD. This technique is sensitive to the stiffness of the underlying substrate as indicated by the change in dissipation as the cantilever interacts with the nanofibers compared to the stiffer surrounding epoxy.

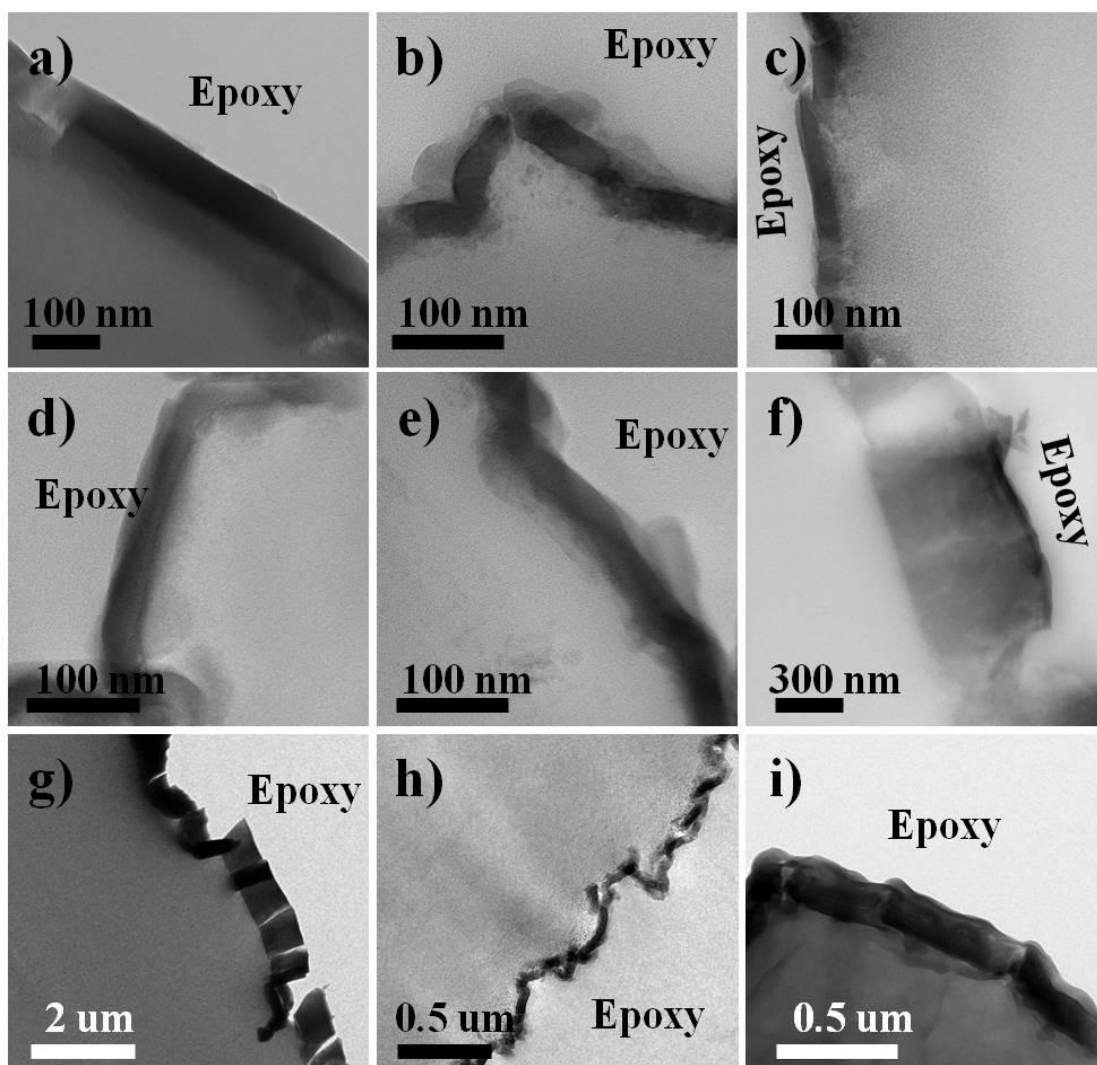


**Figure 3.7:** Cross-sectional TEM images of aluminum oxide coated nylon (a, d, g), polypropylene (b, e, h), and P55D (c, f, i). Samples (a)-(c) were coated at 50°C with 200 ALD cycles whereas samples (d)-(f) were coated at 100°C. The ALD-Hold recipe with longer precursor exposures were used for panels (g)-(I) which were coated with 200 ALD-Hold cycles at 50°C.

**Table 3.1:** Film thicknesses measured on polymer samples after 200 cycles of either ALD or ALD-Holds as measured by TEM and the film thicknesses on the silicon wafer monitor measured by ellipsometry.

<b>ALD</b>				
<b>Polymer</b>	<b>Temperature (°C)</b>	<b>Film Thickness (nm)</b>	<b>Subsurface Thickness (nm)</b>	<b>Thickness on Si (nm)</b>
PA6	50	66 ± 4	66 ± 9	35.2 ± 0.4
PA6	100	33 ± 3	25 ± 10	29.5 ± 0.2
PP	50	27 ± 4	14 ± 6	34.9 ± 0.4
PP	100	29 ± 6	18 ± 6	28.5 ± 0.1
P55D	50	30 ± 5	252 ± 20	32.4 ± 0.4
P55D	100	37 ± 4	610 ± 80	29.3 ± 0.2
<b>ALD-Holds</b>				
<b>Polymer</b>	<b>Temperature (°C)</b>	<b>Film Thickness (nm)</b>	<b>Subsurface Thickness (nm)</b>	<b>Thickness on Si (nm)</b>
PA6	50	760 ± 50	-	43.7 ± 0.6
PP	50	45 ± 4	-	45.3 ± 0.3
P55D	50	170 ± 21	-	45 ± 1

CHAPTER 4 is a reprint from a manuscript published in Langmuir 2011, Devine, C.K., Oldham, C.J., Jur, J.S., Gong, B., Parsons, G.N.

**CHAPTER 4. Fiber Encapsulation for Improved Laboratory Handling and Uniform Nanocoating of Milligram Quantities of Carbon Nanotubes by Atomic Layer Deposition**

Christina K. Devine<sup>1</sup>, Christopher J. Oldham<sup>1</sup>, Jesse S. Jur<sup>2</sup>, Bo Gong<sup>1</sup>, and Gregory N. Parsons<sup>1\*</sup>

<sup>1</sup>Department of Chemical and Biomolecular Engineering, NC State University, Raleigh, NC

<sup>2</sup>Department of Textile Engineering, Chemistry, and Science, NC State University, Raleigh, NC

Corresponding Author:

Telephone: 919-515-7553, Fax: 919-515-3465, Email: gnp@ncsu.edu

## **Abstract**

The presence of nanostructured materials in the work place is bringing attention to the importance of safe practices for nanomaterial handling. We explored novel fiber containment methods to improve the handling of carbon nanotube (CNT) powders in the laboratory, while simultaneously allowing highly uniform and controlled atomic layer deposition (ALD) coatings on the nanotubes, down to less than 4 nm on some CNT materials. Moreover, the procedure yields uniform coatings on milligram quantities of nanotubes using a conventional viscous flow reactor system, circumventing the need for specialized fluidized bed or rotary ALD reactors for lab-scale studies. We explored both fiber bundles and fiber baskets as possible containment methods and conclude that the baskets are more suitable for coating studies. An extended precursor and reactant dose and soak periods allowed the gases to diffuse through the fiber containment, and the ALD coating thickness scaled linearly with the number of ALD cycles. The extended dose period produced thicker coatings compared with typical doses onto CNT controls not encased in the fibers, suggesting some effects due to the extended reactant dose. Film growth was compared on a range of single wall NTs, double wall NTs, and acid functionalized multiwall NTs and we found that ultrathin coatings were most readily controlled on the multi-walled NTs.

## 4.1 Introduction

In the past several years, research in carbon nanotubes (CNTs) has expanded to applications such as drug delivery, transparent conductive coatings, chemical sensors, electrodes for use in organic light-emitting diodes or lithium ion batteries, as capacitors, field effect transistors, actuators, and for use in filtration applications<sup>1-4</sup>. The incorporation of nanotubes into such devices will necessitate processing and handling of relatively large quantities of nanotubes, most likely in powder form. These nanotube powders are difficult to handle and can readily spread through the laboratory and workplace. Reports of potential hazards associated with nanotube inhalation are raising concerns,<sup>5-11</sup> and safe handling practices must be considered. Safe handling is particularly important when nanotubes or other nano-powder samples are transported, for example, between preparation and surface modification work-zones.

For most applications, well dispersed nanotubes are desired, but their tendency to agglomerate in solution makes them difficult to handle. To create solution dispersions of nanotubes, surfactants such as sodium dodecyl sulfate (SDS) are often used. Surfactants do not covalently bond with the nanotubes, maintaining the  $\pi$  bonding system while allowing the nanotubes to disperse in solution. Alternative protocols for the attachment polymers and other functional groups can alter the  $\pi$  conjugation system and affect the properties of the nanotubes<sup>12-14</sup>.

Another method to change the surface energy of carbon nanotubes is to use vapor-phase processes to deposit a thin film coating. Atomic layer deposition (ALD) is used

because it produces highly conformal coatings and is compatible with mild process conditions suitable for nanotubes. Atomic layer deposition uses a sequence of self-limiting reactions to achieve monolayer control over film thickness. The deposition of thin films alters the surface properties of the material, which can increase hydrophilicity and thus improve dispersion of carbon nanotubes in aqueous solution.

Interest in nanomaterials with modified surface composition is leading to new direct methods to uniformly coat volumes of nanotubes and other small objects (e.g. particles, powders, etc.) using vapor phase processes. Our interest, for example, is to explore ultrathin coatings on carbon nanotubes, where at its ultimate thin limit, the nanoscale coating may not significantly affect the performance of the nanotube for its particular application, but it may be able to diminish or eliminate any possible ill effects of exposure. Because nanotube powders are volatile in flowing gas, caution is required to keep nanotubes from dispersing and spreading throughout the reactor during coating. Most studies of ALD coatings on CNTs are performed using nanotubes that are anchored to a Si substrate, or nanotubes deposited on a TEM grid<sup>15,16</sup>. Farmer et al. suspended SWNTs by growing them between two electrodes which helped stabilize them in the reactor and allow direct electrical testing<sup>17</sup>. To coat gram quantities of nanotube powders and decrease CNT agglomeration, custom rotary or fluidized bed tool designs have emerged<sup>18-20</sup>, but issues related to hazard mitigation during powder loading and unloading are not often discussed.

While researcher safety is always a primary concern, few reports directly discuss practices for safe handling of nano-powders as part of the process design. New procedures

describing how to safely handle and contain nanomaterials during vapor phase processing will benefit many research groups in this field. For ALD coating in particular, new procedures and methods will be most attractive if they do not require special deposition equipment designs, but instead are compatible with common commercial or self-fabricated viscous flow ALD reactors. Ideally, any containment method must not interfere substantially with the coating process. The challenge, therefore, is to identify containment methods that secure the nanotubes during transfer in lab air and during vapor phase processing in a viscous flow reactor, while not impeding or otherwise interfering with the ALD reaction sequence.

For this study, two methods were explored to secure and hold carbon nanotubes during laboratory handling and ALD  $\text{Al}_2\text{O}_3$  coating. The reactor used here is a simple self-fabricated viscous flow tubular reactor, and it includes many of the design elements of commercial laboratory-scale tools. One approach we explored used bundles of cotton fibers to absorb nanotubes that were previously dispersed in solvent. A second method used a fiber “basket” (or “wrapping”) to hold the nanotubes, where the nanotubes are loaded as dry powders into a supported fibrous capsule. The fiber “bundle” and “basket” methods both permit the reactant gases to flow through and around the nanotubes, while preventing the tubes from spreading in the reactor during ALD processing. The fiber basket or bundle can hold milligram quantities of nanotubes and improve the handling and transfer of the nanomaterials from a closed glove-box, through the lab and into the ALD reactor without undesired dissemination. The fiber basket method in particular, did not significantly affect the coating process, and we were able to repeatedly and reliably form uniform coatings as thin as 4 nm. We find significant differences in the ALD film coatings and product yields

obtained by the bundle and basket methods. Specifically, we show here that the fiber wrapping method has distinct advantages over the fiber bundle approach in terms of handling, yield of coated nanotubes, and quality of the coating process. Using these methods the CNTs were not agitated to prevent aggregation, as would be the case in using fluidized bed or rotary reactors.<sup>18</sup> The effectiveness of our fiber containment methods at preventing CNT aggregation was not directly evaluated.

## **4.2 Experimental Methods**

### **4.2.1 Multiwall Carbon Nanotube Preparation and Containment for ALD Coating**

The nanotubes used for the fiber containment studies were multiwall nanotubes purchased from Helix Material Solutions. Two different approaches were explored for supporting and containing the nanotubes for deposition: i) fiber bundle; and ii) fiber basket (or fiber wrapping) carrier structures. For the “fiber bundle” approach, carbon nanotubes were suspended in a 0.5 wt % CNTs methanol solution and sonicated for ~15 minutes until uniformly dispersed by visual inspection. Using a syringe, about 6 ml of the suspension was dripped onto ~250 mg sized quartz wool bundles (Leco Corporation) or cosmetic grade cotton fiber balls. Upon loading the fiber bundles with nanotubes, the bundles visibly changed from bright white to black in the regions wetted by solution, as shown in Figure 4.1. After loading, the fiber bundles were allowed to dry at room temperature for more than 24 hours before being transferred into the ALD reactor.

For the “fiber basket” method, a screen made of metal wires with ~ 0.7 mm diameter in a 1.5 mm square grid pattern was formed into a cylindrical scaffold approximately 3 cm

long and 2 cm in diameter then wrapped with either a nonwoven polypropylene (PP) fiber mat or a woven cotton fiber cloth. The nonwoven PP fiber materials were obtained from NC State College of Textiles and the cotton was obtained from Textile Innovators. They were used as received.<sup>21-25</sup> Images of baskets fabricated and the materials required for this study are shown in Figure 4.1. The fiber sheet secures the nanotubes in the basket, and we will show below that the precursor and reactant gases can readily diffuse through the fibers to reach the nanotube samples. Each basket was loaded with approximately 30-50 mg of nanotubes before being enclosed using polyimide film tape. The basket was capable of holding roughly 200 mg of material, however they were not fully loaded, which may allow some nanotube movement inside the basket during processing. To avoid user exposure to nanotubes, all carbon nanotube handling, storage, and transfer to the fiber carriers was performed in a bench-top nitrogen-purged glove box (LC Technology Solutions).

#### **4.2.2 Preparation of Nanotube Control Samples**

In addition to the encased CNTs, some control samples were prepared directly onto TEM grids. The control samples used the MWNTs mentioned previously as well as single-walled and double-walled nanotubes (SWNTs and DWNTs respectively) purchased from Helix Material Solutions. Additionally, MWNTs refluxed in  $\text{H}_2\text{SO}_4/\text{HNO}_3$  to form carboxyl and hydroxyl functional groups were purchased from NanoLab Inc. (Waltham, MA). All carbon nanotube materials were used as received. To prepare the controls, approximately 10 mg of nanotubes were suspended in 20 ml of methanol and sonicated for 15 minutes. A small amount of the sonicated solution was transferred by pipette onto a holey carbon TEM

grid, and the methanol was evaporated in air before loading the grid into the reactor. The grids were anchored in the reactor using an alligator clip secured to the sample boat.

#### 4.2.3 Porosity of the Fiber Mats

The porosity of the fiber mats was estimated using the material density and a known sample size and weight. Specifically, the polypropylene mat is ~0.3 mm thick and weighs  $4.4 \pm 0.3 \text{ mg/cm}^2$ , giving an effective mat density of  $150 \pm 10 \text{ mg/cm}^3$ . Using the tabulated density of polypropylene ( $900 \text{ mg/cm}^3$ ), the net porosity of the fibers is  $0.17 \pm 0.01 \text{ cm}^3/\text{cm}^3$ . This means that the 0.3 mm thick fiber mat contains ~ 83% polymer and ~ 17% void or air space. The thickness and density of the cotton is more difficult to analyze. The mat thickness is approximately 0.5 mm with a mass of  $28 \pm 1 \text{ mg/cm}^2$  giving a density of  $560 \pm 20 \text{ mg/cm}^3$ . Assuming the density of cotton is  $1500 \text{ mg/cm}^3$ , the porosity of the fiber mat is estimated to be  $0.37 \pm 0.01 \text{ cm}^3/\text{cm}^3$ . Furthermore, we measured the PP and cotton sample surface area using Brauner Emmett and Teller (BET) adsorption analysis. This allows us to obtain an effective surface area enhancement to the fiber mats (i.e. net surface area per unit projected surface area). For example, the BET surface area for the polypropylene is ~1.6  $\text{m}^2/\text{g}$  (or  $16 \text{ cm}^2/\text{mg}$ ). A sample of polypropylene fiber mat cut into a  $1 \text{ cm}^2$  sample size weighs 4.4 mg, so therefore, there is ~70  $\text{cm}^2$  of surface area for each  $\text{cm}^2$  of fiber mat. One typically defines the aspect ratio of a non-planar surface structure as the feature depth per unit width. The surface area enhancement ratio (i.e. ~70:1 in this case) provides a rough estimate of the effective aspect ratio. However, since the transport paths through the fibers are nonlinear, we also must consider the system tortuosity, defined in porous media as the ratio between the non-linear distance a species must travel across the matrix and the linear

matrix thickness. In these fiber systems, the open fiber matrix provides many viable pathways for species transport, so we estimate the effective tortuosity to be less than or equal to ~2-3. The overall effective aspect ratio will then be the product of surface area enhancement and the tortuosity. Considering the values for surface area enhancement and tortuosity, the overall effective aspect ratio for the fiber mats is ~ 200:1. Even more conservative estimates of aspect ratio and tortuosity would still produce effective aspect ratios less than 1000:1. It is well known that ALD processes are readily capable of conformal nanocoatings on features with aspect ratio > 1000:1.<sup>26,27</sup> Therefore, we reasonably expect that the ALD precursors will readily diffuse through the fiber mat to reach the enclosed carbon nanotubes.

#### **4.2.4 ALD Film Coating**

After filling and securing the fiber bundle or basket holders with CNTs in the glove box, the samples were transported by hand in air using protective laboratory gloves from the glovebox to the ALD reactor chamber. The nanotube-loaded fiber bundles or baskets were placed onto a large sample boat and transferred into the heated zone of a hot wall viscous flow ALD reactor.

Two controls were used during film deposition. As one control, carbon nanotubes on TEM grids were coated under similar conditions, but with a different recipe, to compare growth on the fiber contained samples. As a second control, small silicon wafer pieces (~1 × 2 cm<sup>2</sup>) were also coated during the ALD runs. For each run, one or more silicon wafer pieces were placed in the reactor and not otherwise encased. For the fiber basket studies, two other

silicon pieces were coated with the CNTs during each run. One smaller ( $\sim 0.5 \times 1 \text{ cm}^2$ ) silicon wafer piece was typically placed in the fiber basket with the nanotubes, and one  $\sim 1 \times 2 \text{ cm}^2$  wafer piece was wrapped in PP or cotton in another fiber basket separate from the CNT basket.

The reactants for deposition were trimethylaluminum (TMA) and water. The ALD runs were performed at  $90 \text{ }^\circ\text{C}$  and  $\sim 2.0 \text{ Torr}$ , and between  $\sim 10$  and  $200$  ALD cycles were used for coating. To help ensure the precursor gases diffused throughout the CNT fiber samples, we used extended precursor soaks during the ALD runs. The soak steps consisted of flowing TMA for 5 seconds, then the gas inlet and outlet valves were closed to produce a static gas exposure in the reactor for 60 seconds. During the soaking period, the pressure increased from  $\sim 2.0$  to  $\sim 2.2 \text{ Torr}$ . Following the soak, the chamber was purged for 90 s using purified nitrogen gas and the pressure returned to  $\sim 2.0 \text{ Torr}$ . The water exposure also followed the same flow and soak-time sequence, followed by another  $\text{N}_2$  purge for 120 s. This flow/soak sequence is designated as  $\text{TMA/Ar/H}_2\text{O/Ar} = 5(60)/90/5(60)/120$  seconds. For CNT samples on the TEM grids, the ALD sequence used a 1 s TMA dose followed by a 30 s  $\text{N}_2$  purge. The water dose was also 1 s and the following purge was 60 s.

#### **4.2.5 Characterization of Coated CNTs**

After coating, the carbon nanotubes were collected and analyzed. The fiber bundles and fiber baskets were handled differently. The bundle samples were rinsed with flowing methanol into 20 ml scintillation vials, and the methanol was allowed to evaporate at room temperature. The dry powder appeared light gray, likely because of remnant material from

the quartz or cotton fibers. Generally, the quartz wool resulted in more remnant material than the cotton fiber bundles, but the quartz allowed the nanotubes to be more easily rinsed out. Figure 4.1 shows photographs of the quartz wool and cotton fibers after loading with CNT's, and after coating and rinsing to remove the coated nanotubes. We attempted to evaluate the effective yield of the fiber bundle containment method by weighing the fiber bundles before and after the nanotube loading, ALD coating, and CNT removal steps. However, the weight changes were too small and the variability was too large to obtain reliable results. For example, in some cases, nanotubes fell out of the fiber bundles during sample transfer and ALD treatment.

We had more success with the fiber basket method. After ALD coating, the fiber baskets were returned to the glovebox and the coated nanotubes were emptied into a scintillation vial. We found that the ALD coating produced a large increase in the mass of the CNTs, consistent with conformal film coating. We worked to estimate the yield of coated CNTs using this method (i.e. the fraction of CNTs lost or remaining in the basket after processing), but the large mass change made this difficult. Therefore, as another control experiment, the CNTs were weighed then filled into the fiber baskets as normal before transfer into the ALD reactor. The samples were exposed to reaction process conditions (i.e. N<sub>2</sub> purge at 2 Torr for approximately 1, 5, or 10 hours), without any TMA or water exposure. The weight of the CNTs removed from basket after this process was within ~2% (weighing accuracy) of that measured before loading, demonstrating negligible loss of CNTs using the fiber basket method.

Small samples of the CNTs coated using the fiber bundle and fiber basket methods, as well as those coated directly on the control TEM grids were analyzed using an FEI Tecnai G<sup>2</sup> Twin transmission electron microscope. The thickness of the nanotubes was estimated from the TEM images using ImageJ software. Additional TEM analysis was performed using a Hitachi HF2000 equipped with an Oxford Link INCA energy dispersive spectroscopy (EDS) system. It is important to note that many individual tubes were imaged during TEM analysis, and the results were highly self-consistent within a deposition run. Selected representative images are shown in the figures.

Raman spectra were collected for the MWNTs using a Horiba-Jobin Yvon LabRAM HR VIS confocal microscope with a 632 nm laser source. The spectrometer was calibrated using the crystalline silicon peak at 520.7 cm<sup>-1</sup>

## **4.3 Results**

### **4.3.1 Fiber Bundle Method**

Figure 4.2 displays TEM images collected from ALD coated multiwall CNTs after 25 and 80 cycles, where the CNTs were supported in the reactor using cotton fiber bundles. The images show the multiwall nanotubes enclosed by a uniform and conformal coating, with a thickness of ~ 5 nm after 25 cycles. The samples coated with 80 cycles also show coatings of ~ 5 nm, suggesting problems with coating nucleation on the nanotubes and/or problems with the fiber support method. Many CNTs were observed to be entrained in the fiber bundle after coating and rinsing, especially for samples coated with more than ~ 25 ALD cycles. The coating likely helped adhere the CNTs to the fibers making them more difficult to

remove. After ALD coating and rinsing with solvent, we attempted to retrieve more CNTs from the fiber bundles by calcining them at 450°C in air for 48 hours. However, an organic residue remained after calcination, impeding CNT recovery. After several attempts to modify the process details to improve the outcome, we abandoned this approach in favor of the basket method.

### **4.3.2 Fiber Basket Method**

Figure 4.3 presents TEM images of multiwall CNTs after 25, 50, 100 and 200 ALD cycles, where the nanotubes were wrapped in the PP basket during coating. Many images were collected for each coating condition, and the tubes within a sample set showed very consistent results. From the images, all samples show smooth and conformal film coatings. The film thickness increased linearly with cycle number on all analyzed surfaces as demonstrated in Figure 4.4. The film thickness for the MWNTs was estimated from TEM images, and thickness on Si was determined by ellipsometry. Several different silicon samples were measured, including silicon placed in the polypropylene basket, silicon wrapped directly in PP, and silicon with no fiber wrapping. We see that each of these samples resulted in films with very similar coating thicknesses, confirming that under the conditions used, the fiber wrapping does not strongly affect the film growth. The dashed line in Figure 4.4 shows the deposition rate is  $\sim 2 \text{ \AA/cycle}$  on the CNTs and on the silicon. This rate is somewhat larger than  $\sim 1.1 \text{ \AA/cycle}$  typically observed for ALD  $\text{Al}_2\text{O}_3$  at 90°C. This higher growth rate could result from the long dose times during the “soak” sequence, or from excess precursor or water remaining in the fiber mesh after the purge sequence.

In addition to baskets wrapped in polypropylene, we evaluated common woven cotton fabric as a basket containment material. The TEM images of MWCNT's after 25, 50, 100, and 200 ALD cycles (including the soak steps) using the cotton wrapping are shown in Figure 4.5. Similar to the films coated in the PP fiber baskets, the films appear to be smooth and conformal from 25 cycles up to 200 cycles. After 100-200 cycles of ALD coating, many nanotubes appeared in the TEM images with uncoated ends, as depicted in Figure 4.5d, consistent with breakage after coating (probably during sample transfer and handling for TEM). We observed breakage only with the thicker coatings, consistent with increases in brittleness with film coating thickness.

We also collected TEM images after 10 and 15 cycles using the cotton basket, and results are presented in Figure 4.6. The coatings showed a coarser texture compared to the thicker coatings, consistent with three-dimensional film nucleation. There is not much difference in film thickness and nuclei texture after 10 and 15 cycles. For both samples the nuclei and film thickness varies between ~0 and ~9 nm. The 25 cycle coating (Figure 4.5) produced a continuous coating, but the film thickness varied considerably between ~4 and ~14 nm. Thicker films (between 50 and 200 cycles) produced more uniform and consistent film coverage on these MWCNTs. Figure 4.7 shows the measured coating thickness on the multiwall nanotubes versus ALD cycle number when the tubes are encased in cotton fiber baskets during growth. For control experiments, we deposited simultaneously onto silicon wafer pieces exposed directly to the growth vapors, as well as silicon wafer pieces wrapped into fiber baskets. Results from these samples are also presented in Figure 4.7. The trend in the graph is nearly identical to the results shown in Figure 4.4 for nanotubes and silicon

encased in polypropylene, with a growth rate of  $\sim 2 \text{ \AA}/\text{cycle}$  on the CNTs and on the silicon control wafers. To determine whether the elevated growth rate was the result of water present in the cotton fibers, the baskets were loaded with CNTs and heated to  $150^\circ\text{C}$  in the reactor for one hour before ALD at  $90^\circ\text{C}$ . These samples showed the same growth rate, suggesting residual the excess growth was not due to water trapped in the fiber mesh before deposition.

We also explored a conventional ALD process sequence, without the long soak period, to assess process requirements for CNT coating in the cotton basket method. Results from TEM analysis of MWCNTs coated without the soaking step are shown in Figure 4.8. Coating MWNTs in the cotton wrapped basket using 50  $\text{Al}_2\text{O}_3$  ALD cycles using a 1s TMA dose, a 30s purge, a 1s  $\text{H}_2\text{O}$  dose and a 30 s purge resulted in a  $\sim 3 \pm 1 \text{ nm}$  coating that was not conformal or continuous. This result shows that a soak step is important when using the cotton baskets, and based on the data in Figures 4.3-4.7 the 60 second soak time appears to be sufficient. A more detailed study of the effect of soak time on film growth uniformity and thickness would help improve and optimize the process. Finally, the results for the fiber basket method further suggest that a larger quantity of nanotubes could be coated using a larger basket and a larger ALD reactor. The recipe would also likely have to be scaled to account for the larger surface area to be coated.

Raman spectra were collected for bare MWNTs as well as those coated with 25, 50, and 100 cycles of  $\text{Al}_2\text{O}_3$ , as shown in Figure 4.9. The spectra are typical of MWNTs, including the D, G, D', G' peaks near  $1320$ ,  $1570$ ,  $1600$  and  $2640 \text{ cm}^{-1}$ , respectively.<sup>28-30</sup> The

spectra in the figure are normalized to the D peak. The G peak corresponds to the graphitic carbon signal, and the relative size of the other peaks is often related to disorder and defects, which are substantial in these MWNT materials. Upon ALD coating, changes and trends are detected in the Raman signal, but generally, the primary signatures of the CNT's are still present, demonstrating that the CNT structure is maintained upon ALD coating. The changes in the spectral peaks may result from some change in the nanotubes upon coating. However, it is also reasonable to expect that a thin conformal coating on the CNT's could affect the nanotube vibrational signature, even in the absence of change in the CNT itself. Furthermore, although not discussed here in detail, we coated MWNTs with ALD ZnO and tested their Raman signature. The results with ZnO ALD were very similar to that with the Al<sub>2</sub>O<sub>3</sub> ALD. The spectra showed some changes, but the primary Raman signature was not significantly altered.

#### **4.3.3 ALD on MWNTs on TEM Grids**

Several MWNTs loaded on TEM grids for ALD coating, and directly transferred to the TEM for imaging. The process sequence used 1s/30s/1s/60s TMA/N<sub>2</sub>/water/N<sub>2</sub> exposures without precursor soak steps. Figure 4.10 shows typical images for the MWCNTs coated on the TEM grid. During the first 5-10 cycles, nodular nuclei appeared on the CNT surface. Fifteen cycles produced rough but cohesive films. The coatings are smooth and uniform after 100 and 200 ALD cycles. The film thickness increased approximately linearly with number of cycles, with a rate of ~1.1 Å cycle. This is similar to that expected for typical ALD under the conditions used, but it is less than the thickness observed after the soaking

exposure sequence in the fiber baskets. This result may indicate some trapping of precursor and/or reactant species in the fiber baskets during the film coating process.

#### **4.3.4 ALD on Other Types of CNTs**

In addition to MWCNTs, we also explored ALD onto commercial single-walled nanotubes. The nanotubes were coated on TEM grids at 90°C, and Figure 4.11 shows the resulting images collected from a few isolated SWCNTs after ALD coating. The deposition sequence was the same as that for the MWCNTs shown in Figure 4.10. As received, the nanotubes formed rope-like agglomerations or bundles visible in the TEM micrographs. The bundles remained after coating, making the film thickness and surface texture difficult to evaluate. The coated rope-like agglomerations of SWNTs showed relatively uniform and smooth coatings, however, the individual SWNTs showed nodular growth similar to that reported by Zhan et al.<sup>31</sup> After 100 ALD cycles the film thickness was approximately  $8 \pm 2$  nm. This is slightly smaller than that measured on the MWNTs. The nodules persisted after 200 ALD cycles. However they appeared to be growing into one another to form a cohesive film. After 200 ALD cycles the film thickness was approximately  $20 \pm 3$  nm. The 200 cycle coatings appear to have cracked and slid from the nanotubes, as shown in Figure 4.11c. This cracking and sliding behavior was observed only for the thicker coatings, consistent with the thick Al<sub>2</sub>O<sub>3</sub> layer being more brittle than the nanotube substrates.

The double-walled nanotubes were also entangled in rope-like aggregates. Figure 4.12 shows TEM images of DWNTs without coating and after ALD coating on the TEM grids. The ALD coating on the double-walled nanotubes was not continuous, with nodular growth similar to that seen on the SWNT samples. The radius of the nodules in Figure 4.12b

is approximately  $10 \pm 2$  nm. The DWNTs were also aggregated into rope-like bundles in the 200 cycle grid, as shown by the nanotube to the left in Figure 4.12c. One single DWNT separated from the aggregate in panel (c) showed both nodular and cohesive (but rough textured) growth on different parts of the tube. The average thickness of the coated region was  $21 \pm 3$  nm. More uniform growth likely proceeds on tubes with a high density of defect sites. Because the bundles include multiple tubes, they will have more defects per unit length, and hence will more likely promote cohesive growth.

We next consider coatings on the functionalized nanotubes shown in the TEM images in Figure 4.13. The uncoated functionalized multiwall nanotubes appear very similar to the non-functionalized MWNTs, but smaller in diameter. The functionalization process performed by the vendor involved refluxing in  $\text{H}_2\text{SO}_4/\text{HNO}_3$  to form carboxyl and hydroxyl functional groups on the surface. Several of the nanotubes appeared to have a rough surface, which was likely a result of the functionalization process. After coating with 100 or 200 ALD cycles on the TEM grid, the coatings were continuous, conformal and smooth with thickness of approximately  $11.8 \pm 0.6$  nm and  $23 \pm 2$  nm respectfully. Again, the growth rate is nearly the same as that on silicon control wafers coated during the same runs.

#### **4.4 Discussion and Conclusions**

We find that reasonably reliable ALD coatings can be obtained on milligram quantities of carbon nanotubes in a conventional flow-through reactor by enclosing the nanotube particles into baskets constructed from nonwoven polypropylene or cotton fabric. Simple flow analysis suggests that the ALD precursors and co-reactant species can readily

transport through the fiber mesh and permeate the CNT powder sample, and TEM data regarding coating uniformity and conformality are consistent with this analysis. To provide sufficient species transport time, an exposure soak cycle is used, where the substrate is exposed to standing gas for ~ 60 seconds during each ALD half-cycle step. The soak sequence produced a growth rate of ~ 2 Å/cycle for TMA/water exposure at 90°C, which is nearly a factor of two larger than observed for conventional continuous gas flow ALD under otherwise the same process conditions, indicating that the processing conditions have yet to be optimized. Growth proceeded readily on multiwall carbon nanotubes, producing conformal films as thin as ~4 nm in this study after 35 ALD cycles.

The film growth on the nanotubes appears to be independent of whether PP or cotton was used as the wrapping material. Fiber baskets fabricated using relatively dense nonwoven polypropylene provided the same results as fiber baskets produced using less dense cotton fabric. Even though coatings exceeding ~45 nm were not evaluated in this study, we anticipate that increasing the ALD cycles beyond 200 or more may ultimately impede further film growth. At some point the ALD film deposited on the fiber mesh container will begin to hamper the diffusion of precursor and byproduct gases through the material.

Fiber basket enclosures and cotton fiber bundles were compared for safe nanotube confinement and encapsulation of milligram quantities of carbon nanotubes during sample transfer, loading and coating deposition. The fiber basket method was easier to implement than the fiber bundle method, and the baskets enabled larger quantities of nanotubes to be coated. Moreover, the basket approach produced more repeatable and uniform coatings on

the carbon nanotubes compared to those loaded in fiber bundles. The fiber basket method produced repeatable and uniform coatings on milligram quantities of nanotubes using a conventional viscous flow reactor system. This approach circumvented the need for specialized fluidized bed or rotary ALD reactors for lab-scale studies, especially where particle aggregation is not critical. After loading fiber baskets with CNTs in the glovebox, the baskets were handled and transported in air to the reactor, exposed to the coating sequence, then transferred back to the glovebox. This process produced no visible loss of nanotubes to the air or outer surface of the white fiber baskets, indicating that the baskets were reasonably safe to use in the laboratory environment.

The fiber basket method provides a relatively simple approach to coat larger number of CNT's and other micro or nanoscale objects in conventional flow-through ALD reactors. While the expressed toxicity and safety of nanomaterials were not studied here, the encapsulation method helped significantly to reduce nanotube and nanoparticle dispersion during routine laboratory handling. While we demonstrate here coatings on up to 100 mg of sample in one deposition run, scaling the process to larger basket size will require process analysis to achieve optimum conditions.

### **Acknowledgments**

The authors acknowledge support from NIH RC2 grant 1RC2ES018772-01 in collaboration with J. Bonner in the Department of Toxicology at NC State University, and support from NSF, project number CMMI-1000382.

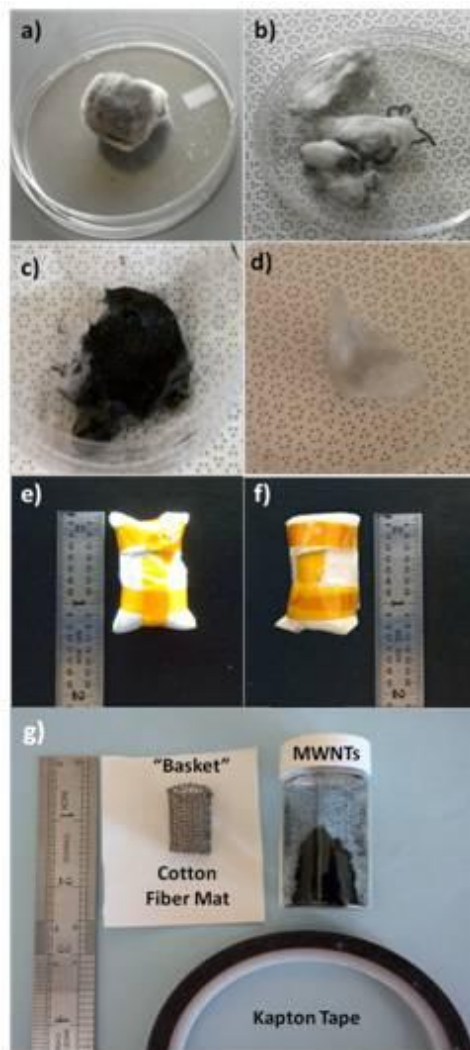


**Figure 4.1:** (a)-(d) Carbon nanotubes contained in fiber bundles. Image (a) shows a cotton ball loaded with CNTs prior to ALD processing. (b) After ALD coating the CNTs were rinsed from the cotton balls using methanol, but large amounts of CNTs remained. (c) Quartz wool fiber bundle after being loaded with CNTs and prior to ALD processing. (d) After coating and rinsing, fewer CNTs remained in the quartz wool compared to cotton. Images (e) and (f) show CNTs contained in cotton and polypropylene fiber baskets, respectively. Panel (g) shows the materials used to create the baskets.

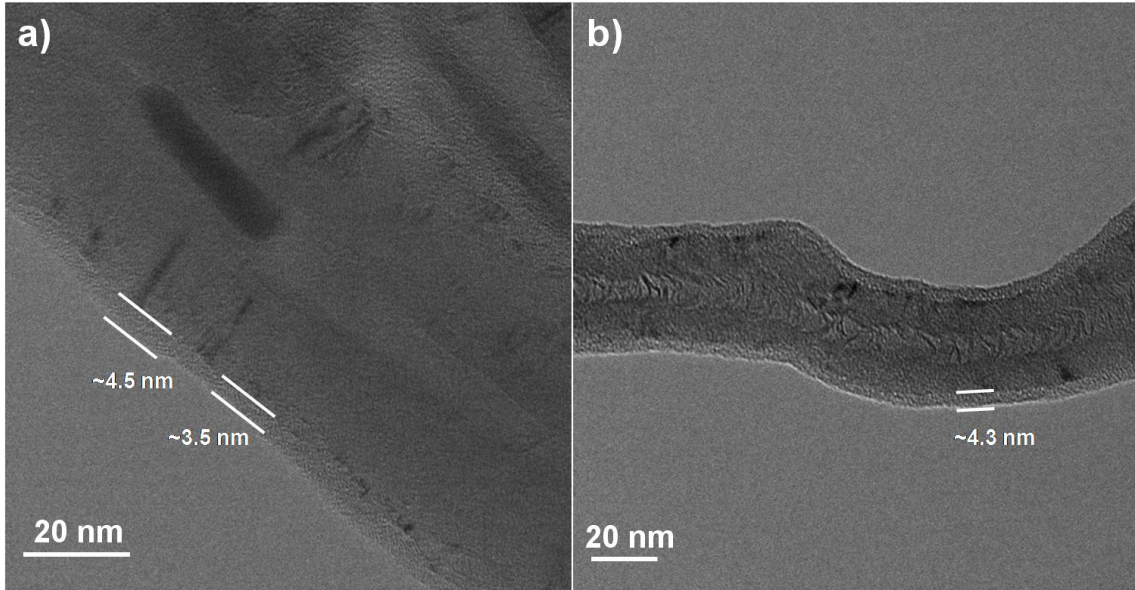


**Figure 4.2:** TEM Images of MWNTs coated with a) 25 cycles of  $\text{Al}_2\text{O}_3$  ALD and b) 80 cycles  $\text{Al}_2\text{O}_3$  ALD at  $90^\circ\text{C}$  from fiber bundle method. Image a) shows a continuous but not conformal coating with the coating thickness varying from 3.5 to 4.5 nm. Image b) has a continuous and conformal coating with a thickness of only 4.3 nm, similar to the 25 cycle coating.

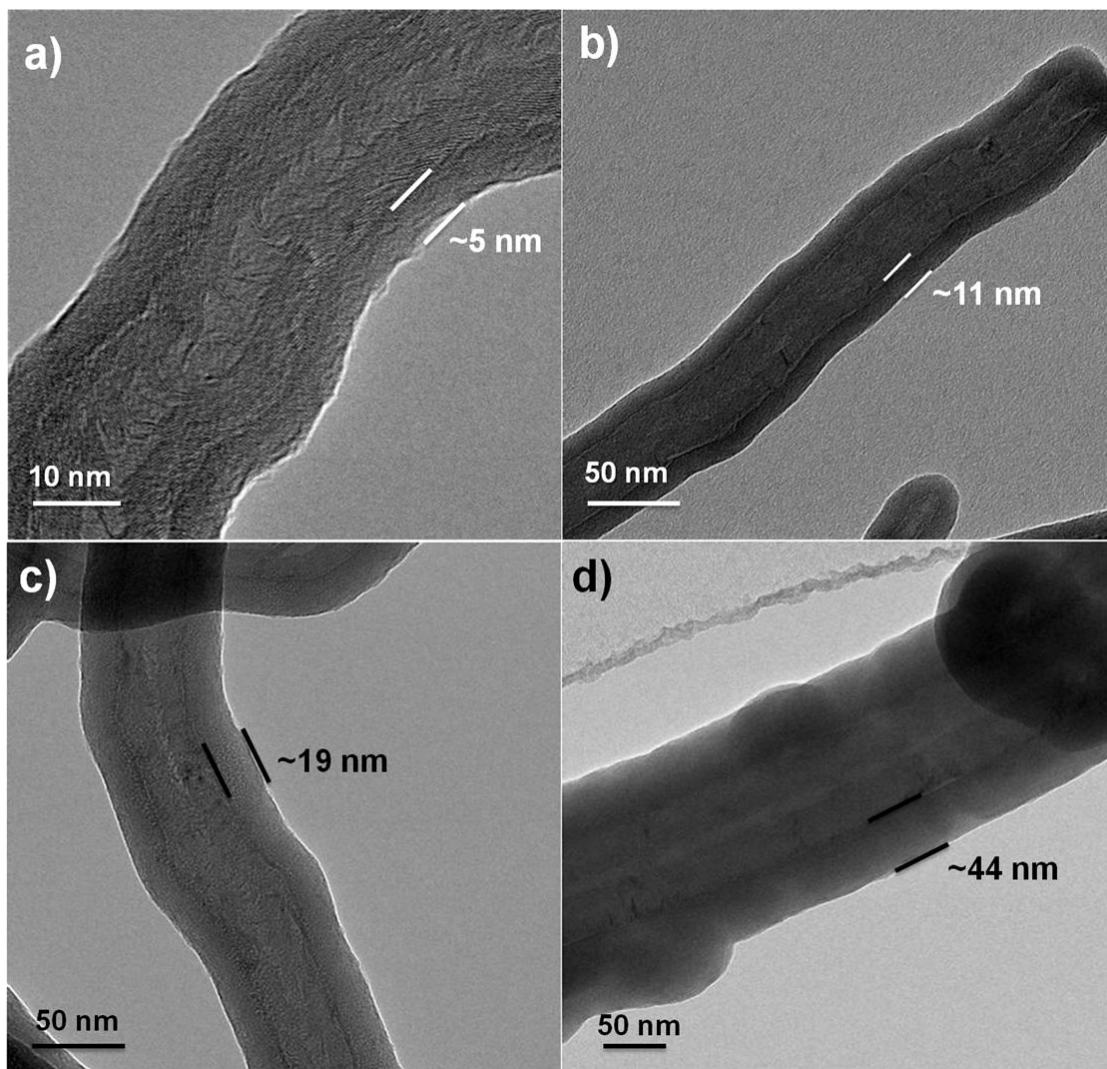


**Figure 4.3:** TEM images of MWNTs coated with a) 25; b) 50; c) 100; and d) 200 cycles of Al<sub>2</sub>O<sub>3</sub> ALD at 90°C using the polypropylene basket method. The coatings were continuous and conformal and the film thickness increase linearly with the number of ALD cycles.

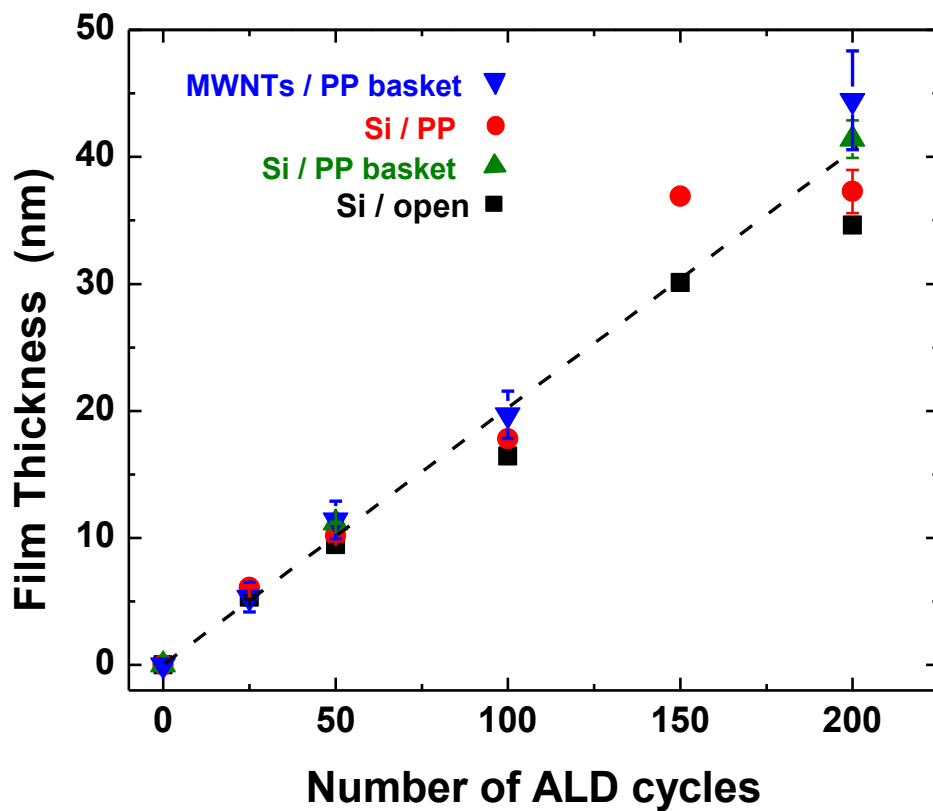


**Figure 4.4:** Graph comparing film thickness on different Si controls and MWNTs using the PP fiber mat. Thickness was measured on silicon directly wrapped in cotton (“Si / PP”), in a PP basket (“Si / PP basket”), and for no fiber containment (“Si / open”). The film thickness increases with linearly with cycle number, and the growth rate is nearly the same on all silicon samples and on the CNTs.

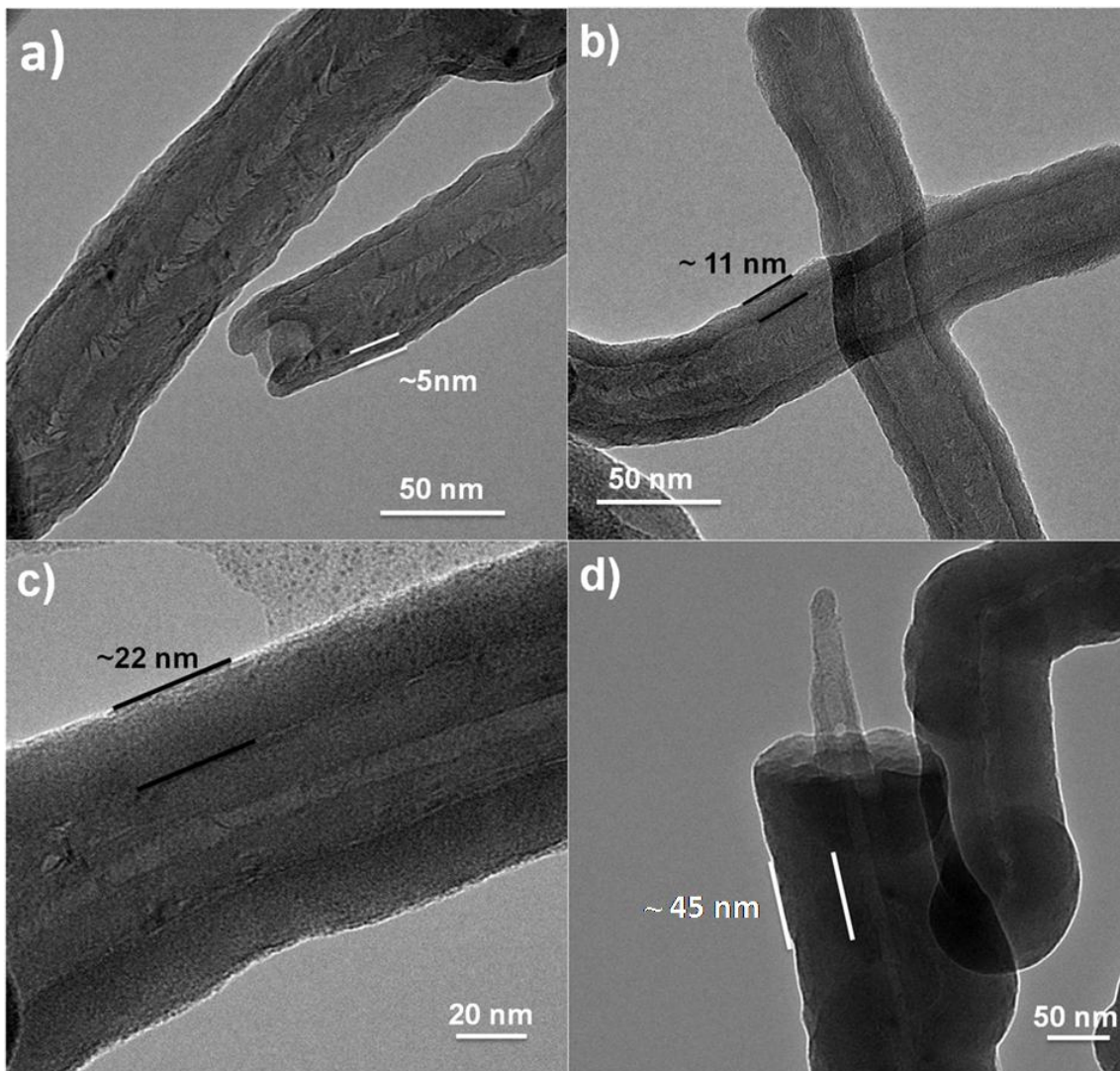


**Figure 4.5:** TEM images of MWNTs coated with a) 25; b) 50; c) 100; and d) 200 cycles Al<sub>2</sub>O<sub>3</sub> ALD at 90°C using the cotton wrapped basket method. The coating thickness increased linearly with cycle number. Several uncoated or broken ends were observed as shown in panel (d). In other images (not shown), the number of visible broken ends increases as the coating thickness increases.

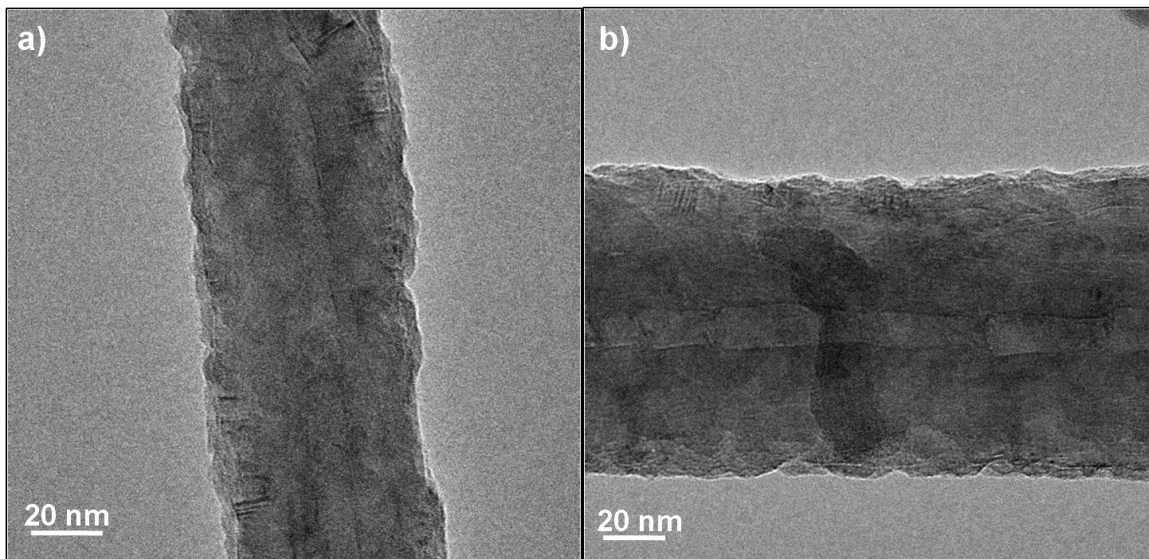


**Figure 4.6:** TEM images of MWNTs coated with a) 10 and b) 15 cycles  $\text{Al}_2\text{O}_3$  ALD at  $90^\circ\text{C}$  using the cotton wrapped basket method. Growth of nuclei had begun by 10 cycles and these nuclei were beginning to grow together at 15 cycles.

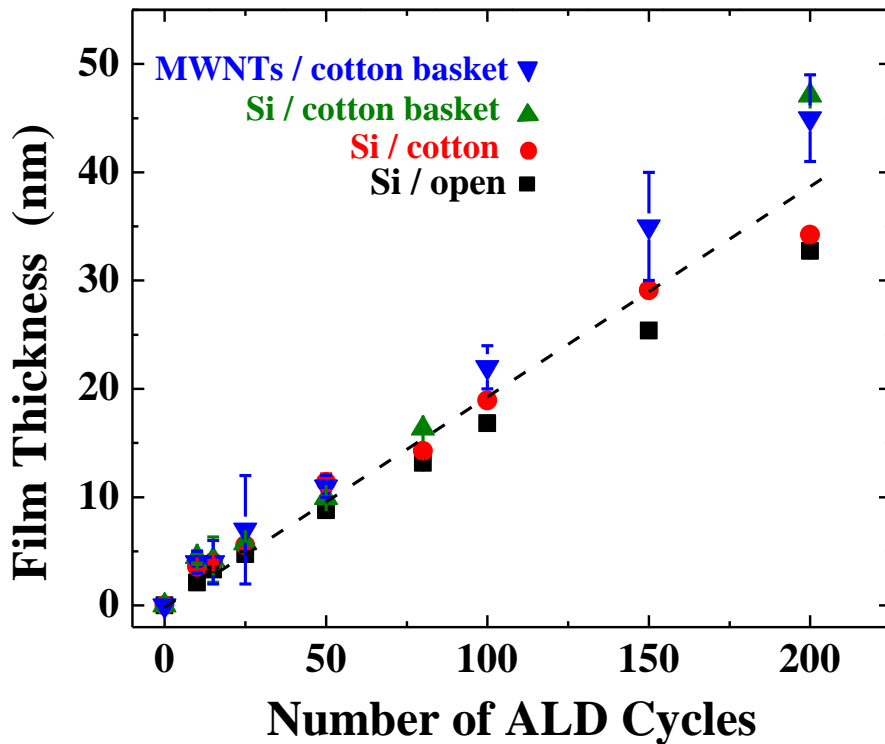


**Figure 4.7:** Graph comparing ALD growth on Si wafers and MWNTs where the substrates (Si and nanotubes) are encased in cotton fiber baskets. The plot also includes thickness measured on silicon when the substrate is directly wrapped in cotton (without the basket) (labeled “Si / cotton”) and when no fiber containment is present (labeled “Si / open”). The growth increases linearly with cycle number at about the same rate observed for fibers encased in polypropylene (Figure 4.4). The film thickness on all substrates follows a similar trend, with some deviation present for larger number of cycles.

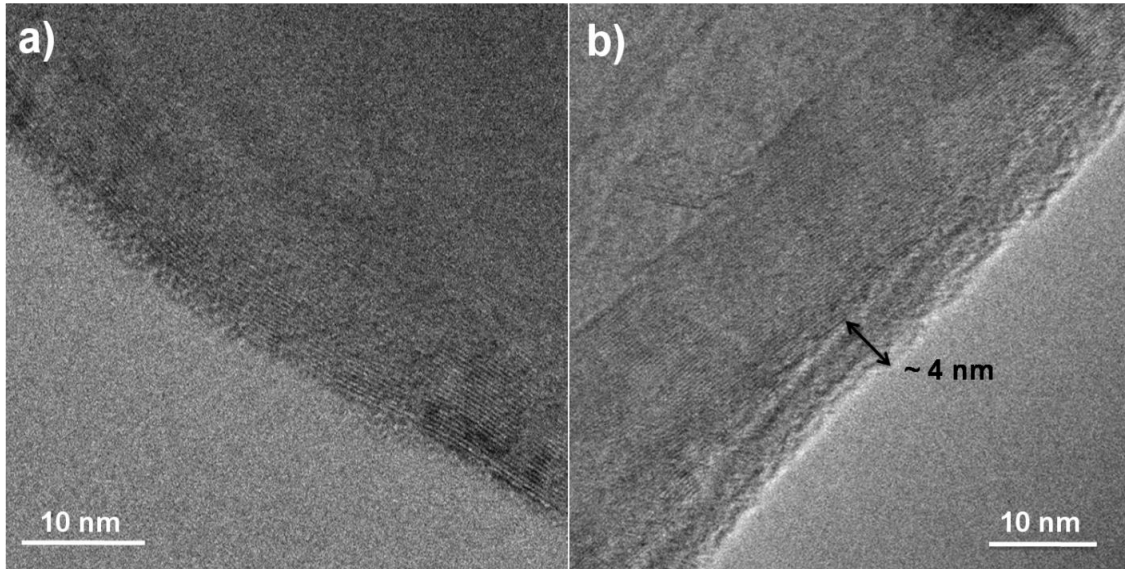


**Figure 4.8:** TEM images of MWNTs coated using the basket method with a cotton fiber wrapping. These nanotubes were coated with 50 cycles of Al<sub>2</sub>O<sub>3</sub> ALD at 90°C using a recipe of 1s TMA/30s N<sub>2</sub>/1s H<sub>2</sub>O/30s N<sub>2</sub>. This recipe resulted in nanotubes with a range of film thicknesses from a) no coating to b) coatings up to approximately 4 nm. The variation in film conformality is likely due to inadequate diffusion of precursor gases through the cotton fiber wrap.

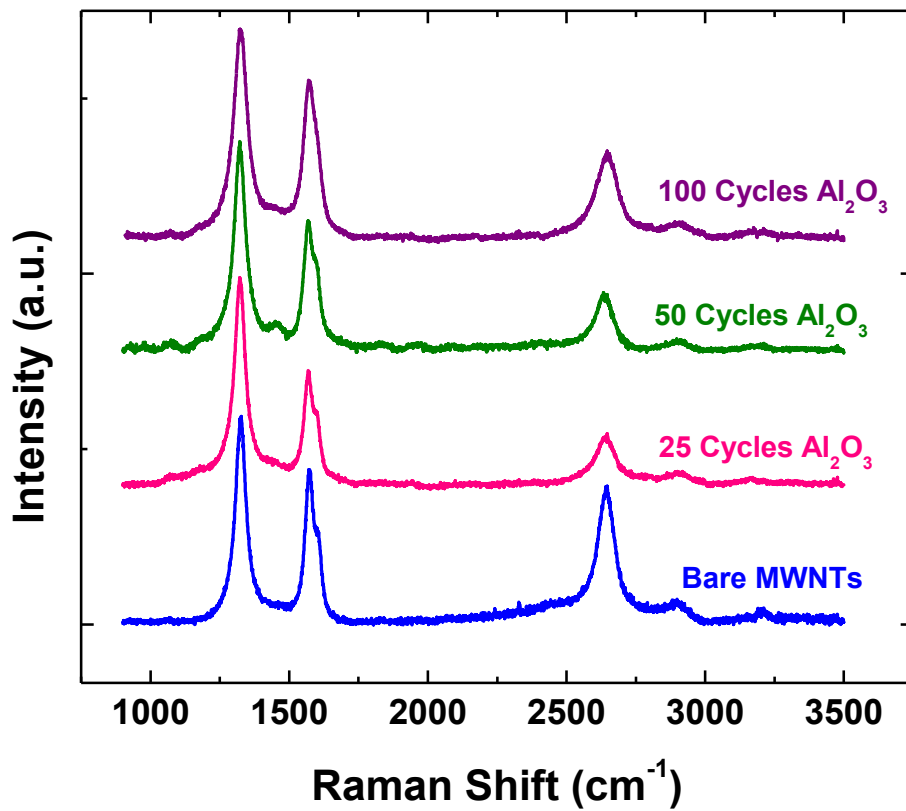


**Figure 4.9:** Raman spectra of MWNTs treated with a) 0 cycles b) 25 cycles c) 50 cycles and d) 100 cycles of Al<sub>2</sub>O<sub>3</sub> ALD. The spectra show peak locations typically associated with MWNTs.

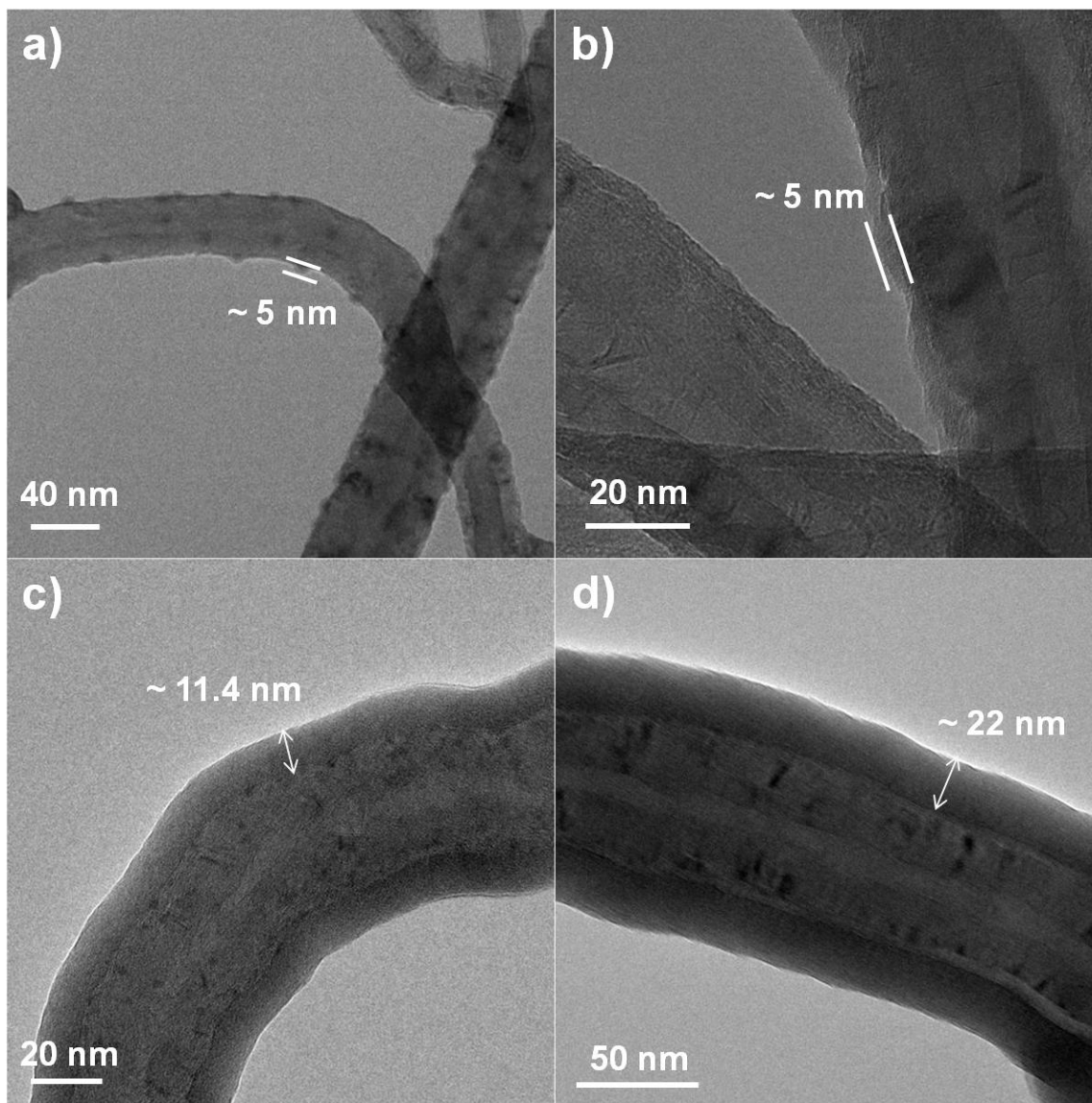


**Figure 4.10:** TEM images from MWNTs mounted on grids prior to deposition. (a) After 10 cycles of  $\text{Al}_2\text{O}_3$  ALD, nodular nuclei are readily seen. (b) After 15 cycles, the nuclei have grown into a rough but cohesive film coating. (c) After 100 and (d) 200 cycles, a smooth and conformal film coating is achieved. This trend follows closely that shown in Figures 4.3 and 4.5, obtained when the same type of nanotubes are coated using the fiber basket method.

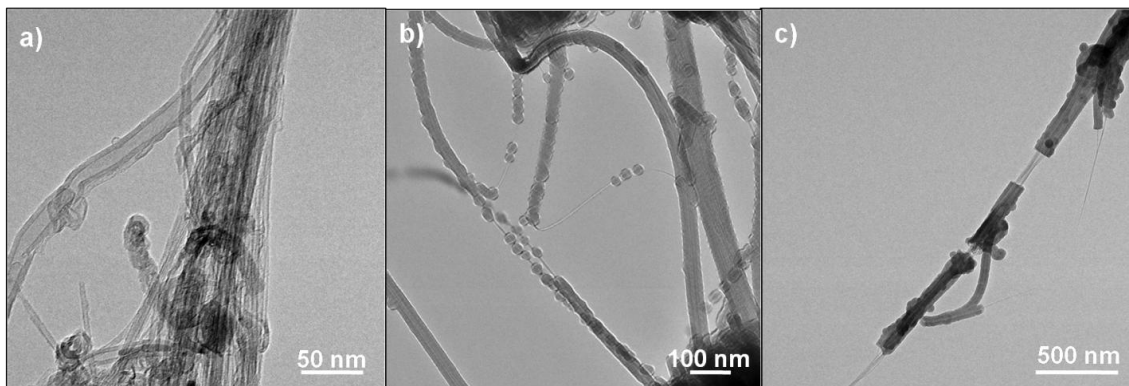


**Figure 4.11:** (a) SWNTs as received; and (b) after coating with 100; and (c) 200 cycles of Al<sub>2</sub>O<sub>3</sub> ALD. Samples were mounted onto a TEM grid prior to deposition. The coating thickness is approximately  $8 \pm 2$  nm after 100 cycles and  $20 \pm 3$  nm after 200 cycles. The rope-like aggregates were coated with a relatively uniform coating, whereas individual single-walled nanotubes demonstrated nodular growth. After 200 cycles, the nodules began to grow together into a cohesive film.

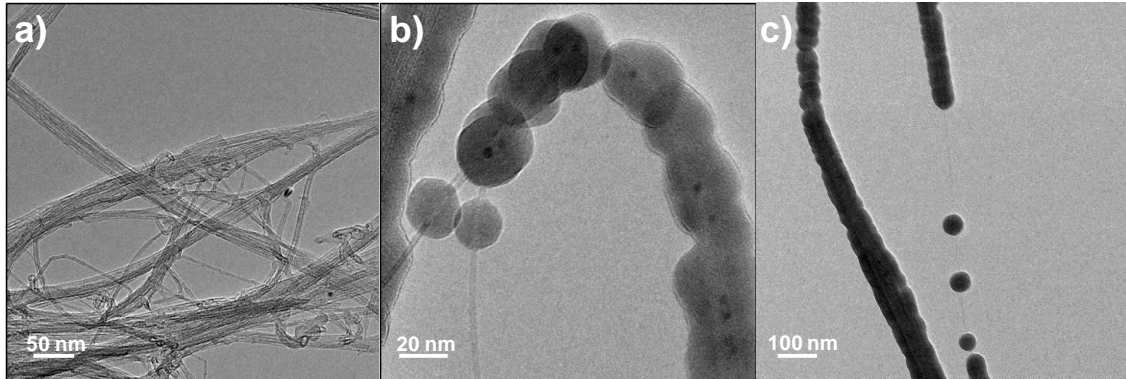


**Figure 4.12:** TEM images of DWNTs (a) uncoated; (b) and after 100; and (c) 200 cycles of  $\text{Al}_2\text{O}_3$  ALD coating. The DWNTs showed nodular growth at 100 cycles. By 200 cycles some of the nodules had grown together to form a more continuous coating, however, many uncoated regions remained. The nodule radius was approximately  $10 \pm 2$  nm for the 100 cycle sample. The film thickness for the 200 cycles sample had increased to approximately  $21 \pm 3$  nm for the coated portions of the 200 cycle sample. This is consistent with nucleation on defects, followed by facile film growth with little additional film nucleation on this particular nanotube type.

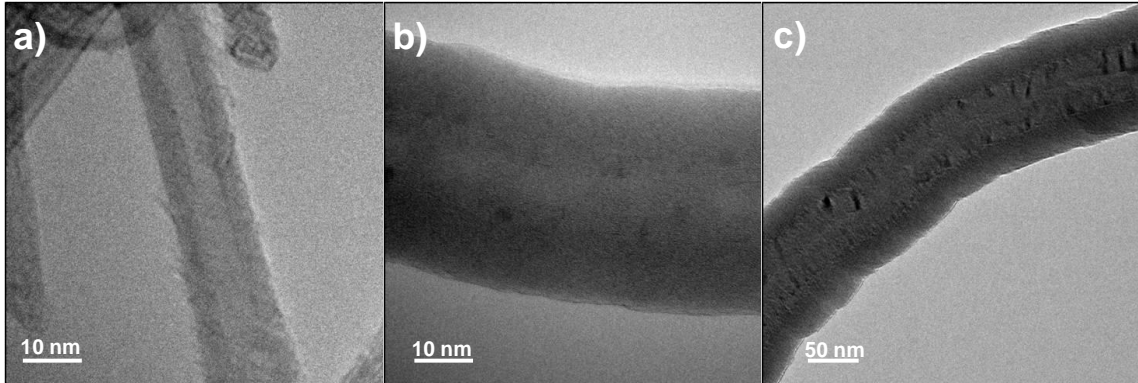


**Figure 4.13:** TEM images of (a) uncoated functionalized MWNTs (b) functionalized MWNTs coated with 100 cycles of Al<sub>2</sub>O<sub>3</sub> ALD and (c) functionalized MWNTs coated with 200 Al<sub>2</sub>O<sub>3</sub> ALD. The coating thickness was approximately  $11.8 \pm 0.6$  nm for the 100 cycle sample and  $23 \pm 2$  nm for the 200 cycle sample. The coatings were smooth and conformal for both the 100 and 200 cycle samples.

## References

- (1) Harris, P. J. F. *Carbon Nanotube Science*; Cambridge University Press: New York, 2009.
- (2) Schnorr, J. M.; Swager, T. M. *Chem. Mat.* **2011**, *23*, 646.
- (3) Dai, H. J. *Accounts Chem. Res.* **2002**, *35*, 1035.
- (4) Eder, D. *Chem. Rev.* **2010**, *110*, 1348.
- (5) Donaldson, K.; Poland, C. A. *Nat. Nanotechnol.* **2009**, *4*, 708.
- (6) Ryman-Rasmussen, J. P.; Cesta, M. F.; Brody, A. R.; Shipley-Phillips, J. K.; Everitt, J. I.; Tewksbury, E. W.; Moss, O. R.; Wong, B. A.; Dodd, D. E.; Andersen, M. E.; Bonner, J. C. *Nat. Nanotechnol.* **2009**, *4*, 747.
- (7) Ryman-Rasmussen, J. P.; Tewksbury, E. W.; Moss, O. R.; Cesta, M. F.; Wong, B. A.; Bonner, J. C. *Am. J. Respir. Cell Mol. Biol.* **2009**, *40*, 349.
- (8) Lam, C. W.; James, J. T.; McCluskey, R.; Hunter, R. L. *Toxicol. Sci.* **2004**, *77*, 126.
- (9) Warheit, D. B.; Laurence, B. R.; Reed, K. L.; Roach, D. H.; Reynolds, G. A. M.; Webb, T. R. *Toxicol. Sci.* **2004**, *77*, 117.
- (10) Shvedova, A. A.; Kisin, E. R.; Mercer, R.; Murray, A. R.; Johnson, V. J.; Potapovich, A. I.; Tyurina, Y. Y.; Gorelik, O.; Arepalli, S.; Schwegler-Berry, D.; Hubbs, A. F.; Antonini, J.; Evans, D. E.; Ku, B. K.; Ramsey, D.; Maynard, A.; Kagan, V. E.; Castranova, V.; Baron, P. *Am. J. Physiol.-Lung Cell. Mol. Physiol.* **2005**, *289*, L698.

- (11) Muller, J.; Huaux, F.; Moreau, N.; Misson, P.; Heilier, J. F.; Delos, M.; Arras, M.; Fonseca, A.; Nagy, J. B.; Lison, D. *Toxicol. Appl. Pharmacol.* **2005**, *207*, 221.
- (12) Sun, Z.; Nicolosi, V.; Rickard, D.; Bergin, S. D.; Aherne, D.; Coleman, J. N. *J. Phys. Chem. C* **2008**, *112*, 10692.
- (13) Chen, L. F.; Xie, H. Q. *Thermochim. Acta* **2010**, *497*, 67.
- (14) Jiang, L. Q.; Gao, L.; Sun, J. *Journal of Colloid and Interface Science* **2003**, *260*, 89.
- (15) Herrmann, C. F.; Fabreguette, F. H.; Finch, D. S.; Geiss, R.; George, S. M. *Appl. Phys. Lett.* **2005**, *87*, 3.
- (16) Min, Y. S.; Bae, E. J.; Jeong, K. S.; Cho, Y. J.; Lee, J. H.; Choi, W. B.; Park, G. S. *Adv. Mater.* **2003**, *15*, 1019.
- (17) Farmer, D. B.; Gordon, R. G. *Nano Lett.* **2006**, *6*, 699.
- (18) Cavanagh, A. S.; Wilson, C. A.; Weimer, A. W.; George, S. M. *Nanotechnology* **2009**, *20*, 255602.
- (19) McCormick, J. A.; Cloutier, B. L.; Weimer, A. W.; George, S. M. *J. Vac. Sci. Technol. A* **2007**, *25*, 67.
- (20) King, D. M.; Spencer, J. A.; Liang, X.; Hakim, L. F.; Weimer, A. W. *Surf. Coat. Technol.* **2007**, *201*, 9163.
- (21) Jur, J. S.; Spagnola, J. C.; Lee, K.; Gong, B.; Peng, Q.; Parsons, G. N. *Langmuir* **2010**, *26*, 8239.

- (22) Spagnola, J. C.; Gong, B.; Arvidson, S. A.; Jur, J. S.; Khan, S. A.; Parsons, G. N. *J. Mater. Chem.* **2010**, *20*, 4213.
- (23) Hyde, G. K.; Park, K. J.; Stewart, S. M.; Hinestroza, J. P.; Parsons, G. N. *Langmuir* **2007**, *23*, 9844.
- (24) Hyde, G. K. S., G.; Spagnola, J. C.; Peng, Q.; Lee, K.; Gong, B.; Roberts, K. G.; Roth, K. M.; Hanson, C. A.; Devine, C. K.; Stewart, S. M.; Hojo, D.; Na, J.-S.; Jur, J. S.; Parsons, G. N. *Langmuir* **2009**.
- (25) Hyde, G. K.; McCullen, S. D.; Jeon, S.; Stewart, S. M.; Jeon, H.; Lobo, E. G.; Parsons, G. N. *Biomed. Mater.* **2009**, *4*.
- (26) Kucheyev, S. O.; Biener, J.; Wang, Y. M.; Baumann, T. F.; Wu, K. J.; van Buuren, T.; Hamza, A. V.; Satcher, J. H.; Elam, J. W.; Pellin, M. J. *Appl. Phys. Lett.* **2005**, *86*.
- (27) Knez, M.; Niesch, K.; Niinisto, L. *Adv. Mater.* **2007**, *19*, 3425.
- (28) Saito, R.; Jorio, A.; Souza, A. G.; Dresselhaus, G.; Dresselhaus, M. S.; Pimenta, M. A. *Phys. Rev. Lett.* **2002**, *88*.
- (29) Chakrapani, N.; Curran, S.; Wei, B. Q.; Ajayan, P. M.; Carrillo, A.; Kane, R. *S. J. Mater. Res.* **2003**, *18*, 2515.
- (30) Murphy, H.; Papakonstantinou, P.; Okpalugo, T. I. T. *J. Vac. Sci. Technol. B* **2006**, *24*, 715.
- (31) Zhan, G. D.; Du, X. H.; King, D. M.; Hakim, L. F.; Liang, X. H.; McCormick, J. A.; Weimer, A. W. *J. Am. Ceram. Soc.* **2008**, *91*, 831.

## **CHAPTER 5. Atomic Layer Deposition of Zinc Oxide on Multiwall Carbon Nanotubes**

### **Abstract**

The deposition of thin films on carbon nanotubes is used to alter surface energy for improved solubility, added functionality, the decoration of biomolecules, and for photocatalytic functionality, among others. We used fiber containment methods to deposit zinc oxide (ZnO) thin films on multiwall carbon nanotubes (MWCNTs) by atomic layer deposition (ALD). Extended precursor dose and soak periods were developed to allow the precursor gases to diffuse through the fiber containment unit. The ALD coating thickness scaled linearly with the number of ALD cycles, and the extended dose and soak periods produced thicker coatings compared to traditional CNT coating methods. That is, the CNT controls not encased in the fibers produced thinner coatings, thus suggesting variation due to the extended reactant dose. The deposition of ZnO films is not uniform on the nanotubes with some CNTs showing no coating, some with ZnO nucleation, whereas others have thick coatings. Moreover, the morphology of the deposited films is rough with ZnO particles nucleating and coalescing into a roughened film.

## 5.1 Introduction

Carbon nanotubes (CNTs) have unique mechanical, electrical, and thermal properties due to their size and surface chemistry<sup>1</sup>. The unique properties of CNTs creates a market for various applications that include drug delivery, transparent conductive coatings, chemical sensors, electrodes for use in organic light-emitting diodes or lithium ion batteries, capacitors, field effect transistors, actuators, and for use in filtration applications<sup>1-4</sup>. Pristine carbon nanotubes are relatively inert and require further functionalization to improve reactivity, solubility, and biocompatibility. As described in Chapter 4, safe handling of CNTs is an important consideration as reports of potential hazards associated with nanotube inhalation are raising concerns<sup>5-11</sup>. The addition of a thin film changes the surface energy and reactivity of CNTs and may decrease the associated respiratory dangers. One method of adding thin films to CNTs and other carbonaceous materials is atomic layer deposition (ALD).

Atomic layer deposition is used because it is capable of diffusing through high surface materials such as nanotubes, thereby depositing thin films with near monolayer control over thickness. The application of atomic layer deposition has been shown to deposit uniform and conformal aluminum oxide ( $\text{Al}_2\text{O}_3$ ) films on multiwall carbon nanotubes (MWCNTs)<sup>12-14</sup>. In comparison to  $\text{Al}_2\text{O}_3$ , zinc oxide (ZnO) films deposited on nanotubes do not exhibit a smooth morphology. The surface of nanotubes after the deposition of ZnO by ALD has a rough surface with ZnO particles forming on the surface<sup>15-18</sup>. The deposition of ZnO is of interest because it is an n-type semiconductor with a wide band gap of 3.37 eV and

a high exciton binding energy of 60 meV at room temperature<sup>19</sup>. The creation of zinc oxide-carbon nanotubes composite materials has been shown to create sensors for ammonia<sup>20</sup>, flexible organic photovoltaics<sup>21</sup>, field emission devices<sup>22</sup>, and as UV photodetectors<sup>18</sup>. While the deposition of ZnO on carbon nanotubes by ALD has been studied, the methods for depositing thin films on nanotubes to-date have been largely devoted to anchoring the CNTs onto a substrate. For our work we use the fiber containment methods described in Chapter 4 to coat unanchored multiwall carbon nanotubes. The ability of the fiber containment method, the ALD recipe parameters, and morphology of the resulting ZnO-CNT materials are analyzed.

## **5.2 Experimental Methods**

### **5.2.1 Multiwall Carbon Nanotube Preparation and Containment for ALD Coating**

The multiwall nanotubes used in this study were purchased from Helix Material Solutions. The nanotubes were used as received. The basket was made of a screen made of metal wires with ~ 0.7 mm diameter in a 1.5 mm square grid pattern was formed into a cylindrical scaffold approximately 3 cm long and 2 cm in diameter then wrapped with a woven cotton fiber cloth obtained from Textile Innovators. The fiber sheet secures the nanotubes in the basket while allowing the precursor and reactant gases to readily diffuse through the fibers and reach the nanotube samples. Each basket was loaded with approximately 30-50 mg of nanotubes before being enclosed using polyimide film tape. The basket was capable of holding roughly 200 mg of material, however they were not fully loaded, which may allow some nanotube movement inside the basket during processing. To

avoid user exposure to nanotubes, all carbon nanotube handling, storage, and transfer to the fiber carriers was performed in a bench-top nitrogen-purged glove box (LC Technology Solutions).

### **5.2.2 Preparation of Nanotube Control Samples**

In addition to the encased CNTs, some control samples were prepared directly onto TEM grids. To prepare the controls, approximately 10 mg of nanotubes were suspended in 20 ml of methanol and sonicated for 15 minutes. A small amount of the sonicated solution was transferred by pipette onto a holey carbon TEM grid, and the methanol was evaporated in air before loading the grid into the reactor. The grids were anchored in the reactor using an alligator clip secured to the sample boat.

### **5.2.3 ALD Film Coating**

After filling and securing the fiber basket holders with CNTs in the glove box, the samples were transported by hand from the glovebox to the ALD reactor chamber. The nanotube-loaded baskets were placed onto a large sample boat and transferred into the heated zone of a hot-wall viscous-flow ALD reactor.

The reactants for deposition were diethyl zinc (DEZ) and water. The ALD runs were performed at 100°C and ~2.0 Torr, and between ~25 and 200 ALD cycles were used for coating. To help ensure the precursor gases diffused throughout the CNT fiber samples, we used extended precursor soaks during the ALD runs. The soak steps consisted of flowing TMA for 5 seconds, then the gas inlet and outlet valves were closed to produce a static gas exposure in the reactor for 120 seconds. Following the soak, the chamber was purged for

120s using purified nitrogen gas. The water exposure also followed the same flow and soak-time sequence, followed by another N<sub>2</sub> purge for 120s. The flow/soak sequence is designated as DEZ/N<sub>2</sub>/H<sub>2</sub>O/N<sub>2</sub> = 5(120)/120/5(120)/120 seconds. For CNT samples on the TEM grids, the ALD sequence used a 2s DEZ dose followed by a 50s N<sub>2</sub> purge. The same sequence was used for the water dose.

#### **5.2.4 Characterization of Coated CNTs**

After coating, the carbon nanotubes were collected and analyzed. After ALD coating, the fiber baskets were returned to the glovebox and the coated nanotubes were emptied into a scintillation vial. Small samples of the CNTs coated using the fiber basket method, as well as those coated directly on the control TEM grids were analyzed using an FEI Tecnai G<sup>2</sup> Twin transmission electron microscope. The thickness of the nanotubes was estimated from the TEM images using ImageJ software. Selected representative images are shown in the figures. Raman spectra were collected for the MWNTs using a Horiba-Jobin Yvon LabRAM HR VIS confocal microscope with a 632 nm laser source. The spectrometer was calibrated using the crystalline silicon peak at 520.7 cm<sup>-1</sup>.

### **5.3 Results**

Figure 5.1 presents TEM images of multiwall CNTs after 25, 40, 50, 80, 100 and 150 ALD cycles, where the nanotubes were coated using the basket method. The morphology of the zinc oxide coated nanotubes is similar to results seen in literature<sup>15-18</sup>. The zinc oxide begins to nucleate after 25 cycles of ALD, where the nuclei have thicknesses of ~7±2 nm. As the number of cycles is increased, the nuclei coalesce and after 50 cycles some nanotubes

have continuous ZnO coatings. The coatings are rough and appear to be ZnO particles that deposit along the nanotube surface. Even after 150 cycles, there are some nanotubes that are in the nucleation stage and others that have no coating at all as demonstrated in Figure 5.1f. The average film thickness, taking into account only the ZnO present on the CNTs and not the uncoated portions, increases linearly with cycle number on all analyzed surfaces as demonstrated in Figure 5.2. The film thickness for the MWNTs was estimated from TEM images, and thickness on Si was determined by ellipsometry. Several different silicon samples were measured, including silicon wrapped directly in cotton (Cotton Si) and silicon with no fiber wrapping (Si). We see that both silicon samples and the MWNTs result in films with very similar coating thicknesses, confirming that under the conditions used, the fiber wrapping does not strongly affect the film growth. The line in Figure 5.2 shows the deposition rate to be  $\sim 2 \text{ \AA/cycle}$  on the CNTs and on the silicon, similar to the  $\sim 2 \text{ \AA/cycle}$  typically observed for ZnO ALD at  $100^\circ\text{C}$ <sup>23</sup>. Figure 5.3 shows the morphology of the nanotubes coated on TEM grids using the 2/50/2/50s ALD recipe. The morphology of the grid-loaded samples is similar to the samples coated using the basket method, but the ZnO film is slightly thinner, as shown graphically in Figure 5.4. The growth rate for the MWCNTs coated using the basket method is  $\sim 2 \text{ \AA/cycle}$  as mentioned previously whereas the growth rate for the grid-loaded nanotubes is  $\sim 1.5 \text{ \AA/cycle}$ . The grid-loaded nanotubes are much more uniform with all nanotubes on the grid showing similar film thicknesses.

Carbon nanotubes were also coated using short soaks and purges, specifically a 60s soak and a 90s purge. Figure 5.5 shows TEM images of nanotubes coated with 50 cycles using the shorter recipe. The ZnO growth on samples coated with shorter soak/purge periods

has the same growth variability between nanotubes coated in the same sample run as the samples using the longer soak/purge periods. Some nanotubes had films  $\sim 11 \pm 3$  nm in thickness whereas others are only decorated with ZnO nuclei. The ZnO film thickness for nanotubes coated with 50 cycles using the longer soak/purge sequence is higher at  $13 \pm 2$  nm. The difference between the average film thicknesses for the two samples is not very large, indicating shorter processing times may be sufficient.

Raman spectra were collected for bare MWNTs as well as those coated with 50, and 100 cycles of ZnO, as shown in Figure 5.6. The spectra are typical of MWNTs, including the D, G, D', and G' peaks near  $1320$ ,  $1570$ ,  $1600$  and  $2640$   $\text{cm}^{-1}$ , respectively<sup>24-26</sup>. The spectra in the figure are normalized to the D peak in order to probe changes in the G and G'. The G peak corresponds to the graphitic carbon signal, and the relative size of the other peaks is often related to disorder and defects, which are substantial in these MWNT materials. Upon ALD coating, changes and trends are detected in the Raman signal, but generally, the primary signatures of the CNT's are still present, demonstrating that the CNT structure is mostly maintained upon ALD coating. Moreover, the peak emerging around  $1080$   $\text{cm}^{-1}$  after 50 cycles of ZnO ALD is associated with the growth of zinc oxide on the nanotubes<sup>27</sup>.

#### 5.4 Discussion

The growth rate of  $\sim 2$  Å/cycle measured on the MWCNTs coated in the basket is similar to what has been observed on planar silicon substrates making it appear that the purging time is successful for removing any remaining byproduct or unreacted precursor in the fiber basket for ALD growth. However, the density of reactive surface sites on the

carbon nanotubes is much lower than the density of reactive site on a silicon wafer. The expected growth rate on the nanotubes is closer to the growth rate on the grid-loaded CNTs ( $\sim 1.5 \text{ \AA/cycle}$ ), as they are a baseline for the normal growth rate of ZnO on the MWCNTs. In comparison, the elevated growth rate on the basket loaded CNTs indicates the fiber containment is still affecting growth and likely leading to CVD. It is possible that with longer purge times the growth rate may become more similar to what is seen on the grid-loaded CNTs.

The variability in the film thickness between nanotubes in the same ALD deposition may be due to the size of the DEZ molecule. Diethyl zinc is much larger than TMA and its size may make it more difficult to diffuse through the cotton fibers and subsequently throughout the CNT powder. However, the grid-loaded nanotubes did not show variability between nanotubes and were all coated to the same degree. Fewer nanotubes were loaded on to the grids so the precursors did not have to diffuse through thick powders or the fiber containment unit. Using a more porous fiber mat for containment may facilitate DEZ diffusion into the fiber basket and improve uniformity. In contrast, the zinc oxide on the cotton wrapped silicon was uniform and conformal. Therefore, the DEZ may have more difficulty diffusing throughout the CNT powder as opposed to the fiber containment, and by decreasing the amount of CNTs in the containment basket the DEZ may more readily diffuse throughout the powder. In addition, diethyl zinc may also have a lower reactivity compared to the TMA reaction discussed in Chapter 4. The TMA molecule may be able to etch the surface of the nanotubes creating new reactive sites and increasing the degree of chemical bonds between the coating and the nanotubes. That is, diethyl zinc may not etch the

nanotube and create reactive sites. Instead, diethyl zinc may only react with the defect sites already present on the CNTs. Considering that defect sites act as locations for nucleation of ZnO film growth, if fewer defect sites or anchoring points for the film are available, there may be a decrease in the adhesion of the ZnO coating to the nanotubes. In several TEM images, portions of the zinc oxide coating were seen separated from the nanotubes. With fewer chemical bonds between the CNT and the ZnO coating it would be much easier for the film to detach, leading to the bare sections of nanotubes seen in the TEM images.

## 5.5 Conclusion

In conclusion, we have shown the fiber basket method of coating carbon nanotubes is only successful to a certain degree for use with zinc oxide ALD precursors using the processing parameters described. The zinc oxide films appear to nucleate as ZnO particles which coalesce as the number of ALD cycles is increased, thus forming rough continuous films. The film growth increases linearly with increasing ALD cycle number for CNTs coated in the basket and the grid-loaded control samples. The basket coated samples had a growth rate of  $\sim 2 \text{ \AA}/\text{cycle}$ , higher than the grid-loaded samples which had a growth rate of  $1.5 \text{ \AA}/\text{cycle}$ . Moreover, there was considerable variability between the nanotubes coated by the basket method in the same ALD deposition. It is possible that the larger size of the DEZ molecule prevents sufficient diffusion into the basket or CNT powder. If one increases in the pore size and porosity of the fiber matrix then it may be possible to increase the ZnO film uniformity on MWCNTs. As an alternative, decreasing the amount of CNTs in the basket may facilitate DEZ diffusion throughout the nanotube powder.

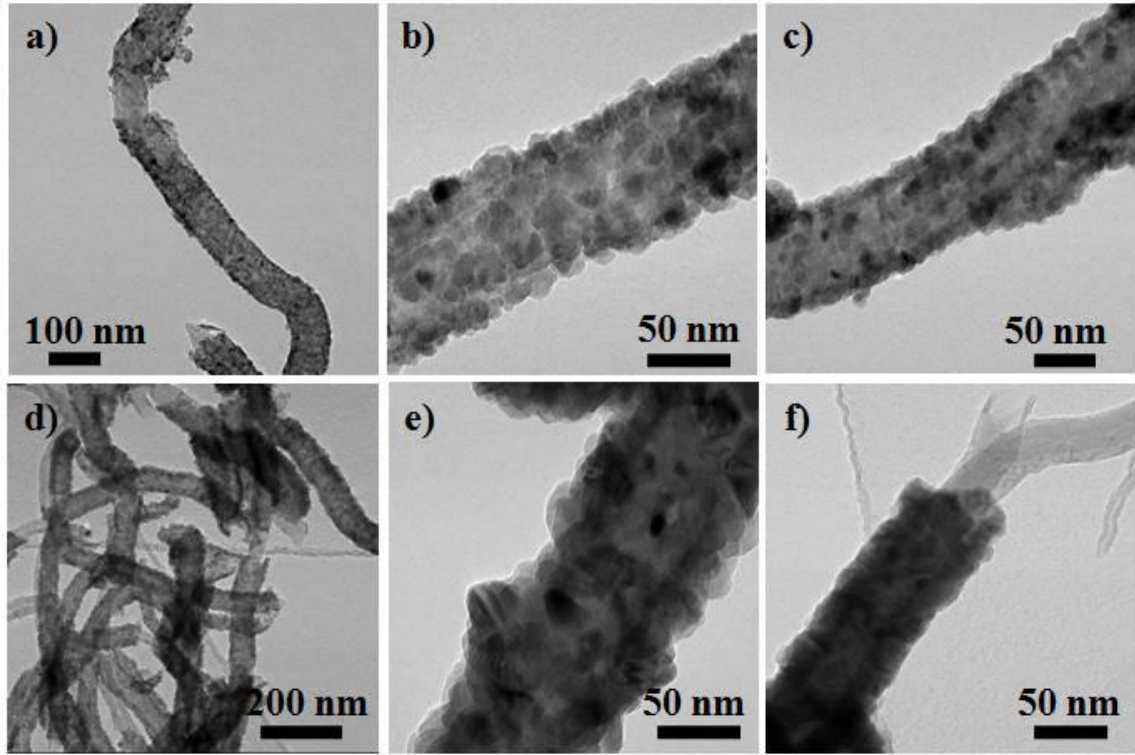


**Figure 5.1:** TEM images of MWCNTs coated with (a) 25, (b) 40, (c) 50, (d) 80, (e) 100, and (f) 150 cycles of ZnO by atomic layer deposition. Nucleation is occurring after 25 cycles and the film begins to coalesce as the number of ALD cycles increases. The film surface is rough and even with 150 cycles some portions of the nanotubes remained uncoated.

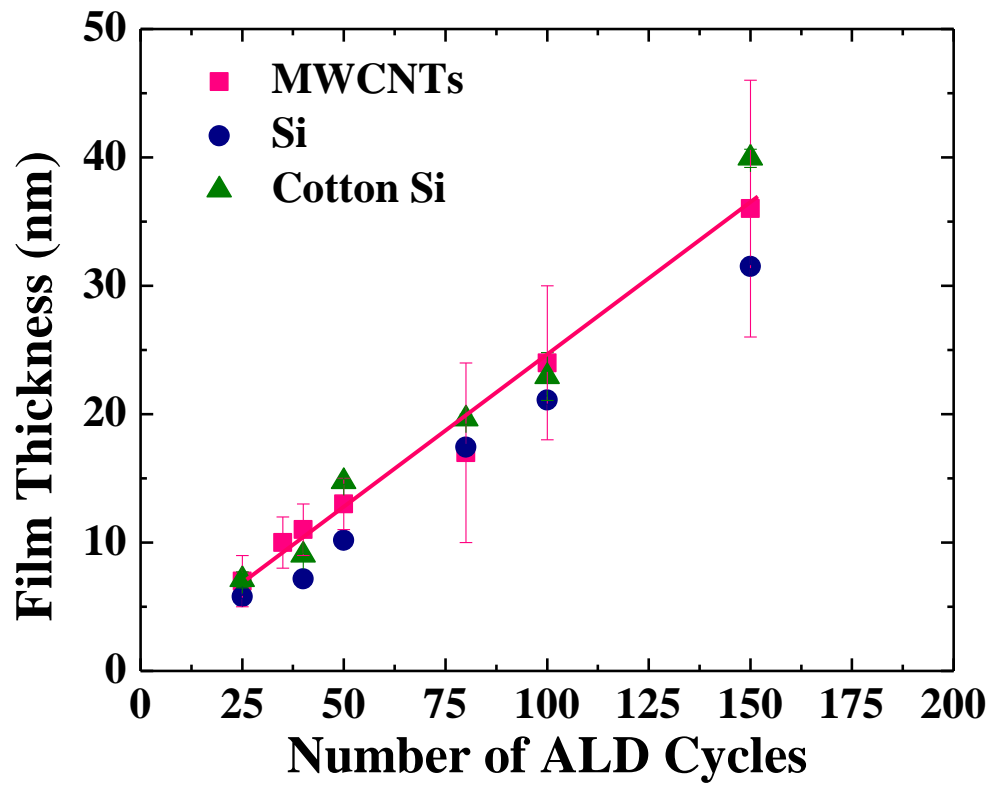


**Figure 5.2:** Film thickness varies linearly with the number of ALD cycles with a growth rate of  $\sim 2 \text{ \AA/cycle}$ , very similar to growth rates seen on planar samples at  $100^\circ\text{C}$ . The silicon sample wrapped in cotton simulated the film (Cotton Si) has film thicknesses very similar to the unwrapped silicon control (Si).

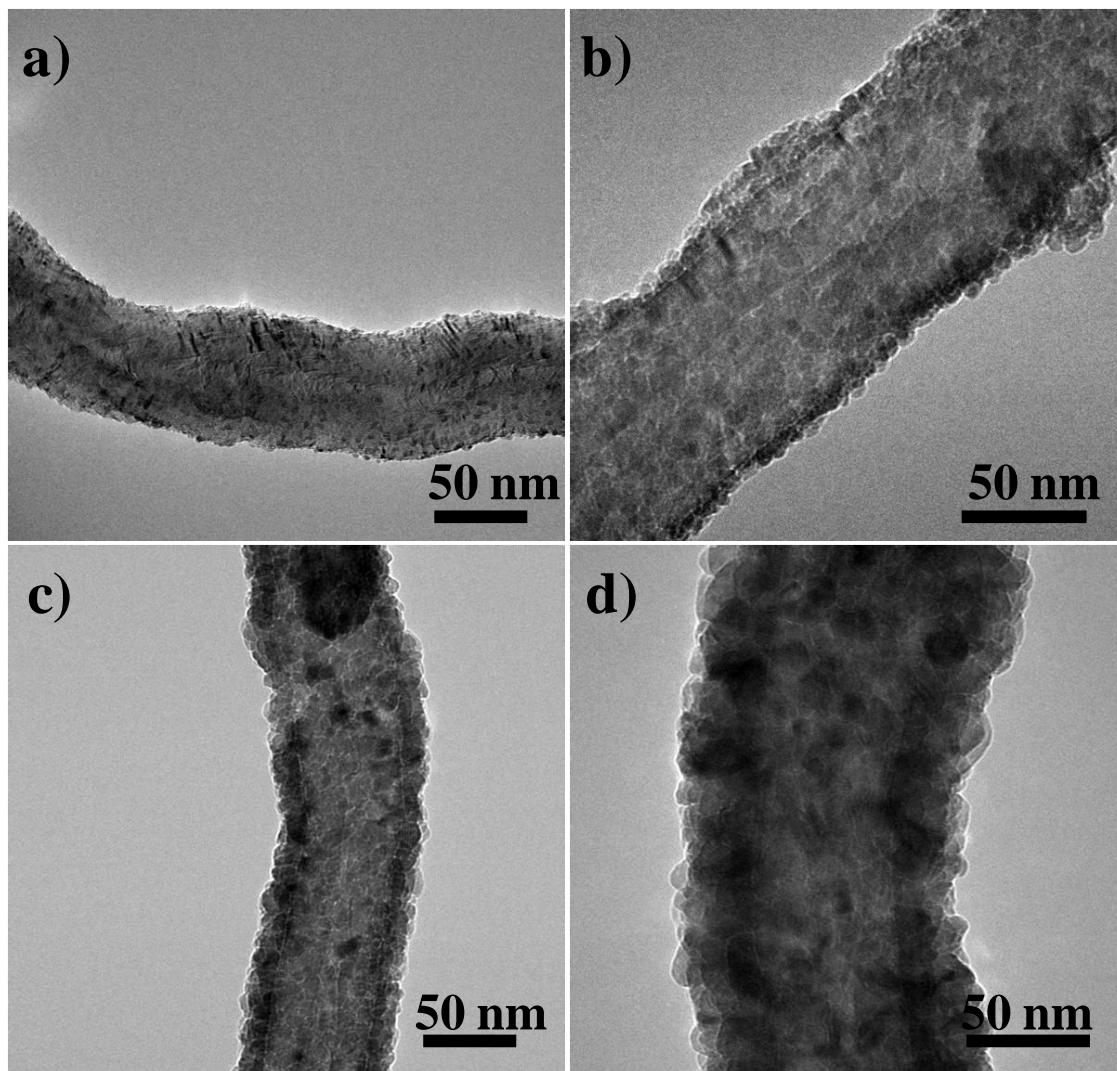


**Figure 5.3:** TEM images of MWCNTs coated with (a) 25, (b) 50, (c) 100, and (d) 200 cycles of ZnO ALD at 100°C. The nucleation and growth is similar to the basket coated samples with nucleation occurring at 25 cycles, however the growth is slower on the gird loaded samples.

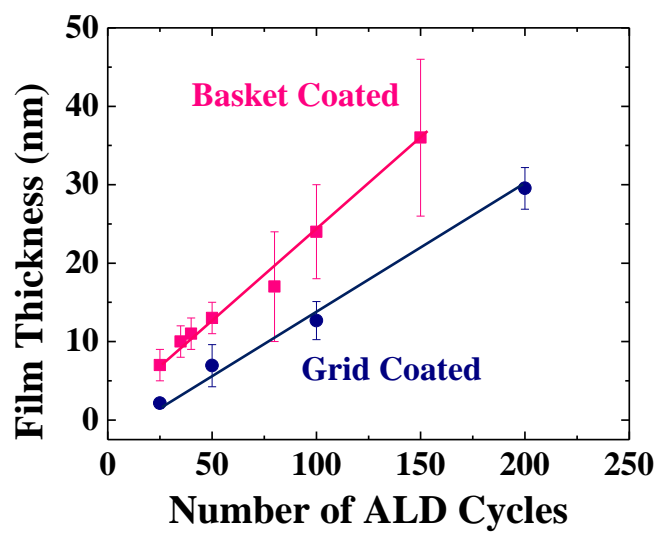


**Figure 5.4:** Film thickness by cycle number as determined by TEM for MWCNTs coated using the basket method and coated on the TEM grids. The growth is linear for both methods; however, the growth rate is much higher using the basket method.

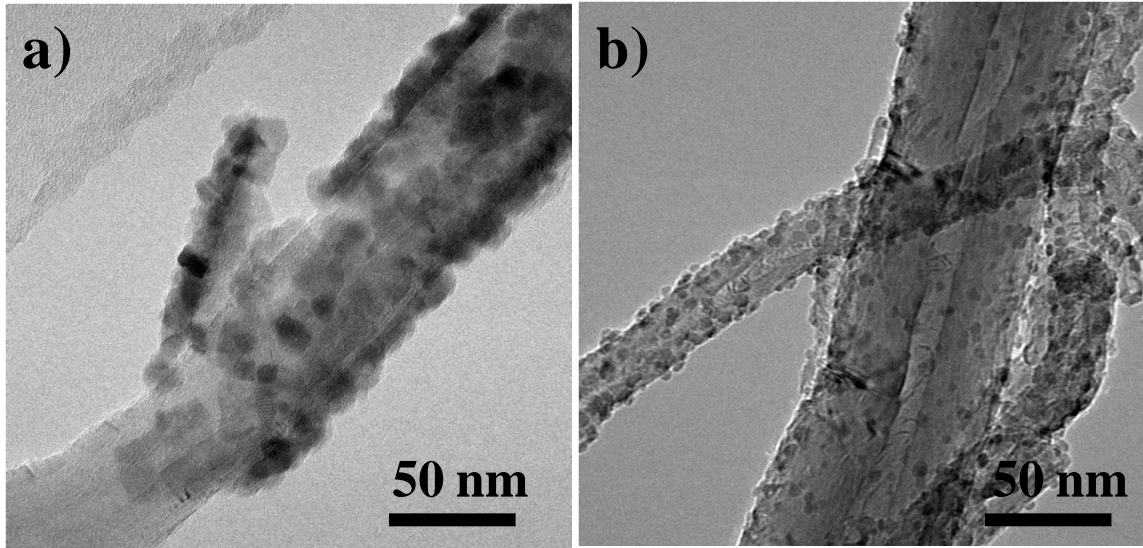


**Figure 5.5:** Multiwall carbon nanotubes coated with 50 cycles of ZnO using short soak and hold times. Some nanotubes showed films ~11 nm thick (a) while others only had sparse ZnO nuclei (b).

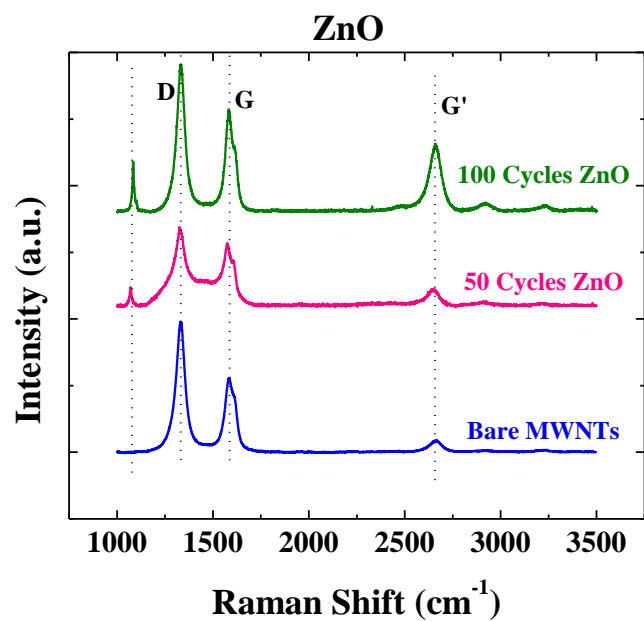


**Figure 5.6:** Raman spectra of uncoated MWNTs and MWNTs coated with 50 and 100 cycles of ZnO by ALD. The carbon nanotube structure is unchanged after the ZnO deposition.

## References

1. P. J. F. Harris, *Carbon Nanotube Science*. (Cambridge University Press, New York, 2009).
2. J. M. Schnorr and T. M. Swager, *Chem. Mat.* **23** (3), 646-657 (2011).
3. H. J. Dai, *Accounts Chem. Res.* **35** (12), 1035-1044 (2002).
4. D. Eder, *Chem. Rev.* **110** (3), 1348-1385 (2010).
5. K. Donaldson and C. A. Poland, *Nat. Nanotechnol.* **4** (11), 708-710 (2009).
6. J. P. Ryman-Rasmussen, M. F. Cesta, A. R. Brody, J. K. Shipley-Phillips, J. I. Everitt, E. W. Tewksbury, O. R. Moss, B. A. Wong, D. E. Dodd, M. E. Andersen and J. C. Bonner, *Nat. Nanotechnol.* **4** (11), 747-751 (2009).
7. J. P. Ryman-Rasmussen, E. W. Tewksbury, O. R. Moss, M. F. Cesta, B. A. Wong and J. C. Bonner, *Am. J. Respir. Cell Mol. Biol.* **40** (3), 349-358 (2009).
8. C. W. Lam, J. T. James, R. McCluskey and R. L. Hunter, *Toxicol. Sci.* **77** (1), 126-134 (2004).
9. D. B. Warheit, B. R. Laurence, K. L. Reed, D. H. Roach, G. A. M. Reynolds and T. R. Webb, *Toxicol. Sci.* **77** (1), 117-125 (2004).
10. A. A. Shvedova, E. R. Kisin, R. Mercer, A. R. Murray, V. J. Johnson, A. I. Potapovich, Y. Y. Tyurina, O. Gorelik, S. Arepalli, D. Schwegler-Berry, A. F. Hubbs, J. Antonini, D. E. Evans, B. K. Ku, D. Ramsey, A. Maynard, V. E. Kagan, V. Castranova and P. Baron, *Am. J. Physiol.-Lung Cell. Mol. Physiol.* **289** (5), L698-L708 (2005).

11. J. Muller, F. Huaux, N. Moreau, P. Misson, J. F. Heilier, M. Delos, M. Arras, A. Fonseca, J. B. Nagy and D. Lison, *Toxicol. Appl. Pharmacol.* **207** (3), 221-231 (2005).
12. C. F. Herrmann, F. H. Fabreguette, D. S. Finch, R. Geiss and S. M. George, *Appl. Phys. Lett.* **87** (12) (2005).
13. A. S. Cavanagh, C. A. Wilson, A. W. Weimer and S. M. George, *Nanotechnology* **20** (25) (2009).
14. C. K. Devine, C. J. Oldham, J. S. Jur, B. Gong and G. N. Parsons, *Langmuir* **27** (23), 14497-14507 (2011).
15. J. M. Green, L. F. Dong, T. Gutu, J. Jiao, J. F. Conley and Y. Ono, *J. Appl. Phys.* **99** (9) (2006).
16. X. L. Li, C. Li, Y. Zhang, D. P. Chu, W. I. Milne and H. J. Fan, *Nanoscale Research Letters* **5** (11), 1836-1840 (2010).
17. Y. S. Min, E. J. Bae, J. B. Park, U. J. Kim, W. Park, J. Song, C. S. Hwang and N. Park, *Appl. Phys. Lett.* **90** (26) (2007).
18. Y. H. Lin, P. S. Lee, Y. C. Hsueh, K. Y. Pan, C. C. Kei, M. H. Chan, J. M. Wu, T. P. Perng and H. C. Shih, *J. Electrochem. Soc.* **158** (2), K24-K27 (2011).
19. Z. L. Wang, *J. Phys.-Condes. Matter* **16** (25), R829-R858 (2004).
20. J. M. Tulliani, A. Cavalieri, S. Musso, E. Sardella and F. Geobaldo, *Sens. Actuator B-Chem.* **152** (2), 144-154 (2011).
21. H. E. Unalan, P. Hiralal, D. Kuo, B. Parekh, G. Amaratunga and M. Chhowalla, *J. Mater. Chem.* **18** (48), 5909-5912 (2008).

22. K. Yu, Y. S. Zhang, F. Xu, Q. Li, Z. Q. Zhu and Q. Wan, *Appl. Phys. Lett.* **88** (15) (2006).
23. J. Malm, E. Sahramo, J. Perala, T. Sajavaara and M. Karppinen, *Thin Solid Films* **519** (16), 5319-5322 (2011).
24. R. Saito, A. Jorio, A. G. Souza, G. Dresselhaus, M. S. Dresselhaus and M. A. Pimenta, *Phys. Rev. Lett.* **88** (2) (2002).
25. N. Chakrapani, S. Curran, B. Q. Wei, P. M. Ajayan, A. Carrillo and R. S. Kane, *J. Mater. Res.* **18** (10), 2515-2521 (2003).
26. H. Murphy, P. Papakonstantinou and T. I. T. Okpalugo, *J. Vac. Sci. Technol. B* **24** (2), 715-720 (2006).
27. R. Cusco, E. Alarcon-Llado, J. Ibanez, L. Artus, J. Jimenez, B. Wang and M. J. Callahan, *Phys. Rev. B* **75** (16) (2007).

CHAPTER 6 is a reprint from a manuscript published in the Journal of Vacuum Science and Technology A., 2013, McClure, C.D., Oldham, C.J., Walls, H.J., Parsons, G.N.

**CHAPTER 6. Large Effect of Titanium Precursor on Surface Reactivity and Mechanical Strength of Electrospun Nanofibers Coated with TiO<sub>2</sub> by Atomic Layer Deposition**

*Christina D. McClure, Christopher J. Oldham*

Department of Chemical and Biomolecular Engineering  
North Carolina State University, Raleigh NC 27695

*Howard J. Walls*

Research Triangle Institute  
Research Triangle Park NC 27709

*Gregory N. Parsons*

Department of Chemical and Biomolecular Engineering  
North Carolina State University, Raleigh NC 27695

## Abstract

Encapsulating and functionalizing polymer nanofibers can improve the polymers chemical resistance and surface reactivity, enabling new applications including biosensing, flexible electronics, gas filtration and chemical separations. Polymer fiber functionalization typically involves energy intensive wet chemical treatments and/or plasma exposure. Recent results show low temperature atomic layer deposition (ALD) to be a viable means to coat nanofibers with uniform and conformal inorganic and hybrid organic-inorganic layers. For this article, we describe how the mechanical properties of nylon-6 nanofibers are affected by ALD coatings of  $\text{TiO}_2$  and other metal oxides. We find that the stress-strain behavior of nylon-6 nanofibers depends strongly on the specific precursor chemistry used in the coating process. For ALD  $\text{TiO}_2$  coatings, titanium tetrachloride tended to embrittle the fibers, whereas titanium isopropoxide had a more subtle effect. Physical characterization shows that the  $\text{TiCl}_4$  diffused into the nylon-6 and reacted subsurface, whereas the titanium isopropoxide tended to react on the surface producing a more abrupt organic/inorganic interface. Results show that precursor choice is an important factor when designing thin film coating processes on polymeric substrates.

## 6.1 Introduction

Electrospinning readily produces polymer or inorganic fibers with diameters of 200 nanometers or less. Various electrospun polymers and inorganic materials are useful for filtration, tissue scaffolds, functional textiles, energy storage, chemical sensing and other systems.<sup>1,2</sup> While different polymers can each provide unique properties, further surface modification can enhance the fiber function, mechanical structure and/or application performance. Nanofiber surfaces are often modified by adding inorganic materials to the polymer solution during electrospinning,<sup>3-6</sup> or by wet chemical or vapor treatments after fiber formation.<sup>7-10</sup> Wet chemical methods often require drying treatments which can be energy intensive. Vapor treatments, including for example reactive plasma exposure,<sup>11-13</sup> or chemical vapor deposition<sup>14,15</sup> can lead to different surface terminations on the fiber mat top and bottom. Recent work shows that low temperature vapor infiltration<sup>16</sup> can dramatically change the mechanical response of fibers. Atomic layer deposition (ALD) can also modify polymer fibers and fiber mats by coating each polymer fiber with a uniform and highly conformal nanoscale inorganic or organic-inorganic thin film.<sup>17-23</sup> This method has been shown to alter surface reactivity and wetting.<sup>20</sup> Atomic layer deposition has been used with fibers to create magnetic and photocatalytic organic-inorganic composites,<sup>19</sup> to deposit SnO<sub>2</sub> for gas sensing,<sup>21</sup> and tungsten coatings for conductive fibers.<sup>23</sup> It could be helpful to alter the surface reactivity, for example, while simultaneously maintaining the mechanical elasticity of the polymer. On the other hand, some applications may benefit from the additional mechanical rigidity that an inorganic coating can provide. Previous results demonstrate that the ALD coatings on nylon nanofibers are sufficiently uniform and

conformal to achieve good fiber encapsulation, to create nanoscale fibers that are resistant to detrimental chemical exposure.<sup>18</sup> However, to date the mechanical properties of nanofibers coated by ALD is largely unstudied.

Atomic layer deposition utilizes sequential self-limiting surface reactions to deposit a thin film nearly one monolayer at a time. By controlling the number of self-limiting reactions taking place the resulting film thickness is carefully controlled. Therefore, we expect the ALD process may provide a means to tune the mechanical response of polymer fibers or other flexible filament media. This article specifically explores the effect of titanium ALD precursors on the structure of the resulting TiO<sub>2</sub> coating on nylon nanofibers, and how the coating and the specific precursor chemistry affect the resulting mechanical response of modified fiber mat structures.

## **6.2 Experimental**

### **6.2.1 Electrospun polymer fiber preparation**

Nylon nanofibers were electrospun using a solution of 20 wt % nylon (Ultramid B27 02 from BASF) in formic acid (88% Acros Organics, ACS Reagent). The solution was stirred in an oil bath at 60°C for approximately 2 hours until the nylon pellets had completely dissolved. This solution was used to electrospun the nylon nanofibers. We used a NESSE electrospinning set-up from Innovative Systems Design to produce the nylon nanofibers. The high voltage power supply was set to 20 kV and the syringe pump was set to approximately 250  $\mu$ L to keep a pressure of 2-3 psi on the solution. A 26-gauge needle with a blunt end was used for electrospinning. The distance between the high voltage needle and

the grounded 10” diameter collector plate was ~5.5”. The collector plate was wrapped with Reynolds Wrap Nonstick aluminum foil for fiber collection. Dry gas was set to flow parallel to the needle at a flow rate of approximately 2-3 liters/min. In addition to the dry gas, a jet gas flow at a flow rate of 4-5 liter/min was directed at the point of the needle tip at an angle of approximately 45°. The jet gas can be used to direct the fiber stream to ensure the entire collector is being coated. The nylon mats were electrospun for 2 hours at room temperature with a relative humidity of approximately 60%.

The electrospun fibers on foil were cut into strips 1 cm wide and 5.5 cm long and then removed from the foil using tweezers. The mat thickness was measured using a Thwing-Albert electronic thickness tester and found to be ~0.04 mm. The nylon strips were mounted on cardstock frames (Recollections®) as shown in Figure 6.1. Double sided Kapton tape was used to affix the mats to the frames. The inner dimension of the frame was 4.5 × 4.5 cm.

## **6.2.2 Fiber treatment and surface modification**

Atomic layer deposition was performed in a home built hot-wall viscous flow reactor described previously.<sup>18</sup> Aluminum oxide (Al<sub>2</sub>O<sub>3</sub>), zinc oxide (ZnO), and titanium dioxide (TiO<sub>2</sub>) were deposited on the nylon nanofibers. The metal containing precursors used were trimethyl aluminum (TMA, Strem Chemicals, 98%) and diethyl zinc (DEZ, Strem Chemicals, 95%) for aluminum oxide and zinc oxide respectively. For titanium dioxide the metal precursor was titanium tetrachloride (TiCl<sub>4</sub>, Gelest, 99%) or titanium (IV) isopropoxide (TIP, Acros Organics, 98%). For all processes, the oxygen containing precursor was deionized water (H<sub>2</sub>O). The deposition temperature was either 50°C or 105°C.

The carrier gas was high purity nitrogen (99.999%, Airgas) that was fed through a Drierite gas purifier. The operating pressure was approximately 3 Torr when depositing Al<sub>2</sub>O<sub>3</sub>, ZnO, and TiO<sub>2</sub> using TiCl<sub>4</sub> as a precursor. To deposit TIP a bubbling system was installed to bubble N<sub>2</sub> through the TIP liquid. The addition of this bubbling line increased the operating pressure to approximately 4 Torr. A schematic of the reactor is shown in Figure 6.2. The precursor dosing times are listed in Table 6.1. The TIP dosing time is split between the prep and dose step. During the prep step nitrogen is bubbled into the TIP to volatilize the TIP. After the prep step the TIP is dosed to the reactor for 0.5 s. To determine growth rate, each deposition run included a planar silicon wafer, and the film thickness was measured after each run using ellipsometry. On the silicon wafers, the growth per cycle at 105°C was 0.45±.07 and 0.26±.03 Å/cycle using TiCl<sub>4</sub> and TIP, respectively. At 50°C the growth rate increased to 0.97±.05 and 0.59±.03 Å/cycle respectively. Figure 6.3 shows film thickness on silicon vs. ALD cycle number for the chemistries and temperatures used. These growth rates are similar to what has been reported for these precursors,<sup>24-26</sup> however the value for TIP at 50°C is slightly higher than that reported by Xie et al.<sup>27</sup> Because the film thickness on the polymer fiber was not directly measured, the mechanical data reported below is plotted versus ALD cycle number for the different coatings. As a control, samples were also placed in the reactor at 50°C under nitrogen flow with a pressure of 3 Torr for approximately 2 hours to monitor the effect of temperature and pressure.

### 6.2.3 Morphology and chemical characterization

The morphology of the uncoated and coated fibers was analyzed using scanning electron microscopy (SEM). The SEM images were obtained at the NC State University

Analytical Instrumentation Facility using a JEOL 6400F field emission SEM and at the Shared Materials Instrumentation Facility at Duke University using a FEI XL30 SEM. Before imaging, the fibers were sputter coated using a Quorum Technologies Mini Sputter Coater (Model SC7620) equipped with a gold/palladium target. The current was set to ~20 mA and the samples were sputtered for approximately 90 seconds.

Cross-sectional TEM images of uncoated nylon nanofibers and nylon nanofibers coated with 200 cycles of either  $\text{TiCl}_4/\text{H}_2\text{O}$  or  $\text{TIP}/\text{H}_2\text{O}$  were collected at the Analytical Instrumentation Facility (AIF) at North Carolina State University. The samples were first microtomed at AIF and then imaged with a Hitachi HF2000 TEM with an accelerating voltage of 200 kV and a FE Tungsten source.

The chemical composition of the nylon fiber mats was assessed using Fourier transform infrared spectroscopy (FTIR) and X-ray photoelectron spectroscopy (XPS). The FTIR used was a Thermo Nicolet Magna 750, equipped with a nonpolarized IR beam, a KBr beamsplitter, and a deuterated triglycine sulfate detector. For each IR experiment, each fiber sample was weighed to be sure that for each fiber type, the same amount of fiber was present in the IR beam to help enable direct quantitative data comparison of extent of reaction after different precursor exposure. The surface of the fibers was analyzed with XPS using either a Riber XPS-3000 or a SPECS XPS, both equipped with an Mg anode source. The scans were calibrated by referencing to adventitious carbon at ~285 eV. The XPS studies were done at the AIF at NC State University.

#### 6.2.4 Mechanical Analysis

Several methods are commonly used to evaluate mechanical properties of traditional micron-scale fibers and fiber mats. For example, ASTM Standard D5035 describes a tensile method for measuring the breaking force and the elongation of textile fabrics. Most procedures known for microfiber mechanical characterization do not translate directly to analysis of nanofibers.<sup>28-31</sup> One difficulty is that fiber alignment will influence tensile response. Alignment can be controlled and optically analyzed during fabrication of microfiber mats, but alignment control and analysis are more difficult for nanofiber media. Some approaches, for example, use rotating or conductive collectors can enable some control over nanofiber alignment.<sup>32,33</sup> Nanofiber structure is also influenced by details of the solution preparation process which can also change the fiber mechanical strength.<sup>34</sup>

For this study, mechanical tensile testing of the fiber mats was done using an Instron 5943 Tensile tester equipped with a 10 N load cell and pneumatic grips. The crosshead speed was set to 10 mm/min. The gauge length was 2.5 cm. The nylon mats were loaded onto the grips, the sides of the cardstock frame were cut and then mats were measured under strain until failure.

All electrospun samples were prepared using similar solutions and similar electrospinning conditions to ensure minimal sample-to-sample variation in nanofiber structure and fiber alignment. The collected tensile data is normalized to the mass of the starting fiber mat.

## 6.3 Results

### 6.3.1 Nanofiber Morphology

Figure 6.4 shows SEM images of nanofiber mats used in this study. The uncoated nanofibers in panel (a) are approximately  $200 \pm 40$  nm in diameter, with several smaller nanofibrils dispersed through the fiber network.<sup>34</sup> Panels (b)-(e) are SEM images of nanofiber mats coated with 100 cycles of aluminum oxide, zinc oxide,  $\text{TiO}_2$  from  $\text{TiCl}_4/\text{H}_2\text{O}$ , and  $\text{TiO}_2$  from  $\text{TIP}/\text{H}_2\text{O}$ , respectively. After coating, the nanofibrils are most apparent in the SEM images for samples coated with aluminum oxide or  $\text{TiCl}_4/\text{H}_2\text{O}$  (panels b and d). Flat silicon wafers coated in the same deposition run showed thickness of  $11.8 \pm 0.02$  nm,  $10 \pm 1$  nm,  $6.6 \pm 0.2$  nm, and  $3.7 \pm 0.08$  nm for the fibers coated with aluminum oxide, zinc oxide, and titanium dioxide using  $\text{TiCl}_4/\text{H}_2\text{O}$  and  $\text{TIP}/\text{H}_2\text{O}$  respectively as shown in Figure 6.3. The nanofibril network appears damaged in the SEM micrographs of the bare nanofibers and the fibers coated with zinc oxide and  $\text{TIP}/\text{H}_2\text{O}$ . This damage could be due to the metal sputter coating used before SEM imaging. The aluminum oxide and  $\text{TiCl}_4/\text{H}_2\text{O}$  coatings seem to help minimize nanofibril breakage. The ALD films did not alter the nanofiber morphology. Previous studies of  $\text{Al}_2\text{O}_3$  ALD onto nylon nanofibers showed distinct morphology change after TMA/ $\text{H}_2\text{O}$  exposure which was ascribed to infiltration and reaction between the TMA and the carbonyl groups present in the nylon.<sup>18,22</sup> Any reaction between nylon and the titanium precursors studied here appears to be less vigorous than the TMA/nylon interaction.

We also used TEM to image the cross section of the uncoated and coated samples, and Figure 6.5 shows the results. The uncoated nylon nanofiber cross sections are shown in

Figure 6.5 panels (a) and (b). The polymer fiber shows minimal TEM contrast with the surrounding epoxy. Figures 6.5 (c) and (d) show similar fibers coated with TiO<sub>2</sub> from TiCl<sub>4</sub>/H<sub>2</sub>O, and Figures 6.5 (e) and (f) show fibers coated using TIP/H<sub>2</sub>O. The nanofibers coated with TiCl<sub>4</sub>/H<sub>2</sub>O have a very distinct and uniform coating that is approximately  $19 \pm 3$  nm thick, consistent with the growth rate on the planar silicon. Contrast gradients around the edges of some fibers arise from fibers that are not perfectly perpendicular for a cross section. The coating on the nanofibers treated with TIP/H<sub>2</sub>O is not uniform on the nanofibers, and the film thickness is more difficult to discern. We estimate it is  $\sim 4 \pm 1$  nm, which is considerably less than the  $\sim 11$  nm measured on silicon under the same conditions. The different growth rate on the oxidized silicon and nylon surfaces using TIP is consistent with less TIP adsorption on the polymer surface leading to overall slower TiO<sub>2</sub> nucleation. Similar TEM studies have been done for aluminum oxide coated nylon fibers<sup>36</sup>.

### 6.3.2 FTIR

The FTIR data in Figure 6.6 allows us to look closely at how the nylon nanofibers react with the two TiO<sub>2</sub> precursors. Each plot shows spectra for the untreated nylon nanofibers (bottom-most spectrum in each panel) as well as difference spectra after ALD coating. Each difference spectrum is the absorbance of the fibers after a process step minus the absorbance before the step (i.e. after the previous step). The difference spectra highlight the change in bonding structure upon ALD coating. Figure 6.6(a) and (b) show results on the same absorbance scale, after coating the nylon nanofibers with TiCl<sub>4</sub>/H<sub>2</sub>O and TIP/H<sub>2</sub>O respectively. The changes with the TIP precursor are much smaller than with the TiCl<sub>4</sub> vapor. To more clearly view the changes, the same spectra are shown again in 6(c) and (d)

respectively, with a more expanded absorbance scale for the difference spectra. The spectra of the untreated nylon show a characteristic hydrogen-bonded NH stretching mode at  $\sim 3300\text{ cm}^{-1}$ , the  $\text{CH}_2$  asymmetric and symmetric stretching peaks at  $2931\text{ cm}^{-1}$  and  $2860\text{ cm}^{-1}$  respectively. The amide I peak is at  $\sim 1645\text{ cm}^{-1}$ , the amide II (N-H bend/C-N stretch) is at  $\sim 1542\text{ cm}^{-1}$ , and the amide III (N-C=O) and  $\text{CH}_2$  wagging peaks are at  $\sim 1369\text{ cm}^{-1}$  and  $1201\text{ cm}^{-1}$ , respectively. The spectra in panel (a) corresponding to deposition using  $\text{TiCl}_4$  show relatively large features at  $530$  and  $\sim 810\text{ cm}^{-1}$  which are ascribed to the stretching modes of the amorphous  $\text{TiO}_2$ . The spectra corresponding to TIP ALD show much smaller  $\text{TiO}_2$  related features. Even so, the expanded spectra in 6(d) show that  $\text{TiO}_2$  is present after coating with TIP/ $\text{H}_2\text{O}$ . For both deposition precursors, the amide peaks near  $1400\text{-}1800\text{ cm}^{-1}$  and the NH stretching peaks near  $3300\text{ cm}^{-1}$  were affected by 100 ALD cycles, but the  $\text{TiCl}_4/\text{H}_2\text{O}$  reaction produced a much larger change compared to 100 cycles of TIP/ $\text{H}_2\text{O}$ . FTIR has been widely used to analyze the interaction of TMA with nylon<sup>35-37</sup>. Qualitatively, the change in spectral response after  $\text{TiCl}_4/\text{H}_2\text{O}$  appears similar to the change after TMA/ $\text{H}_2\text{O}$ , where the TMA reacted with carbonyl and N-H groups present in nylon.<sup>35-37</sup> An important difference is that the titanium precursors react less vigorously and to a lesser extent with the nylon than does TMA under similar conditions. This is due to TMA being a stronger Lewis acid than the titanium precursors.

### 6.3.3 X-ray Photoelectron Spectroscopy

We also used XPS to analyze the chemical composition of the fibers and fiber surfaces. Figure 6.7(a) shows XPS survey scans for the untreated nylon fibers and fibers coated with 100 cycles of either  $\text{TiCl}_4/\text{H}_2\text{O}$  or TIP/ $\text{H}_2\text{O}$  at  $50^\circ\text{C}$ . The nylon fibers show

features due to oxygen, nitrogen, and carbon. Figures 6.7(b) and (c) show the atomic fraction estimated from the XPS data for a series of samples coated with TiO<sub>2</sub> using: (b) TiCl<sub>4</sub>/H<sub>2</sub>O; (c) TIP/H<sub>2</sub>O. The untreated nylon shows predominantly carbon. Titanium is present on the all of the ALD coated fibers, with a trace of chlorine from TiCl<sub>4</sub>/H<sub>2</sub>O. After 100 ALD cycles, the nitrogen signal is near the XPS sensitivity limit (~0.5%) for the nylon coated using TiCl<sub>4</sub>/H<sub>2</sub>O, whereas N is readily observed after coating with TIP/H<sub>2</sub>O. This indicates that after 100 cycles the TiCl<sub>4</sub>/H<sub>2</sub>O coated samples have a TiO<sub>2</sub> film thick enough so that the XPS cannot detect the nitrogen signal from the underlying polymer, whereas it requires more than 200 cycles for the TIP/H<sub>2</sub>O treated fibers to mask the nitrogen signal. After 200 cycles (TiCl<sub>4</sub>/H<sub>2</sub>O) and 400 cycles (TIP/H<sub>2</sub>O), both samples show Ti, O and C, consistent with TiO<sub>2</sub> (along with surface adventitious carbon). The transition from C to Ti/O in the XPS spectra occurs over ~50 cycles using TiCl<sub>4</sub>/H<sub>2</sub>O, but it takes more than 100 cycles to achieve a fully coated Ti/O film using TIP/H<sub>2</sub>O. This is consistent with the IR results showing more coating using TiCl<sub>4</sub>/H<sub>2</sub>O compared to TIP/H<sub>2</sub>O ALD.

### 6.3.4 Mechanical Response

To analyze the effect of ALD on the mechanical response of nylon nanofibers, we produced samples with various numbers of ALD cycles at 105°C for each precursor and at 50°C for the titania coated samples. Each run contained at least 4 fiber samples for analysis. Some runs were repeated and results from both sets of samples were analyzed and recorded. Stress versus strain curves from one representative sample coated at 105°C are plotted in Figure 6.8 (a) and (b) for TiCl<sub>4</sub>/H<sub>2</sub>O and TIP/H<sub>2</sub>O coatings, respectively. Figures 6.8 (c) and (d) show results from similar nylon nanofibers coated with Al<sub>2</sub>O<sub>3</sub> and ZnO ALD. The stress

is normalized to the mass of the starting fiber sample. Considering the data in Figure 6.8(a) the untreated sample stretches with applied strain, until sample failure at ~24 % strain. The slope of the stress vs. strain curve analyzed at low applied strain is the Young's modulus, and is discussed below. As the nylon is coated with  $\text{TiCl}_4/\text{H}_2\text{O}$ , the point of ultimate strain decreases, so that after ~50 cycles, the material is very brittle, consistent with a ceramic coating on the nylon fiber. For the sample coated using  $\text{TIP}/\text{H}_2\text{O}$  (Figure 6.8b), the ultimate strain also decreases with increasing film thickness, but the transition is less severe. After 200 cycles the sample can still withstand a strain of more than 15%. Considering the samples coated with  $\text{Al}_2\text{O}_3$  and  $\text{ZnO}$ , the  $\text{Al}_2\text{O}_3$  coating shows trends similar to those of  $\text{TiCl}_4/\text{H}_2\text{O}$ , with a large decrease in maximum strain with increasing ALD coating thickness. The  $\text{ZnO}$  coating behaves more like the  $\text{TIP}/\text{H}_2\text{O}$  process with less change upon coating. Some samples show an increase in maximum tensile strain after  $\text{ZnO}$  ALD coating, but these samples are within error.

Analysis of the stress vs. strain plots allows us to determine the tensile strength, ultimate strain, and Young's modulus normalized by sample mass. To determine these values, we collected stress-strain results from at least 5 samples prepared under the same conditions and determined the average tensile strength, ultimate strain, and Young's modulus at each treatment condition. Samples that demonstrated irregular behavior during testing, such as slippage or breakage due to defects in the sample were not included in analysis. The resulting values are plotted versus the number of ALD cycles in Figure 6.9. Generally, the tensile strength of the fibers (maximum stress achieved on the stress-strain curve, data not shown) was not significantly impacted by the ALD coatings. Figure 6.9 (a) shows that the

ultimate strain (strain at failure) decreases with increasing ALD cycles, most markedly for the  $\text{TiCl}_4/\text{H}_2\text{O}$  and  $\text{Al}_2\text{O}_3$  coated samples. This means that the  $\text{TIP}/\text{H}_2\text{O}$  samples retained more elasticity after ALD treatment. Figure 6.9(b) shows the Young's Modulus of the ALD treated nylon nanofibers. The modulus increased upon coating with  $\text{TiCl}_4/\text{H}_2\text{O}$ , but it was not significantly altered by the  $\text{TIP}/\text{H}_2\text{O}$  ALD processes. From Figure 6.3, we see that the growth rate of  $\text{TiCl}_4$  is approximately twice that of  $\text{TIP}$ . Taking that difference into account when looking at Figure 6.9, we see that even with similar film thicknesses the ultimate strain for the  $\text{TiCl}_4$  treated samples is much lower and the modulus much higher than the  $\text{TIP}$  treated samples. Also as shown in Figure 6.9, the trends in mechanical response were largely unchanged when the  $\text{TiCl}_4/\text{H}_2\text{O}$  or  $\text{TIP}/\text{H}_2\text{O}$  process temperature was changed from 105 to 50°C. The glass transition temperature,  $T_g$ , for nylon 6 is ~ 52-54°C, making the deposition temperature close to or greater than  $T_g$ .<sup>38</sup> It should be noted that the modulus for the heat treated control samples was  $23 \pm 1$  MPa/mg. This value is within error to the  $20 \pm 4$  MPa/mg measured for the room temperature control samples, indicating that the elevated temperature had little effect on the mechanical behaviors of the samples. For comparison, we also treated some nylon nanofibers with  $\text{Al}_2\text{O}_3$  or  $\text{ZnO}$  ALD at 105°C and compared the mechanical response of those fiber mats to that of the titania coated samples. Figure 6.9 shows that the  $\text{Al}_2\text{O}_3$  process using TMA and  $\text{H}_2\text{O}$  led to changes similar to the  $\text{TiCl}_4/\text{H}_2\text{O}$  process, with the samples having mechanical properties more similar to an inorganic material. The  $\text{ZnO}$  process using DEZ and  $\text{H}_2\text{O}$  produced changes more similar to the  $\text{TIP}/\text{H}_2\text{O}$  treated samples and retained mechanical properties similar to the uncoated material.

## 6.4 Discussion

We find that TiO<sub>2</sub> ALD onto nylon nanofiber mats can distinctly alter the mat's response to applied force, but the extent of mechanical change depends strongly on the nature of the titanium precursor used. The XPS data confirmed that titanium dioxide was growing on the nylon using both precursors. However, the in-situ FTIR data in Figure 6.6 show a much larger change in the amide I and amide II modes after TiCl<sub>4</sub>/H<sub>2</sub>O compared to the change after the same TIP/H<sub>2</sub>O exposure, indicating that compared to the TIP, the TiCl<sub>4</sub> is more able to diffuse and react in the nylon bulk than the TIP. Similar in-situ FTIR analysis has been used to quantify the extent of reaction between trimethylaluminum and various polymer materials.<sup>37</sup>

The different extent of reaction for the two Ti precursors examined can be understood based on the expected chemical reactivity of these species. TiCl<sub>4</sub> is a strong Lewis acid, so it can react with nucleophilic carbonyl groups in the nylon to form titanium-oxygen-alkyl linkages.<sup>39,40</sup> The high reactivity for the TiCl<sub>4</sub> is consistent with the IR data showing that the TiCl<sub>4</sub>/H<sub>2</sub>O exposure strongly modifies the amide I and amide II modes near 1645 and 1543 cm<sup>-1</sup> associated with carbonyl Lewis base sites.<sup>37</sup> Furthermore, HCl is an important byproduct of the TiCl<sub>4</sub>/H<sub>2</sub>O reaction. HCl could insert into the nylon polymer chains leading to chain scission. When the polymer chain is altered or severed, the relatively small TiCl<sub>4</sub> precursor can diffuse more easily into the polymer bulk, further enhancing the extent of TiCl<sub>4</sub> reaction. In turn, the higher reactivity for the TiCl<sub>4</sub> relative to TIP will produce a relatively large change in the mechanical strength and elasticity of the fibers, which is evident in the

measured mechanical response. Significant subsurface diffusion of TMA during ALD on nylon has been documented by several previous reports.<sup>18,22,37</sup> As a weaker Lewis acid, TIP will take longer to nucleate on the fiber surface compared to  $\text{TiCl}_4$ , but it will ultimately lead to a more uniform coating without much chemical modification or mechanical change in the bulk fiber, consistent with the mechanical results. As the coating grows and begins to fully coat the fiber, any precursor diffusion will be impeded, further promoting conformal surface growth.

Based on these observations, we conclude therefore that the differences in the mechanical properties after  $\text{TiO}_2$  coating with  $\text{TiCl}_4$  and TIP are due to the very different extent of chemical interactions between the precursors and the nylon during the initial stages of ALD. Sinha et al.<sup>40</sup> studied the diffusion of  $\text{TiCl}_4$  and TIP into PMMA polymer films, and they concluded that  $\text{TiCl}_4$  more readily diffuses through the PMMA than does TIP, and that the TIP reacts with the polymer to form a film that alters the precursor transport properties. They also noted that the reaction between PMMA and  $\text{TiCl}_4$  could lead to chain crosslinking since titanium has six coordination sites, which would decrease the mobility of the polymer chains. We note that nylon crosslinking will also decrease the elasticity of the fibers, consistent with the increase in Young's modulus after ALD using  $\text{TiCl}_4$  shown in Figure 6.9b.

The changes in mechanical properties after TMA/ $\text{H}_2\text{O}$  and DEZ/ $\text{H}_2\text{O}$  are also consistent with different precursor/nylon extent of reaction. Since the TMA is a strong Lewis acid, it will react more readily with the Lewis base sites in nylon 6 (i.e. carbonyl

groups), leading to more extensive modifications of the bulk chemical properties and mechanical response of the coated fibers, similar to  $\text{TiCl}_4$ . Similarly, DEZ is a weaker Lewis acid compared to TMA and  $\text{TiCl}_4$ , leading it to have less impact on the mechanical properties of nylon. The difference in reactivity may also be in part due to steric hindrance effects. The smaller size of the TMA and  $\text{TiCl}_4$  molecules will facilitate the formation of the Lewis adduct compared to DEZ and TIP. The mechanical properties seen in the bulk mats might explain the prominence of the nanofibrils in the SEM images of the aluminum oxide and  $\text{TiCl}_4/\text{H}_2\text{O}$  coated fibers. These coatings might reinforce the nanofibrils, preventing breakage during sputtering.

## 6.5 Conclusion

We demonstrated that the mechanical properties of nylon 6 nanofiber mats change after exposing the fibers to ALD using titanium isopropoxide or titanium tetrachloride precursors. The tensile strength of the fibers was mostly unchanged by the ALD process, but the Young's modulus increased and ultimate strain markedly decreased after exposure to ~50 cycles of  $\text{TiCl}_4/\text{H}_2\text{O}$  at 50 and 105°C. Similar treatments with  $\text{TIP}/\text{H}_2\text{O}$  produced less overall chemical change, and had less of an effect on the mechanical properties. We conclude that the  $\text{TiCl}_4/\text{H}_2\text{O}$  process tends to add  $\text{TiO}_2$  in the form of particles within the fiber itself which coalesce into a film, whereas the  $\text{TIP}/\text{H}_2\text{O}$  adds  $\text{TiO}_2$  as a film on the outer surface of the fiber. Because of the larger extent of subsurface interaction for the  $\text{TiCl}_4$  vs the TIP, similar amounts of  $\text{TiO}_2$  from  $\text{TiCl}_4$  produce much larger changes in mechanical response compared to  $\text{TiO}_2$  from TIP. Moreover, we note that generally the precursor/bulk polymer interaction

tends to degrade mechanical strength and elasticity of the nylon nanofibers. Overall results show that precursor-substrate interactions during ALD coating can have a large impact on the mechanical properties of polymer fiber materials.

### **Acknowledgments**

This work was supported by the Defense Threat Reduction Agency (DTRA) contract number HDTRA1-07-C-0058. Any opinions, findings and conclusions or recommendations expressed in this material are those of the author(s) and do not necessarily reflect the views of DTRA. We are thankful to the Analytical Instrumentation Facility at North Carolina State University, specifically Fred Stevie for the XPS data, Roberto Garcia for the TEM images, and Chuck Mooney for the SEM images.

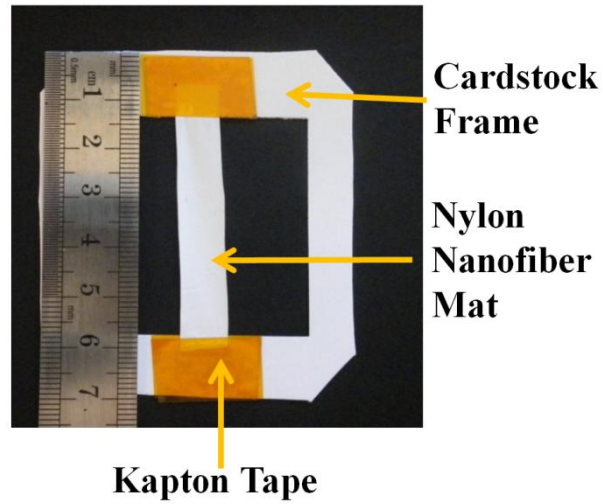


**Figure 6.1:** Example of an uncoated nylon nanofiber sample mounted on a cardstock frame using double sided Kapton tape prior to stress-strain testing.

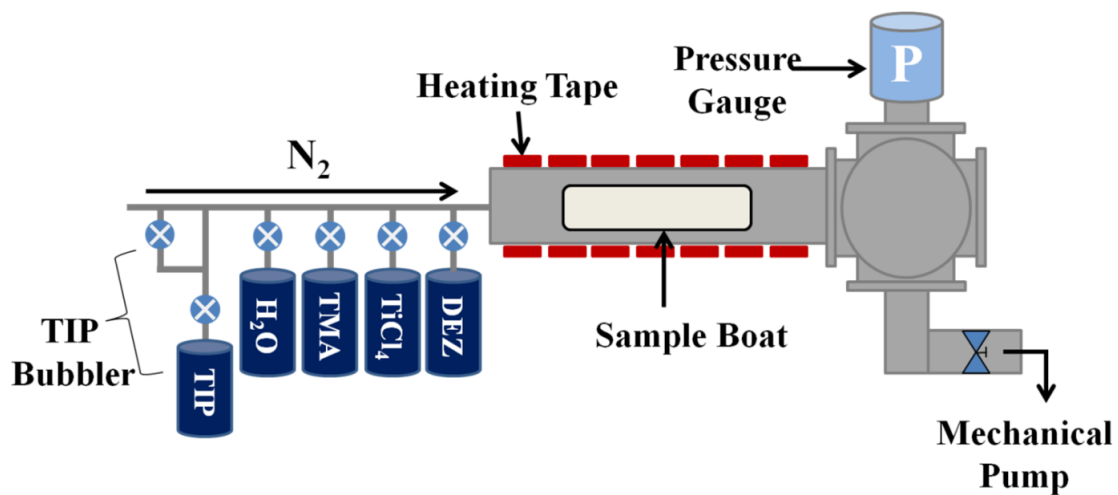


**Figure 6.2:** Schematic of the home built hot-wall viscous flow reactor used to coat the nylon nanofibers.

**Table 6.1:** Dosing and purging times used to coat the nylon nanofibers samples for aluminum oxide, zinc oxide, and titanium dioxide coatings.

Precursor	Precursor Dose		N <sub>2</sub> Purge	Water Dose	N <sub>2</sub> Purge
TMA	0.1 s		45 s	0.1 s	30 s
DEZ	0.2 s		45 s	0.2 s	30 s
TiCl <sub>4</sub>	0.1 s		30 s	0.1 s	30 s
TIP	Prep - 2s	Dose - 0.5 s	30 s	0.1 s	30 s

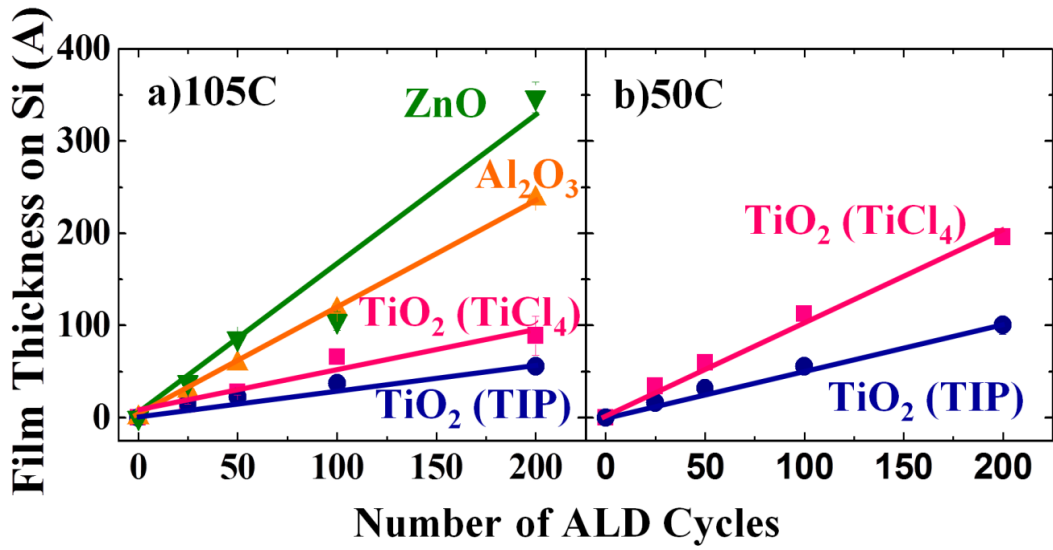


**Figure 6.3:** Film thickness vs. ALD cycle number for the silicon wafer monitors coated at a deposition temperature of (a) 105 °C and (b) 50 °C. The wafers were placed in the reactor while the nanofibers were being coated to monitor film growth.

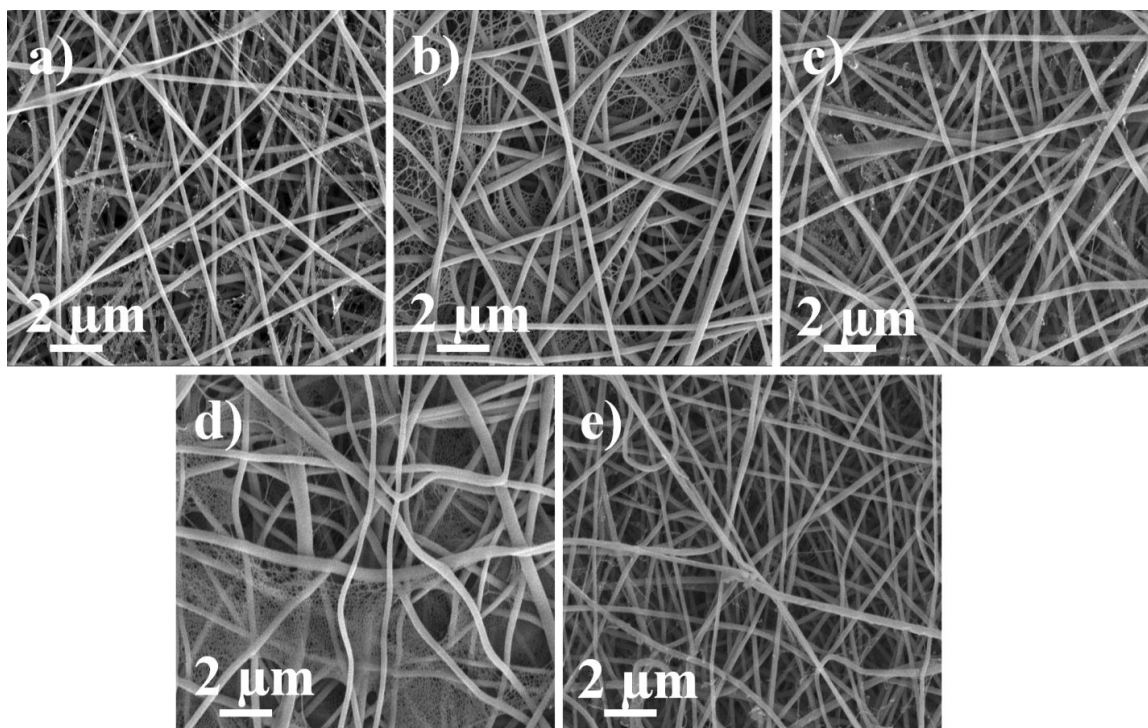


**Figure 6.4:** Representative SEM images showing the morphology of (a) uncoated nylon nanofibers, approximately 200 nm in diameter with smaller nanofibrils dispersed throughout the mat. The morphology of the nanofibers was not changed after coating with either 100 cycles of (b) Al<sub>2</sub>O<sub>3</sub>, (c) ZnO, (d) TiO<sub>2</sub> using TiCl<sub>4</sub>/H<sub>2</sub>O or (e) TiO<sub>2</sub> using TIP/H<sub>2</sub>O. The nanofibrils are more apparent after Al<sub>2</sub>O<sub>3</sub> and TiO<sub>2</sub> via TiCl<sub>4</sub>/H<sub>2</sub>O.

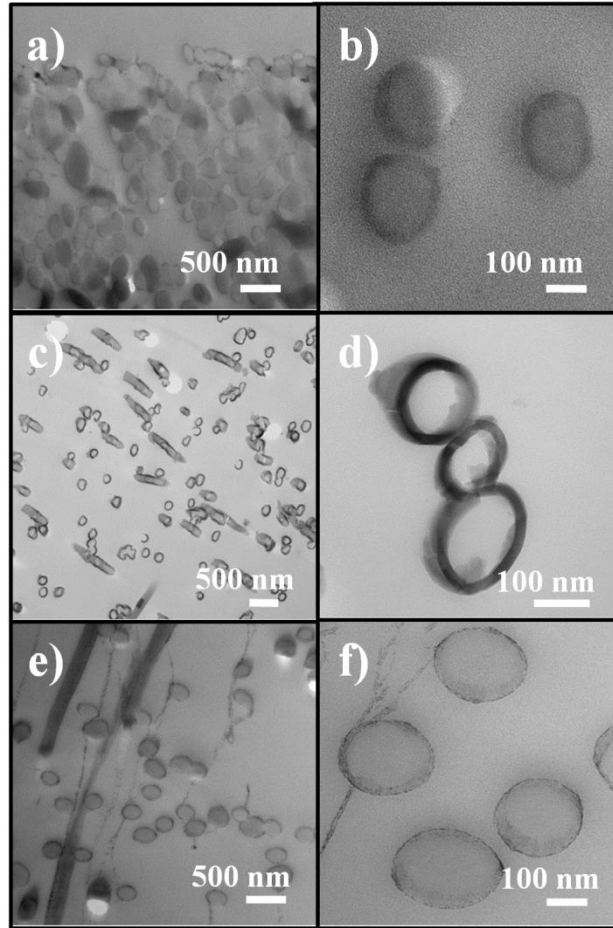


**Figure 6.5:** Cross-sectional TEM images of nylon nanofibers that were (a-b) uncoated, (c-d) coated using 200 cycles of  $\text{TiCl}_4/\text{H}_2\text{O}$  and (e-f) coated using 200 cycles of  $\text{TIP}/\text{H}_2\text{O}$ . All coatings were performed at  $50^\circ\text{C}$ . The uncoated nanofibers show little TEM contrast relative to the epoxy, whereas there is a clearly defined shell around the titania coated nanofibers. The film is very uniform on the  $\text{TiCl}_4/\text{H}_2\text{O}$  coated fibers, but coating is thinner and less well-defined for the  $\text{TIP}/\text{H}_2\text{O}$  process.

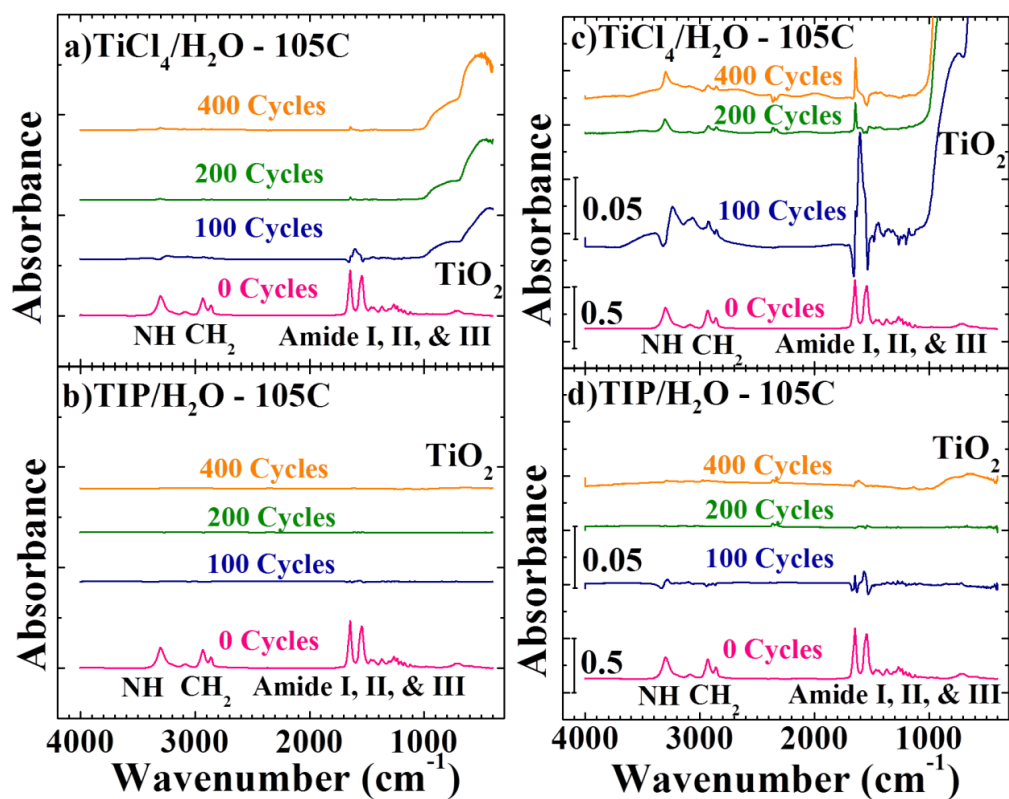


**Figure 6.6:** FTIR difference spectra of the titanium dioxide coated nylon nanofibers for coating using (a), (c) TiCl<sub>4</sub>/H<sub>2</sub>O and (b), (d) TIP/H<sub>2</sub>O. Spectra in (a) show TiO<sub>2</sub> modes after ~100 TiCl<sub>4</sub>/H<sub>2</sub>O cycles, whereas spectra in (b) show minimal TiO<sub>2</sub> features after 400 cycles of TIP/H<sub>2</sub>O. Under a more magnified absorbance scale in (c) and (d), TiO<sub>2</sub> features become apparent for TIP/H<sub>2</sub>O samples.

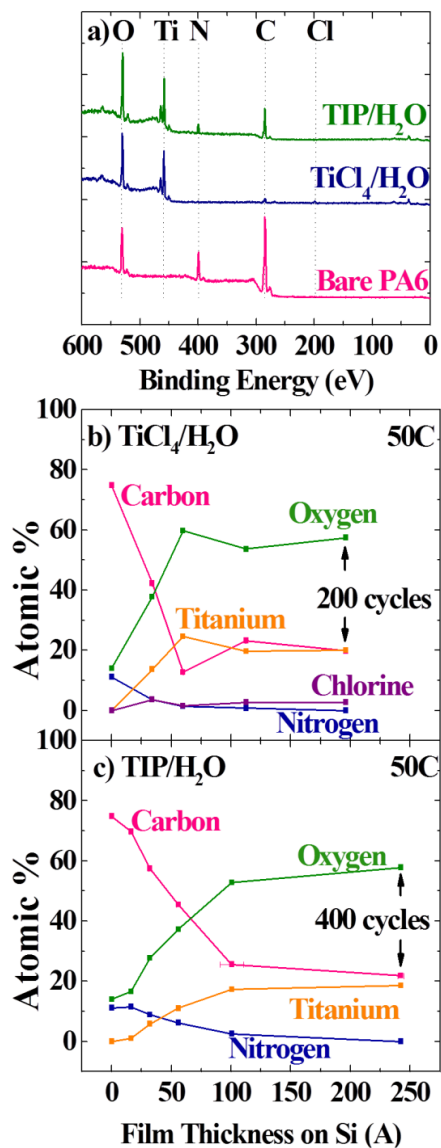


**Figure 6.7:** (a) The XPS survey scan for uncoated nylon shows oxygen, nitrogen and carbon signals. After 100 cycles of TiCl<sub>4</sub>/H<sub>2</sub>O, only trace amount of nitrogen are detected, whereas a nitrogen peak is still visible for the TIP/H<sub>2</sub>O sample. Figures (b) and (c) show the atomic percentages based on film thickness for titanium and oxygen for TiCl<sub>4</sub>/H<sub>2</sub>O and TIP/H<sub>2</sub>O samples, respectively.

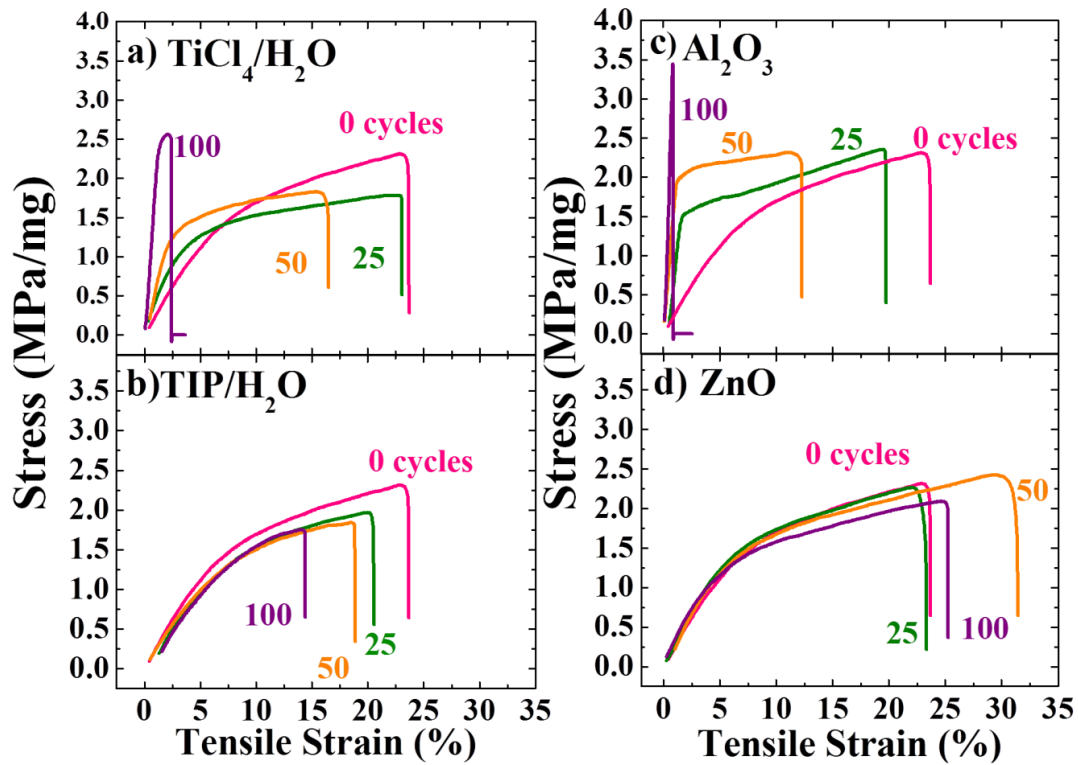


**Figure 6.8:** Stress-strain data from one representative nylon nanofiber sample coated with titanium dioxide using (a)  $\text{TiCl}_4/\text{H}_2\text{O}$ , (b)  $\text{TIP}/\text{H}_2\text{O}$ , (c) aluminum oxide, and (d) zinc oxide. The initial slope of the stress-strain curves increase with increasing cycle numbers for the samples coated with either (a)  $\text{TiCl}_4/\text{H}_2\text{O}$  or (c) aluminum oxide, indicating more ceramic behavior. The (b)  $\text{TIP}/\text{H}_2\text{O}$  and (d) zinc oxide coated samples show properties similar to the uncoated nylon nanofibers even at higher cycle number.

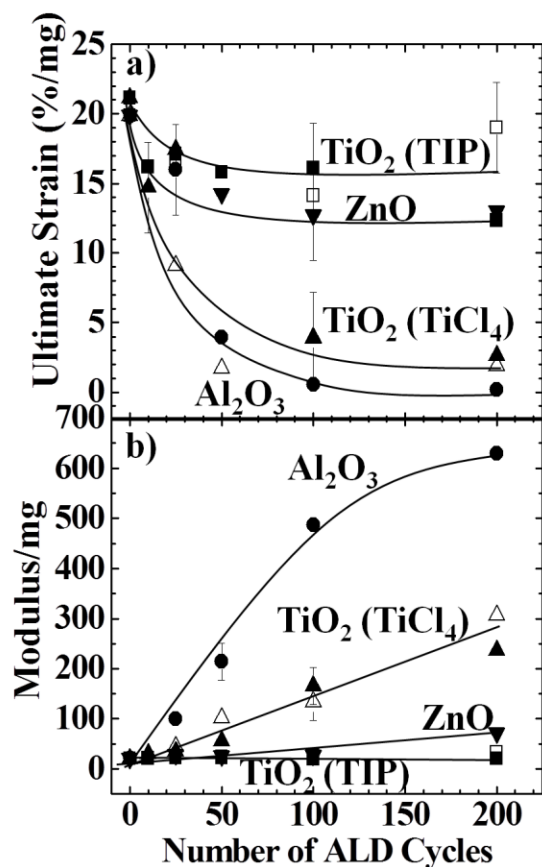


**Figure 6.9:** The (a) ultimate strain and (b) Young's Modulus versus cycle number for nylon nanofibers coated with TiCl<sub>4</sub>/H<sub>2</sub>O and TIP/H<sub>2</sub>O ALD at 105°C (solid symbols) and 50°C (open symbols), as well as results from nylon coated with ALD Al<sub>2</sub>O<sub>3</sub> and ZnO at 105°C. As the number of ALD cycles increases, the ultimate strain decreases and Young's Modulus increases for the aluminum oxide and TiCl<sub>4</sub>/H<sub>2</sub>O coated samples, consistent with increased brittleness. The TIP/H<sub>2</sub>O and zinc oxide samples show trends similar to the uncoated nylon nanofibers.

## References

- (1) Z.-M. Huang, Y.-Z. Zhang, M. Kotaki, and S. Ramakrishna, *Compos. Sci. Technol.* **63**, 2223 (2003).
- (2) D. H. Reneker, A. L. Yarin, E. Zussman, and H. Xu, *Adv. Appl. Mech.* **41**, 43 (2007).
- (3) J. S. Jeong, S. Y. Jeon, T. Y. Lee, J. H. Park, J. H. Shin, P. S. Alegaonkar, A. S. Berdinsky, and J. B. Yoo, *Diam. Relat. Mater.* **15**, 1839 (2006).
- (4) M. B. Bazbouz, and G. K. Stylios, *J. Polym. Sci. Pol. Phys.* **48**, 1719 (2010).
- (5) W. K. Son, J. H. Youk, and W. H. Park, *Carbohydr. Polym.* **65**, 430 (2006).
- (6) D. Li, Y. Wang, and Y. Xia, *Nano Lett.* **3**, 1167 (2003).
- (7) H. S. Yoo, T. G. Kim, and T. G. Park, *Adv. Drug Deliv. Rev.* **61**, 1033 (2009).
- (8) F. Chen, C. Lee, and S. Teoh, *Mater. Sci. Eng, C.* **27**, 325 (2007).
- (9) J. H. Park, B. S. Kim, Y. C. Yoo, M. S. Khil, and H. Y. Kim, *J. Appl. Polym. Sci.* **107**, 2211 (2008).
- (10) J. Zeng, A. Aigner, F. Czubayko, T. Kissel, J. H. Wendorff, and A. Greiner, *Biomacromolecules* **6**, 1484 (2005).
- (11) A. Wróbel, M. Kryszewski, W. Rakowski, M. Okoniewski, and Z. Kubacki, *Polymer* **19**, 908 (1978).
- (12) Q. Wei, Y. Liu, D. Hou, and F. Huang, *J. Mater. Process. Tech.* **194**, 89 (2007).
- (13) D. Pappas, A. Bujanda, J. D. Demaree, J. K. Hirvonen, W. Kosik, R. Jensen, and S. McKnight, *Surf. Coat. Technol.* **201**, 4384 (2006).
- (14) M. Ma, Y. Mao, M. Gupta, K. K. Gleason, and G. C. Rutledge, *Macromolecules* **38**, 9742 (2005).

- (15) N. I. Baklanova, T. M. Zima, A. I. Boronin, S. V. Kosheev, A. T. Titov, N. V. Isaeva, D. V. Grashenkov, and S. S. Solntsev, *Surf. Coat. Technol.* **201**, 2313 (2006).
- (16) S.-M. Lee, E. Pippel, U. Gosele, C. Dresbach, Y. Qin, C. V. Chandran, T. Brauniger, G. Hause, and M. Knez, *Science* **324**, 488 (2009).
- (17) Q. Peng, X.-Y. Sun, J. C. Spagnola, G. K. Hyde, R. J. Spontak, and G. N. Parsons, *Nano Lett.* **7**, 719 (2007).
- (18) C. J. Oldham, B. Gong, J. C. Spagnola, J. S. Jur, K. J. Senecal, T. A. Godfrey, and G. N. Parsons, *J. Electrochem. Soc.* **158**, D549 (2011).
- (19) E. Santala, M. Kemell, M. Leskelä, and M. Ritala, *Nanotechnology* **20**, 035602 (2009).
- (20) G. K. Hyde, G. Scarel, J. C. Spagnola, Q. Peng, K. Lee, B. Gong, K. G. Roberts, K. M. Roth, C. A. Hanson, C. K. Devine, S. M. Stewart, D. Hojo, J.-S. Na, J. S. Jur, and G. N. Parsons, *Langmuir* **26**, 2550 (2010).
- (21) W.-S. Kim, B.-S. Lee, D.-H. Kim, H.-C. Kim, W.-R. Yu, and S.-H. Hong, *Nanotechnology* **21**, 245605 (2010).
- (22) J. C. Spagnola, B. Gong, S. A. Arvidson, J. S. Jur, S. A. Khan, and G. N. Parsons, *J. Mater. Chem.* **20**, 4213 9 (2010).
- (23) J. S. Jur, W. J. Sweet, C. J. Oldham, and G. N. Parsons, *Adv. Func. Mater.* **21**, 1993 (2011).
- (24) M. Ritala, M. Leskela, L. Niinisto, and P. Haussalo, *Chem. Mater.* **5**, 1174 (1993).
- (25) M. Ritala, M. Leskelä, E. Nykänen, P. Soininen, and L. Niinistö, *Thin Solid Films* **225**, 288 (1993).
- (26) J. Aarik, A. Aidla, H. Mändar, and T. Uustare, *Appl. Surf. Sci.* **172**, 148 (2001).

- (27) Q. Xie, J. Musschoot, D. Deduytsche, R. L. Van Meirhaeghe, C. Detavernier, S. Van den Berghe, Y.-L. Jiang, G.-P. Ru, B.-Z. Li, and X.-P. Qu, *J. Electrochem. Soc.* **155**, H688 (2008).
- (28) E. P. S. Tan, S. Y. Ng, and C. T. Lim, *Biomaterials* **26**, 1453 (2005).
- (29) S.-C. Wong, A. Baji, and S. Leng, *Polymer* **49**, 4713 (2008).
- (30) R. Inai, M. Kotaki, and S. Ramakrishna, *Nanotechnology* **16**, 208 (2005).
- (31) E. P. S. Tan, and C. T. Lim, *Nanotechnology* **17**, 2649 (2006).
- (32) P. Kiselev, and J. Rosell-Llompart, *J. Appl. Polym. Sci.* **125**, 2433 (2012).
- (33) M. Khamforoush, and M. Mahjob, *Mater. Lett.* **65**, 453 (2011).
- (34) H. R. Pant, K.-T. Nam, H.-J. Oh, G. Panthi, H.-D. Kim, B. Kim, and H. Y. Kim, *J. Colloid Interf. Sci.* **364**, 107 (2011).
- (35) C. J. Oldham, B. Gong, J. C. Spagnola, J. S. Jur, K. J. Senecal, T. A. Godfrey, and G. N. Parsons, *J. Electrochem. Soc.* **158**, D549 (2011).
- (36) J. C. Spagnola, B. Gong, S. A. Arvidson, J. S. Jur, S. A. Khan, and G. N. Parsons, *J. Mater. Chem.* **20**, 4213 (2010).
- (37) B. Gong, and G. N. Parsons, *J. Mater. Chem.* **22**, 15672 (2012).
- (38) J. Brandrup, E. H. Immergut, E. A. Grulke, A. Abe, and D. R. Bloch, *Polymer Handbook*, 4<sup>th</sup> ed. (John Wiley & Sons, 1999; 2005), pp. VI/235.
- (39) B. Gong, Q. Peng, J. S. Jur, C. K. Devine, K. Lee, and G. N. Parsons, *Chem. Mater.* **23**, 3476 (2011).
- (40) A. Sinha, D. W. Hess, and C. L. Henderson, *J. Vac. Sci. Technol. B* **25**, 1721 (2007).

## **Chapter 7. Determination of Elastic Modulus of Electrospun Nylon 6 Nanofibers Coated by Atomic Layer Deposition using AFM Nanoindentation**

### **Abstract**

Polymer nanofibers are widely used for filtration, tissue scaffolding, as catalyst supports, and as functional textiles. The deposition of thin films onto polymer nanofibers has been widely studied to add further functionality for chemical resistance, biocompatibility, and to alter wettability among others. The addition of thin films can impact the mechanical properties of the polymer materials. In this study, thin films were deposited onto electrospun nylon 6 nanofibers using atomic layer deposition (ALD). The nanofibers were coated with aluminum oxide and titanium dioxide. The elastic modulus of the nanofibers was measured by nanoindentation using an atomic force microscope. The modulus for the nanofibers increases with increasing film thickness in the case of aluminum oxide films and titanium dioxide thin films using titanium tetrachloride and water as precursors. The elastic modulus is unaffected by the deposition of titanium dioxide using titanium isopropoxide and water. The modulus on silicon is unchanged after deposition for all treatments except after 100 cycles of titanium tetrachloride and water after which the modulus increases. More data is required to determine the validity of this trend. Amplitude modulated frequency modulated AFM was also used to map the surface of a titanium tetrachloride/water coated nylon nanofiber cross-section. The images show the soft nanofibers encapsulated by stiff titania films with a sharp interface between the two materials. The AM-FM technique proves to be an excellent method of force mapping and can be a useful tool in analyzing thin films on nanofibers and the resulting morphology and stiffness.

## 7.1 Introduction

The emergence of electrospinning has allowed for the creation of polymer fibers with diameters on the nanoscale. Due to small fiber diameters, electrospun polymers mats have been used in filtration<sup>1, 2</sup>, tissue scaffolding<sup>3, 4</sup>, protein delivery<sup>5</sup>, sensing applications<sup>6, 7</sup>, and for functional textiles<sup>8-10</sup>. Further functionalization of the fibers can improve biocompatibility, chemical resistance, conductivity, and sensing capabilities among others. Common methods of functionalization include adding inorganic materials such as carbon nanotubes<sup>8</sup> or nanoparticles<sup>11</sup> into the polymer solution during electrospinning, wet chemical methods<sup>3, 4, 12</sup>, and vapor phase methods such as plasma treatments<sup>13, 14</sup> and chemical vapor deposition<sup>15</sup>. We focus on atomic layer deposition (ALD) as a facile vapor phase method of coating complex three dimensional networks.

Atomic layer deposition is a form of chemical vapor deposition that uses sequential, self-limiting reactions to deposit inorganic films with near monolayer control over thickness. It has been widely used in the semiconductor industry and has also been applied to polymer substrates for diffusion barriers<sup>16, 17</sup>, to alter wettability<sup>18, 19</sup> and for increased conductivity<sup>20</sup>. A benefit of ALD on fibrous substrates is that the precursors can diffuse throughout the fiber mat to deposit a uniform film on each fiber<sup>21-24</sup>.

The application and use of certain ALD precursors have been found to embrittle some fibers<sup>25</sup> while other studies have found ALD treatment to enhance mechanical properties<sup>26</sup>. It is desirable to further understand the chemical and physical interaction between ALD precursors and polymer substrates and how that interaction affects their mechanical performance. It can be complicated to measure the mechanical properties of nanofibers due

to the difficulty of fiber alignment in nanofiber mats.<sup>27, 28</sup> The directionality in reference to the applied load and the degree of alignment in nanofiber mats will alter the measured mechanical response. Additionally, it is difficult to obtain a single nanofiber for tensile testing<sup>29, 30</sup>. An alternative method is nanoindentation using atomic force microscopy (AFM) to measure the modulus of individual nanofibers<sup>31-33</sup>. Using this technique, we investigate the effect of ALD deposited thin films on the modulus of individual electrospun nanofibers. We also explore new techniques in atomic force microscopy, namely amplitude modulated frequency modulated (AM-FM) AFM, and how they can provide more insight into the stiffness and morphology of nanoscale materials.

## **7.2 Experimental**

### **7.2.1 Materials and Electrospinning**

Nylon nanofibers were electrospun using a solution of 20 wt % nylon (Ultramid B27 02 from BASF) in formic acid (88% Acros Organics, ACS Reagent). The solution was stirred in an oil bath at 60°C for approximately 2 hours until the nylon pellets had completely dissolved. A NESSE electrospinning unit described previously was used for electrospinning<sup>25</sup>. The electrospinning substrates were silicon wafers with native oxide present, attached by epoxy to AFM disks. The oxidized silicon wafer surface was cleaned using acetone and blown with house nitrogen before use to remove any particulates. The wafers and AFM disks were then mounted on a grounded collection plate covered with aluminum foil. The nylon nanofibers were then electrospun for ~60 seconds to achieve a sparse single layer of nanofibers.

### 7.2.2 Nanofiber Functionalization

The electrospun nylon fibers were functionalized using atomic layer deposition. The deposition was done in a hot-walled viscous flow reactor at 50°C with a deposition pressure of ~3 Torr. The fibers were coated with either aluminum oxide or titanium dioxide. The precursors used for aluminum oxide deposition were trimethyl aluminum (TMA, 98%) purchased from STREM chemicals and deionized water. For the titanium dioxide deposition, either titanium tetrachloride (TiCl<sub>4</sub>, Gelest, 99%) or titanium (IV) isopropoxide (TIP, Acros Organics, 98%) were used with deionized water. The samples were exposed to the metal containing precursor and then the reactor chamber was purged with nitrogen (99.999%) before being exposed to the deionized water. The aluminum oxide and TiCl<sub>4</sub>/H<sub>2</sub>O exposures were 0.1/45/0.1/30s corresponding to TMA or TiCl<sub>4</sub>/N<sub>2</sub>/H<sub>2</sub>O/N<sub>2</sub>. The TIP recipe included an extra step in which nitrogen was pulsed into the TIP bubbler to volatilize the vapor such that the TIP/H<sub>2</sub>O exposures were 2/0.5/30/0.1/30s corresponding to TIP prep/TIP/N<sub>2</sub>/H<sub>2</sub>O/N<sub>2</sub>.

### 7.2.3 Atomic Force Microscopy

Imaging and nanoindentation was done using a Cypher AFM from Asylum. The nanoindentation was done while in contact mode. Diamond coated AFM tips purchased from Nanoworld were used for indentation. The spring constant for the tips was determined using the Sader method<sup>34</sup>. IGOR software using the Hertz model was used to calculate the modulus from the force curves collected. Hertzian contact mechanics assumes that the materials are homogenous and isotropic and that there are no attractive forces such that adhesion is ignored. Additionally a contact radius,  $a$ , is smaller than the radius of the spherical indenter. The radius of contact can be described by

$$a^3 = \frac{3PR}{4E^*}$$

where P is the indenter load, R is the radius of the indenter, and E\* is the reduced modulus. The reduced modulus is a modulus that incorporates the modulus (E<sub>1</sub> and E<sub>2</sub>) and Poisson ratio (ν<sub>1</sub> and ν<sub>2</sub>) of the tip and substrate by

$$\frac{1}{E^*} = \left( \frac{1 - \nu_1^2}{E_1} + \frac{1 - \nu_2^2}{E_2} \right)$$

Published values<sup>35</sup> for the Poisson ratio for nylon are typically ~ 0.35. The indenter and silicon are expected to have ν ≈ 0.2. The modulus for the indenter was estimated to be 865 GPa with a radius of 81 nm. The tip property values were calibrated using nanoindentation on a quartz substrate with a known modulus (E = 69.6 GPa). The force curves were generally collected using a trigger point of 1V. The amplitude modulated frequency modulated (AM-FM) force mapping was done using an Asylum MFP-3D.

### 7.3 Results

Sample force curves for the silicon substrate and the nylon nanofibers are shown in Figure 7.1. As expected, the oxidized silicon substrate is much stiffer than the nylon nanofibers as demonstrated by the shapes of the force curves. The AFM tip experiences a much greater force from the silicon at shallower indents, whereas for the nylon, the tip can indent over 2 nm into the fiber before experiencing a similar resistance. Figure 7.2 shows several representative AFM images for the uncoated, titania coated, and alumina coated nanofiber samples. The nanofibers are approximately 200 ± 40 nm in diameter, as measured from a previous study described in Chapter 6 using the same electrospinning conditions. The

silicon substrates under the nanofibers are smooth even after 100 ALD cycles indicating uniform ALD growth. The white dots on the images in Figure 7.2 indicate where indentation occurred on the substrate or fiber, along with the corresponding value for the measured modulus. These values are summarized graphically in Figure 7.3. The uncoated nylon 6 fiber has a modulus of approximately  $2.0 \pm 0.5$  GPa, which is similar to values calculated using nanoindentation on injection molded nylon films<sup>35, 36</sup>. Bazbouz et al<sup>29</sup> measured the modulus of a single nanofiber to be 901.65 MPa using a tensile test, which is within a factor of  $\sim 2$  of the value we measured. However, measuring PA-6 fibers using an AFM bend test, Li et al.<sup>37</sup> found a much larger modulus of 30 GPa. Large differences in the modulus may occur due to variations in fiber diameter, crystallinity, water content, and details of the testing method. Other sources of error for AFM indentation include slippage on the curved fiber surface or adhesion between the tip and sample.

The modulus for the uncoated oxidized silicon surface is  $54 \pm 9$  GPa, which is close to 70 GPa measured for SiO<sub>2</sub> by Choi et al<sup>38</sup>, and less than  $\sim 198$  GPa measured for silicon without oxide by Wang et al.<sup>39</sup> After performing 100 ALD cycles at 50°C, the modulus for the nylon nanofibers increases from 2 to nearly 13 GPa, whereas the value measured on coated silicon decreases from  $\sim 54$  to an average of 28 GPa with a range of 2.7-79.6 GPa. The large range reflects the variation in modulus values measured across the wafer surface as shown in Figure 7.2. Possible sources of error include slippage, tip blunting, or material piling during testing. Aluminum oxide ALD films deposited at 50°C likely contain hydroxyls that reduce the overall density (and the modulus) compared to films deposited at higher temperature. Films deposited at  $\sim 180^\circ\text{C}$  show  $E \approx 180 \pm 8.2$  GPa,<sup>40</sup> and at 300 °C

values increase further to  $220 \pm 40$  GPa<sup>41</sup>. As for the nylon, it is reasonable to expect the aluminum oxide to increase the modulus compared to the uncoated fiber. The measured value reflects the influence of the underlying nylon.

The modulus for nylon and silicon coated with TiCl<sub>4</sub>/H<sub>2</sub>O increases to nearly 7 GPa and 300 GPa respectively. More measurements are needed to accurately measure the modulus for the sample treated with 100 cycles of TiCl<sub>4</sub>/H<sub>2</sub>O. The modulus for the TIP/H<sub>2</sub>O treated nanofibers show little change from the uncoated sample, changing to 1.3 GPa after 400 ALD cycles. The modulus for the titania coated silicon decreases to 18 GPa. The difference between the TiCl<sub>4</sub>/H<sub>2</sub>O and TIP/H<sub>2</sub>O treated nanofibers is expected due to the varying chemical interactions with the nylon as described in a previous work<sup>25</sup>. The modulus of the titania layer deposited on silicon using TIP/H<sub>2</sub>O is much lower than typical literature values, whereas the TiCl<sub>4</sub>/H<sub>2</sub>O treated silicon is slightly higher. According to literature, the modulus for titania varies slightly depending on deposition method but is in the range of 200-250 GPa<sup>42, 43</sup>. The lowest range of 9.5-10.5 GPa reported was observed with dip-coated TiO<sub>2</sub> coatings<sup>44</sup>. The value can also vary depending on crystallinity; Gheewala et al<sup>45</sup> determined that the modulus increases from ~170 GPa to 260 GPa as the crystalline phase changes from anatase to rutile. The TIP/H<sub>2</sub>O sample is closer to the lower range. This may be due to organic contaminants remaining in the titania layer or a decrease in film density. As for the TiCl<sub>4</sub>/H<sub>2</sub>O coated silicon, it is likely that with more measurements the modulus will get closer to the literature values.

An AFM image and corresponding force curve of a nylon nanofiber coated with 100 cycles of  $\text{TiCl}_4/\text{H}_2\text{O}$  after an indentation is shown in Figure 7.4. The trigger point used for this indent was higher than that used for the modulus calculations. The image shows a clear indentation in the shape of the AFM tip. That this indentation remains indicates that plastic deformation occurred during indentation. The trigger point was high enough to force the AFM tip far enough into the coated nanofiber to crack the titania coating. The loading portion of the force curve shows some changes in shape as in the indentation depth increases. These changes likely correspond to the different forces seen by the tip as it comes into contact with the titania coating, as force increases until the coating breaks, and the decrease in force as the tip interacts with the nylon as opposed to the metal oxide. While it is difficult to see where those changes occur in Figure 7.4, it is likely possible to change the trigger point to find an optimum setting to make them more apparent. This would give insight to the force the coatings can withstand before failure. It also appears that the AFM tip gets stuck in the fiber during the unloading process. This is likely due to the tip digging into the material. This may be an insightful tool to learn more about the properties of ALD coated nanofibers.

Another AFM tool that can give insight into the mechanical behavior of these materials is AM-FM mapping. Figure 7.5 shows an example image from this technique. The sample imaged was a cross-section of nylon nanofibers coated with  $\text{TiCl}_4/\text{H}_2\text{O}$ . The type of imaging is very sensitive to the stiffness of the substrate so it can discern between the nylon, epoxy, and titania portions. The darker coloring in the image corresponds to the softer nylon nanofibers. Each fiber is encapsulated by white indicating a stiff material, in this case titania. It is interesting to note that the sharpness of the white around the dark nanofibers, indicating

that there is an abrupt interface between the titania coating and the nanofiber. The graph of energy dissipation below the image shows how it is affected by the sample stiffness. The value stays stable as it interacts with the epoxy and then there is a sharp increase as it interacts with the titania coating followed by a dramatic decrease when it reaches the nylon nanofibers. The increase and subsequent decrease in energy dissipation as the AFM tip interacts with the titania film indicates a sharp interface between the nanofibers and titania. This type of force mapping can provide information about the modulus of the substrate materials and their morphology by differentiating between stiffness. It may also be useful for determining whether there is diffusion of the metal oxide precursors into the polymer by looking at the color gradation.

#### **7.4 Conclusions**

The deposition of aluminum oxide and titanium dioxide via  $\text{TiCl}_4/\text{H}_2\text{O}$  increased the modulus of individual nylon nanofibers as measured by AFM nanoindentation. The modulus of the nylon nanofiber did not increase after 400 ALD cycles of  $\text{TIP}/\text{H}_2\text{O}$ , which correlates well with the data presented in Chapter 6<sup>25</sup>. By changing the AFM settings it is possible to inflict plastic deformation on the nanofibers and view the resulting morphological effects. Additionally, while not observed here, it may be possible to see these effects in the force curves to analyze the force required to crack the metal oxide coating. Furthermore, AM-FM mapping results show a relatively stiff film on a less stiff substrate and can be used to generate force curves for modulus determination and gives insight into the sample morphology.

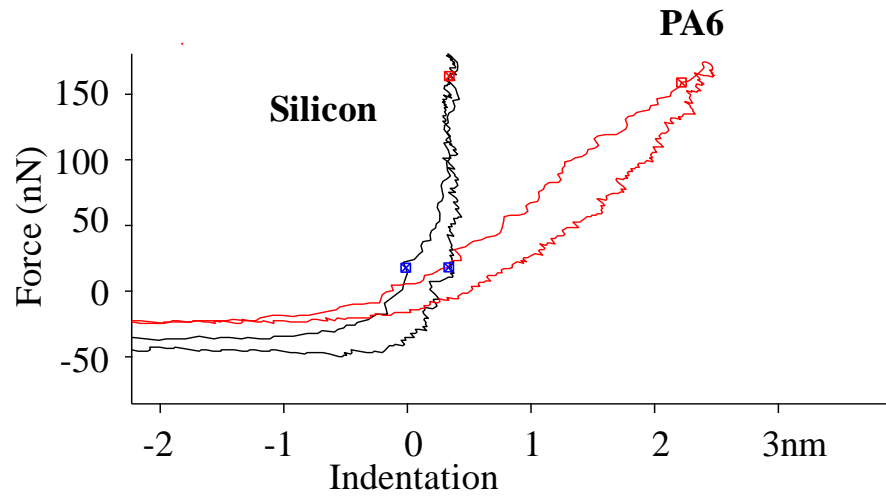


**Figure 7.1:** Force-indentation graph comparing the force curves for a silicon substrate and a nylon 6 nanofiber. The AFM cantilever experiences a greater amount of force for a more shallow indentation depth for the stiffer silicon substrate compared to the more pliant nylon nanofiber.

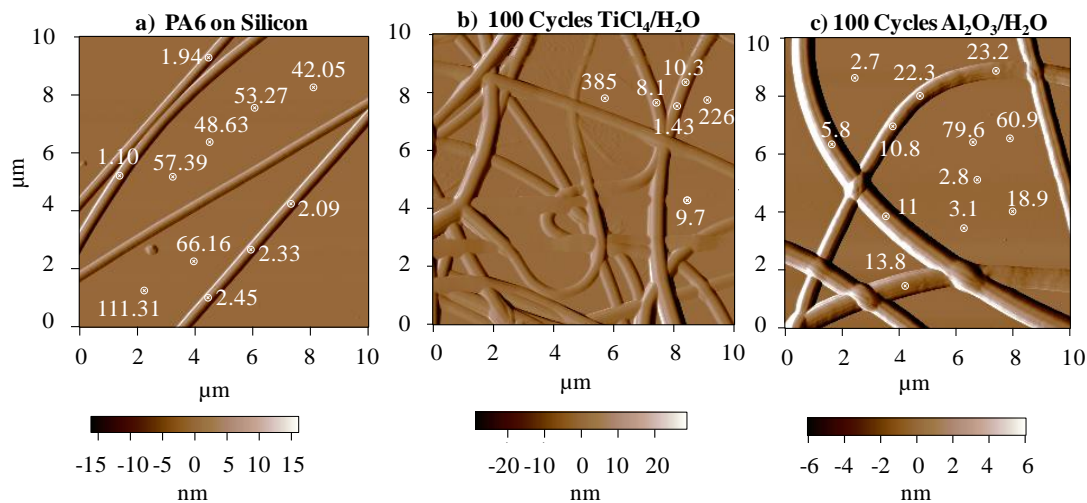


**Figure 7.2:** AFM images showing the (a) uncoated nylon 6 nanofibers on a silicon substrate, (b) the nanofibers and Si coated with 100 cycles of  $\text{TiO}_2$  coated using  $\text{TiCl}_4/\text{H}_2\text{O}$ , and (c) the nanofibers coated with 100 cycles of aluminum oxide. The numbers indicate the substrate modulus in GPa as measured by the Igor program.

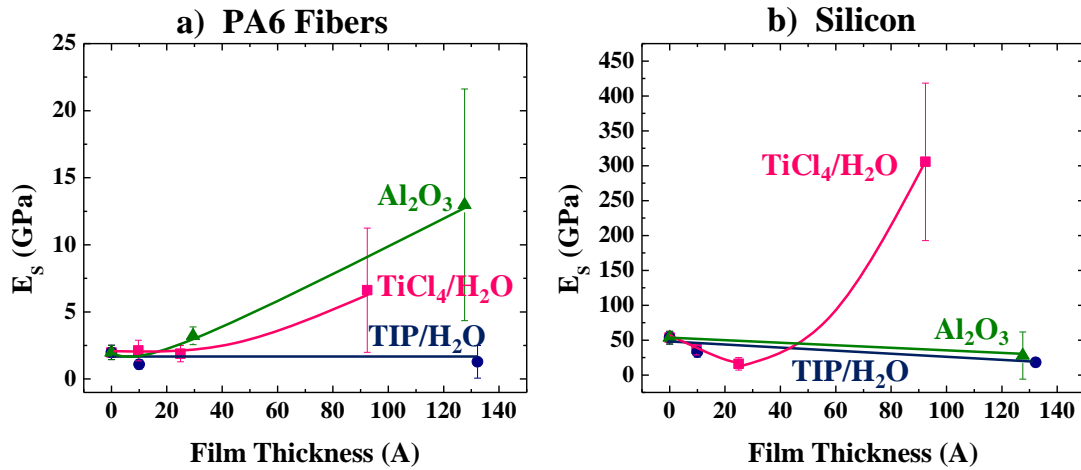


**Figure 7.3:** Modulus measured by AFM nanoindentation on (a) nylon 6 nanofibers and (b) silicon substrate. The modulus increases after the deposition of 100 ALD cycles of aluminum oxide and titanium dioxide using  $TiCl_4/H_2O$ . The modulus was unchanged after 400 cycles of TIP/ $H_2O$ , as anticipated according to previous results.

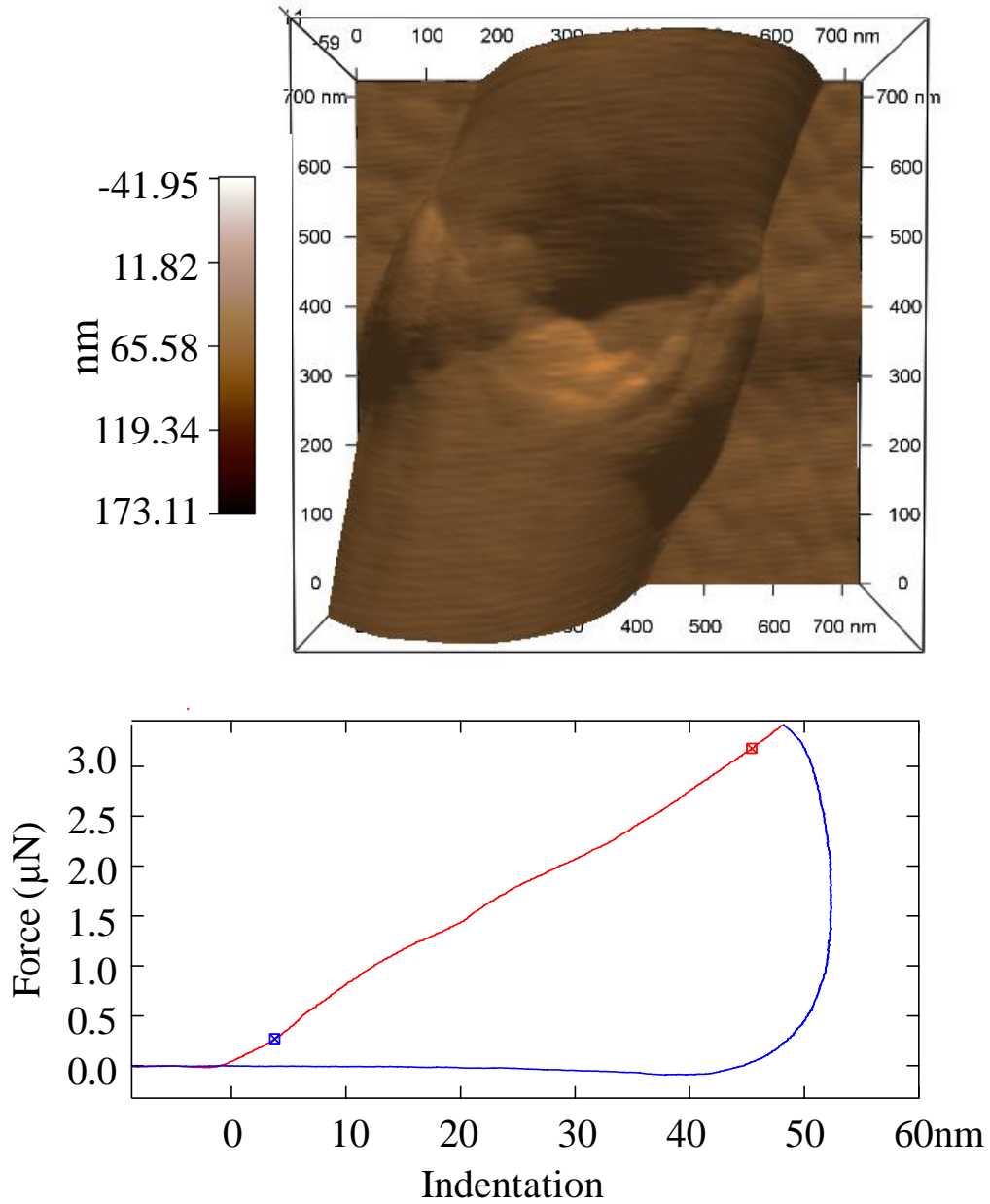


**Figure 7.4:** A Nylon 6 nanofiber coated with 100 cycles of titanium dioxide via  $\text{TiCl}_4/\text{H}_2\text{O}$  and its corresponding force curve after being depressed with the AFM cantilever. The force of the cantilever broke through the titanium dioxide coating and into the nanofiber, leaving the shape of the cantilever imprinted on the nanofiber.

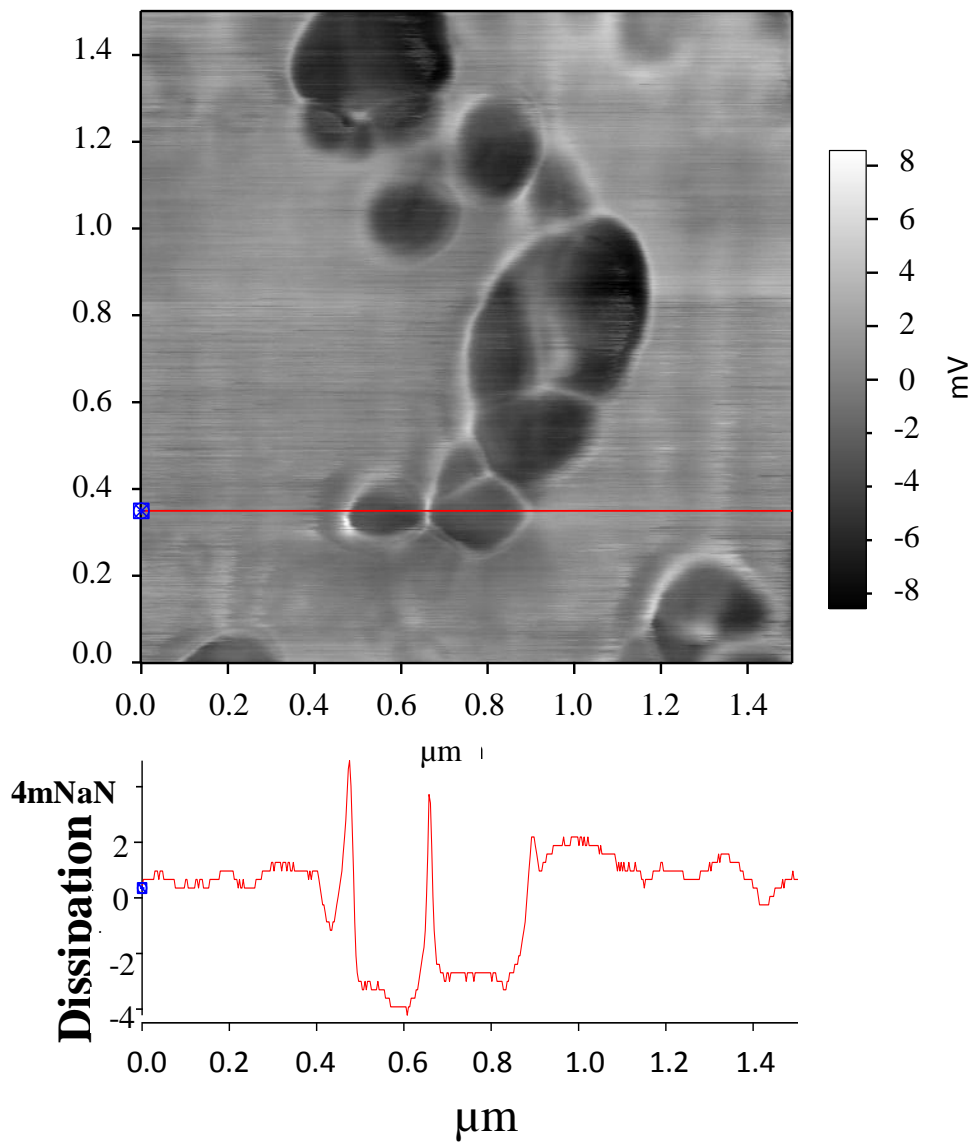


**Figure 7.5:** AM-FM AFM image of the cross-section of a nylon 6 nanofiber mat coated with 100 cycles of  $\text{TiCl}_4/\text{H}_2\text{O}$  ALD. This technique is sensitive to the stiffness of the underlying substrate as indicated by the change in dissipation as the cantilever interacts with the nanofibers compared to the stiffer surrounding epoxy.

## References

1. R. Gopal, S. Kaur, Z. W. Ma, C. Chan, S. Ramakrishna and T. Matsuura, *J. Membr. Sci.* **281** (1-2), 581-586 (2006).
2. P. Gibson, H. Schreuder-Gibson and D. Rivin, *Colloid Surf. A-Physicochem. Eng. Asp.* **187**, 469-481 (2001).
3. F. Chen, C. N. Lee and S. H. Teoh, *Mater. Sci. Eng. C-Biomimetic Supramol. Syst.* **27** (2), 325-332 (2007).
4. H. S. Yoo, T. G. Kim and T. G. Park, *Adv. Drug Deliv. Rev.* **61** (12), 1033-1042 (2009).
5. J. Zeng, A. Aigner, F. Czubayko, T. Kissel, J. H. Wendorff and A. Greiner, *Biomacromolecules* **6** (3), 1484-1488 (2005).
6. D. Bhattacharyya, K. Senecal, P. Marek, A. Senecal and K. K. Gleason, *Adv. Funct. Mater.* **21** (22), 4328-4337 (2011).
7. S. Z. Ji, Y. Li and M. J. Yang, *Sens. Actuator B-Chem.* **133** (2), 644-649 (2008).
8. J. S. Jeong, S. Y. Jeon, T. Y. Lee, J. H. Park, J. H. Shin, P. S. Alegaonkar, A. S. Berdinsky and J. B. Yoo, *Diam. Relat. Mat.* **15** (11-12), 1839-1843 (2006).
9. Z. M. Huang, Y. Z. Zhang, M. Kotaki and S. Ramakrishna, *Compos. Sci. Technol.* **63** (15), 2223-2253 (2003).
10. J. S. Jur, W. J. Sweet, C. J. Oldham and G. N. Parsons, *Adv. Funct. Mater.* **21** (11), 1993-2002 (2011).
11. W. K. Son, J. H. Youk and W. H. Park, *Carbohydr. Polym.* **65** (4), 430-434 (2006).

12. J. H. Park, B. S. Kim, Y. C. Yoo, M. S. Khil and H. Y. Kim, *J. Appl. Polym. Sci.* **107** (4), 2211-2216 (2008).
13. Q. F. Wei, Y. Liu, D. Y. Hou and F. L. Huang, *J. Mater. Process. Technol.* **194** (1-3), 89-92 (2007).
14. D. Pappas, A. Bujanda, J. D. Demaree, J. K. Hirvonen, W. Kosik, R. Jensen and S. McKnight, *Surf. Coat. Technol.* **201** (7), 4384-4388 (2006).
15. M. L. Ma, Y. Mao, M. Gupta, K. K. Gleason and G. C. Rutledge, *Macromolecules* **38** (23), 9742-9748 (2005).
16. M. D. Groner, S. M. George, R. S. McLean and P. F. Carcia, *Appl. Phys. Lett.* **88** (5) (2006).
17. A. A. Dameron, S. D. Davidson, B. B. Burton, P. F. Carcia, R. S. McLean and S. M. George, *J. Phys. Chem. C* **112** (12), 4573-4580 (2008).
18. K. Lee, J. S. Jur, D. H. Kim and G. N. Parsons, *J. Vac. Sci. Technol. A* **30** (1) (2012).
19. G. K. Hyde, G. Scarel, J. C. Spagnola, Q. Peng, K. Lee, B. Gong, K. G. Roberts, K. M. Roth, C. A. Hanson, C. K. Devine, S. M. Stewart, D. Hojo, J. S. Na, J. S. Jur and G. N. Parsons, *Langmuir* **26** (4), 2550-2558 (2010).
20. W. J. Sweet, J. S. Jur and G. N. Parsons, *J. Appl. Phys.* **113** (19) (2013).
21. Q. Peng, X. Y. Sun, J. C. Spagnola, G. K. Hyde, R. J. Spontak and G. N. Parsons, *Nano Lett.* **7** (3), 719-722 (2007).
22. J. C. Spagnola, B. Gong, S. A. Arvidson, J. S. Jur, S. A. Khan and G. N. Parsons, *J. Mater. Chem.* **20** (20), 4213-4222 (2010).

23. C. J. Oldham, B. Gong, J. C. Spagnola, J. S. Jur, K. J. Senecal, T. A. Godfrey and G. N. Parsons, *J. Electrochem. Soc.* **158** (9), D549-D556 (2011).
24. E. Santala, M. Kemell, M. Leskela and M. Ritala, *Nanotechnology* **20** (3) (2009).
25. C. D. McClure, C. J. Oldham, H. J. Walls and G. N. Parsons, *J. Vac. Sci. Technol. A* ((in press)).
26. S. M. Lee, E. Pippel, U. Gosele, C. Dresbach, Y. Qin, C. V. Chandran, T. Brauniger, G. Hause and M. Knez, *Science* **324** (5926), 488-492 (2009).
27. R. Inai, M. Kotaki and S. Ramakrishna, *Nanotechnology* **16** (2), 208-213 (2005).
28. R. Jalili, M. Morshed, S. Abdolkarim and H. Ravandi, *J. Appl. Polym. Sci.* **101** (6), 4350-4357 (2006).
29. M. B. Bazbouz and G. K. Stylios, *J. Polym. Sci. Pt. B-Polym. Phys.* **48** (15), 1719-1731 (2010).
30. E. P. S. Tan, S. Y. Ng and C. T. Lim, *Biomaterials* **26** (13), 1453-1456 (2005).
31. E. P. S. Tan and C. T. Lim, *Appl. Phys. Lett.* **87** (12) (2005).
32. J. J. Roa, G. Oncins, J. Diaz, X. G. Capdevila, F. Sanz and M. Segarra, *J. Eur. Ceram. Soc.* **31** (4), 429-449 (2011).
33. L. M. Bellan, J. Kameoka and H. G. Craighead, *Nanotechnology* **16** (8), 1095-1099 (2005).
34. J. E. Sader, J. W. M. Chon and P. Mulvaney, *Rev. Sci. Instrum.* **70** (10), 3967-3969 (1999).
35. L. Shen, W. C. Tjiu and T. X. Liu, *Polymer* **46** (25), 11969-11977 (2005).

36. G. A. Bell, D. M. Bielinski and B. D. Beake, *J. Appl. Polym. Sci.* **107** (1), 577-582 (2008).
37. L. Li, L. M. Bellan, H. G. Craighead and M. W. Frey, *Polymer* **47** (17), 6208-6217 (2006).
38. J. H. Choi and C. S. Korach, *Int. J. Precis. Eng. Manuf.* **12** (2), 345-354 (2011).
39. T. H. Wang, T. H. Fang and Y. C. Lin, *Mater. Sci. Eng. A-Struct. Mater. Prop. Microstruct. Process.* **447** (1-2), 244-253 (2007).
40. M. K. Tripp, C. Stampfer, D. C. Miller, T. Helbling, C. F. Hermann, C. Hierold, K. Gall, S. M. George and V. M. Bright, *Sens. Actuator A-Phys.* **130**, 419-429 (2006).
41. K. Tapily, J. E. Jakes, D. S. Stone, P. Shrestha, D. Gu, H. Baumgart and A. A. Elmustafa, *J. Electrochem. Soc.* **155** (7), H545-H551 (2008).
42. S. S. Pradhan, S. Sahoo and S. K. Pradhan, *Thin Solid Films* **518** (23), 6904-6908 (2010).
43. A. K. Prasad, R. Jha, R. Ramaseshan, S. Dash, I. Manna and A. K. Tyagi, *Surf. Eng.* **27** (5), 350-354 (2011).
44. H. Yaghoubi, N. Taghavinia, E. K. Alamdari and A. A. Volinsky, *ACS Appl. Mater. Interfaces* **2** (9), 2629-2636 (2010).
45. I. Gheewala, R. Smith and S. D. Kenny, *J. Phys.-Condes. Matter* **20** (35) (2008).

## **Chapter 8. Modulation of Bulk Mechanical Properties of Polymers by Vapor-Phase Treatments using Atomic Layer Deposition of Al<sub>2</sub>O<sub>3</sub> and TiO<sub>2</sub>.**

### **Abstract**

Polymers possess many unique physical properties and are commonly used in industrial applications due to their ease of processing. The deposition of thin films on different polymer materials is of interest, and has been widely studied for as a means of functionalization. In particular, atomic layer deposition (ALD) is a facile method for functionalizing polymer materials with thin films. The nucleation and growth of thin films on polymers by ALD is commonly investigated with cross-section transmission electron microscopy and quartz crystal microbalance techniques. In this study, we use thin bars of melt-molded polymers, including nylon, polypropylene, and Pellethane 2363-55D to study bulk mechanical properties and how they are affected by depositing inorganic thin films by ALD under a range of process conditions. The addition of aluminum oxide thin films to nylon, Pellethane 2363-55D and polypropylene at 100°C increases the elastic modulus, and the extend of modulus change increases using longer reactant exposure times. The longer exposure increases the extent of reaction, allowing for deeper penetration of the metal organic precursor.

## 8.1 Introduction

Inorganic-polymer hybrid materials are of interest for chemical resistance, improved diffusion barriers<sup>1</sup>, flexible electronics<sup>2</sup>, solar cells<sup>3</sup>, and sensors<sup>4</sup>. A variety of wet chemical methods are used to create these inorganic-organic hybrid materials such as sol-gel<sup>5</sup>, hydrothermal<sup>6</sup>, and other wet chemical methods. However, these processes may involve harsh solvents that deteriorate the polymer substrate. Another method of depositing inorganic films is by atomic layer deposition (ALD). Atomic layer deposition is an excellent technique for functionalizing temperature sensitive substrates such as polymers in that it may be performed at lower temperatures<sup>7</sup>. Using sequential self-limiting vapor phase reactions, a thin inorganic film is deposited with near monolayer control over thickness. Moreover, ALD is a technique capable of providing conformal and uniform films on a variety of substrates. It has been used with polymers to add functionality for diffusion barriers<sup>8,9</sup>, increase conductivity<sup>10</sup>, for flexible electronics<sup>11</sup>, to alter wettability<sup>12,13</sup>, and to create 3D structures where a polymer is used as a sacrificial layer<sup>14,15,16</sup>.

Film growth on polymers varies depending on temperature and dosing conditions. Previous authors reported that altering dosing conditions promotes diffusion into polymers and subsequently increases the amount of inorganic within the polymer network<sup>17,18</sup>. The deposition temperature also affects the diffusion distance into the polymer. For example, less subsurface film growth was previously observed at lower temperatures for both polypropylene<sup>17,18</sup> and nylon 6<sup>17,19</sup>. Film growth may also vary depending on the polymer being used. Polymers with reactive sites demonstrate a larger mass uptake by QCM during the first few ALD cycles compared to unreactive polymers such as polypropylene<sup>18,17</sup>. It has

also been shown that using microdose vapor infiltration increases the mechanical properties of spider silk<sup>20</sup>. This change in mechanical response was ascribed to precursor diffusion into the silk leading to breakage in hydrogen bonds. The broken hydrogen bonds were then thought to react to form metal-coordinated or covalent bonds. The breakage of hydrogen bonds and insertion of metal ions decreased the size of the protein  $\beta$ -sheet crystallites, which is thought to have increased the amount of amorphous regions leading to an increase in the max extensibility and max stress. Therefore, based on the current literature, it is possible to tune the mechanical properties of polymers by controlling the precursor exposure time and order.

In this work we investigate the effect of precursor exposure time on polypropylene (PP), nylon 6, and a common industrial thermoplastic polyurethane elastomer, Pellethane 2363-55D (P55D). We vary the ALD precursor exposure time in an effort to either promote or minimize diffusion into the substrate. The tensile properties of the treated samples were then measured to relate the growth characterization to the bulk response of the polymer. In addition, we investigate the role of molecular weight in the mechanical properties of ALD coated PP and polyethylene oxide (PEO). Finally, we explored various coatings and laminates and assess the ability of ALD to improve the water resistance of high molecular weight PEO.

## 8.2 Experimental

### 8.2.1 Melt-Pressing

For mechanical testing, polymer beads were melt-pressed into thin bars with enlarged ends pictured in Figure 8.1. These “dog bone” pieces were shaped according to ASTM standard D638 and had a thickness of ~0.345 mm. The polymers used were polypropylene (PP,  $M_w$  ~ 250,000 or 580,000), nylon 6, and polyethylene oxide (PEO,  $M_v$  of 100,000 or  $1 \times 10^6$ ). The PP, PEO, and nylon 6 were purchased from Sigma Aldrich. A thermoplastic polyurethane elastomer, Pellethane 2363-55D (P55D), was purchased from Lubrizol. The nylon 6, high molecular weight (HMW) PP, and P55D beads were pressed at 210°C. The low molecular weight (LMW) polypropylene was pressed at 160°C while the low and high MW PEO was pressed at ~90°C and ~100°C, respectfully. After melt-pressing, the samples were cooled between metal plates. A thin film of P55D was melt-pressed for FTIR analysis. Films of high molecular weight PEO were also pressed to determine whether the ALD coating would successfully encapsulate the samples thereby improving their water resistance.

### 8.2.2 Atomic Layer Deposition

The aforementioned polymers were coated in a home-built hot-walled viscous flow reactor. Nitrogen (99.999%) was used as the carrier gas and the chamber pressure was ~3.5 Torr. Aluminum oxide was deposited using trimethyl aluminum (TMA, 98%, STREM Chemicals) and deionized water as precursors. Two different recipes were developed and used to coat the polymer samples. The first ALD recipe used relatively short precursor and reactant dose times separated by a nitrogen purge. The exposure times for TMA/N<sub>2</sub>/H<sub>2</sub>O/N<sub>2</sub>

were 0.1/45/0.1/30 seconds, respectively. The second method used similar dose times, but a “hold” step was added after the precursor dose. During the hold, the reactor chamber was isolated from the pump, allowing more time for the precursors to interact with the samples. The process timing followed TMA(hold)/N<sub>2</sub>/H<sub>2</sub>O(hold)/N<sub>2</sub> = 0.5(60)/180/0.5(60)/180 seconds. The depositions were performed at 50°C and 100°C. As experimental controls, several polymer samples were exposed to the same thermal cycle, but did not receive any precursor exposure. Due to temperature sensitivity, the PEO was only coated and heat treated at 50°C. Additionally, polypropylene and nylon 6 samples were treated at 100°C to an ALD “microdose” process. One TMA microdose step consisted of a 0.15s TMA dose, a 60s hold and a 45s purge. To make one ALD macrocycle, this step was repeated 9 times, followed by one similar water microdose. Samples were treated to 10 or 50 macrocycles. A silicon wafer was placed in the reactor with the polymers for each run to monitor Al<sub>2</sub>O<sub>3</sub> growth. For the PEO samples undergoing water testing, a variety of laminates were used by mixing aluminum oxide seed layers with titanium dioxide coatings. The different ALD treatments performed in this study are listed in Table 8.3.

### **8.2.3 Instron Testing**

The mechanical properties of the polymer bars were measured using an Instron 5943 Tensile tester equipped with a 1 kN load cell and pneumatic grips. The gauge length was 2.5 cm and the crosshead speed was set to 25 mm/min. The samples were strained until failure while the stress was measured, and 5 samples were tested for each data point.

#### *Characterization*

Transmission electron microscopy was used to analyze the film thickness on the polymers. The samples were cut using a microtome and imaged at the Analytical Instrumentation Facility at North Carolina State University. The samples were imaged with either a JEOL 2000FX S/TEM or a Hitachi HF2000 TEM. Additionally, FTIR was used to analyze the chemical changes occurring in the P55D as a result of the ALD process. The thin P55D film used for FTIR was treated using the traditional ALD recipe at 50°C. The FTIR used was a Thermo Nicolet Magna 750, equipped with a nonpolarized IR beam, a KBr beamsplitter, and a deuterated triglycine sulfate detector.

#### **8.2.4 Water Testing**

High MW PEO samples pressed into 0.9 mm thick films were cut into pieces 0.5 in. wide and 1 in. height. The samples were weighed before and after ALD coating. After coating, the samples were placed into ~20 mL of deionized water for 5 minutes followed by gently blotting the sample with a laboratory tissue to remove any remaining water. The samples were allowed to dry at room temperature for 30 minutes and were then reweighed.

### **8.3 Results**

#### **8.3.1 TEM**

The TEM images of the polymer cross-sections in Figure 8.2 (a-i) show conformal films on all polymer samples. The surface and subsurface growth determined from the TEM images, as well as the thicknesses measured on silicon wafers are listed in Table 8.1. All samples were treated with 200 cycles of either the ALD or ALD-hold recipe at 50°C or 100°C. The nylon sample coated at 50°C (Figure 8.2a) shows a distinct interface between

the dense Al<sub>2</sub>O<sub>3</sub> film on the polymer surface and the Al<sub>2</sub>O<sub>3</sub> subsurface growth. The surface and subsurface thicknesses are both ~66 nm, which is much higher than the 35 nm thickness measured on the Si wafer. The ALD-deposited film on the nylon sample treated at 100°C is shown in Figure 8.2d and has a much thinner film with surface and subsurface growth approximately half of that seen on the sample coated at 50°C. Moreover, the subsurface growth at 50°C is not as uniform for the higher deposition temperature. The nylon sample treated by the ALD-hold at 50°C (Figure 8.2g) has a very thick film of approximately 760 nm, and is much larger than the 43 nm measured on the Si monitor wafer. Several QCM studies have shown a large mass-uptake with polymer substrates during the first few ALD cycles<sup>17,18</sup>. The large uptake in mass is due to the precursors penetrating past the polymer surface and diffusing into the subsurface region. The thicker film on the 50°C ALD sample, compared to the 100°C ALD sample, is likely due to water present in the subsurface region that results by insufficient purging. As for the 100°C ALD sample, the increased temperature may aid in the purging of excess water leading to a thinner film. Alternatively, the high temperature may allow the precursors to diffuse further into the polymers, thus increasing the dispersion. In this case, it is possible that the dispersed regions of Al<sub>2</sub>O<sub>3</sub> growth do not coalesce to create a dense film within the polymer subsurface region, which makes contrast imaging with TEM difficult. Similarly, with the ALD-hold sample, the hold step may help promote diffusion of the precursors into the polymer resulting in more dispersed aluminum oxide as no subsurface growth observed in the TEM images.

The polypropylene TEM images of the samples coated using ALD at 50°C and 100°C are shown in Figures 8.2b and 8.2e, respectively. The images show that the coatings at two

different temperatures yield similar film thicknesses and correlate well with the Si monitor wafer. However, the subsurface growth measured for polypropylene is not uniform and includes only the near surface region. There appears to be more aluminum oxide that has diffused over 100 nm in to the polymer and coalesced into islands of aluminum oxide growth. The polypropylene sample treated using the ALD-hold recipe at 50°C has a thicker film than the other ALD samples reported with a thickness of approximately 45 nm, the same thickness measured by the Si monitor wafer. There is obvious subsurface growth in the form of coalesced particles, however, it is not possible to determine the thickness when subsurface growth ceases. The surface and subsurface growth of Al<sub>2</sub>O<sub>3</sub> on the ALD coated polypropylene at 50°C and 100°C are nearly equivalent and very similar to the growth measured on the silicon wafer monitor. Wilson et al<sup>21</sup> described a nucleation period where the ALD precursors become ensnared in the polymer near-surface region and react to begin film growth<sup>21</sup>. Since there are no reactive groups on the polypropylene polymer chain the nucleation is likely slower compared to polymers with reactive sites such as nylon and P55D. The slower growth found in this study is consistent with QCM data that shows less initial mass uptake for polypropylene compared to polymers with reactive sites such as nylon and polyvinyl alcohol<sup>17</sup>.

The ALD coated P55D samples have surface film thicknesses similar to the ALD treated polypropylene, with a thickness of ~30 nm for the samples deposited at 50°C (Figure 8.2c) and ~37nm for the samples deposited at 100°C (Figure 8.2f). Interestingly, the subsurface growth for this material, as probed by TEM reveals Al<sub>2</sub>O<sub>3</sub> diffusing approximately 250 nm into the bulk for samples treated at 50°C, whereas the diffusion depth

is nearly 600 nm for the sample treated at 100°C. The sample coated at 100°C has a very clear interface between the subsurface growth and the polymer, whereas the 50°C sample shows contrast fading with increasing depth into the polymer. When treated using the ALD-hold method, the surface film thickness increases to ~160 nm. Unlike the ALD treated samples, there is no obvious diffusion of aluminum oxide into the polymer.

### 8.3.2 FTIR

The FTIR difference spectra of the P55D thin film is shown in Figure 8.3 with the related peak assignments listed in Table 8.2. Each spectrum was obtained by subtracting the previous spectrum. The resulting spectra show how the chemical composition changes during each step. The untreated P55D shows IR peaks characteristic of polyurethanes, which are similar to the findings of Simmons et al.<sup>22</sup>. After 10 cycles of aluminum oxide there is a large change in the ether-associated bands indicating a reaction between the ALD precursors and the urethane polymer. Furthermore, after 10 cycles, there is a simultaneous increase in the Al-O band due to the growth of aluminum oxide. Reactions are still observed in the FTIR data after 100 cycles indicating that the ALD precursors are continuing to diffuse into the polymer bulk and locate additional reactive sites. The diffusion into the polymer bulk correlates well with the TEM data in Figures 8.2c and f. Previous studies were also performed on nylon 6 and polypropylene<sup>17, 23</sup>. The FTIR studies on nylon 6 demonstrate a large change in the chemical composition, with a decrease in the intensity associated with the carbonyl bands<sup>17,23</sup>. The decrease was seen early in the reaction and minimized with more cycles<sup>23</sup>. Since the reaction does not continue with further coating, it is possible that the aluminum oxide films are forming a diffusion barrier with increasing film thickness and

prevents further subsurface growth. The FTIR studies on polypropylene demonstrate a slight change in chemical composition after the first ALD cycle and minimal change afterwards, which indicates little chemical interaction between the ALD precursors (TMA and water) and the polypropylene<sup>17</sup>. Another study by Gong et al<sup>24</sup> used quantitative FTIR analysis to relate the relative extent of reaction between TMA and various polymers. The study determined the relative extent of reaction between TMA and polypropylene to be  $< 10$  whereas that for nylon to be  $\sim 590 \pm 90$ <sup>24</sup>. This correlates well with other FTIR studies<sup>17, 23</sup> and the thicker films seen in the TEM images for nylon.

### **8.3.3 Effect on Mechanical Data**

Representative stress-strain curves for uncoated nylon 6, polypropylene, and P55D are shown in Figure 8.4. Panel 8.4a shows a typical nylon sample that necked during testing; necking was also seen with polypropylene. Figure 8.5 shows the Young's Moduli calculated from the linear portion of the stress-strain curves. For the nylon samples shown in Figure 8.5a, the Young's modulus increases slightly for both the ALD and ALD-hold treated samples. It should be noted that the x-axis of film growth is the growth as measured on the silicon wafer monitor. For the ALD treated samples, the modulus increases from  $1.2 \pm 0.2$  GPa for untreated nylon and plateaus around  $1.4 \pm 0.1$  GPa after 100 cycles. The modulus increase is only slight and within error of the uncoated samples. No temperature dependence is observed in the samples coated using ALD at 50°C and 100°C. It is interesting that for the ALD treated nylon 6 samples, the elastic modulus is identical for the samples treated at 50°C and 100°C despite the difference in film thickness. The samples coated at 50°C have a clearly defined subsurface growth with a very thick film on the surface, whereas the samples

coated at 100°C have nearly half the film thickness on the surface and subsurface region. That this difference in growth does not affect the modulus of the materials indicates that the ALD-deposited film is not thick enough compared to the sample thickness to significantly alter the modulus. The samples treated with the ALD-holds also show similar results, however the modulus increases to approximately 1.6 GPa. The increase in elastic modulus compared to the ALD treated samples may be due to the thicker Al<sub>2</sub>O<sub>3</sub> film. According to the TEM images, the film thickness on the nylon 6 sample treated using the ALD-hold method at 50°C is ~760 nm, which is greater than 10 times thicker than the 50°C ALD sample.

In comparison to the nylon samples, the polypropylene samples in Figure 8.5b do exhibit a temperature difference. The 50°C ALD treated samples do not show any difference in modulus, whereas the modulus for the samples treated at 100°C increases from  $0.82 \pm 0.05$  GPa to ~ 1 GPa. The increase in modulus for the higher temperature ALD sample may be due to the deposition temperature and not the aluminum oxide. Furthermore, the heat treatment increases the modulus to  $1.16 \pm 0.06$  GPa. The heat-treated samples were allowed to cool at room temperature which may have increased the degree of crystallinity in the samples, thereby increasing the elastic modulus. The ALD-hold samples have a higher modulus than the ALD-treated samples even for the samples coated at 50°C, indicating that the effect is likely in part due to the aluminum oxide coating. The increase in modulus may be due to the TMA and water precursors having more time to diffuse into the polymer network and nucleate leading to a thicker Al<sub>2</sub>O<sub>3</sub> coating on the ALD-hold treated sample.

The ALD-hold samples coated at 100°C have the highest increase, reaching a modulus of nearly 1.3 GPa.

The P55D samples in Figure 8.5c show the largest percent change in modulus. The samples coated at 50°C using ALD and the ALD-hold treatments both have a larger increase in modulus than their 100°C counterparts. The modulus for the ALD hold samples increases the most, from roughly 75 MPa for the untreated samples to nearly 160 MPa after 200 ALD-hold cycles at 50°C. The increase in modulus may be due to the increased film thickness of 160 nm compared to 30 nm seen on the 50°C ALD sample. It is also possible that diffusion throughout the samples may increase the modulus.

The change in modulus for the microdose method is compared to the ALD-hold results shown in Figure 8.5. Interestingly, the samples treated with the microdose method have a modulus nearly equivalent to the ALD-hold process for both the nylon and polypropylene samples. The film thickness for the nylon samples, as measured by the silicon wafer monitor for the 10 and 50 microdose cycles, is equivalent to what would be expected for 100 and 200 cycles, respectively, at a growth rate of  $\sim 1.1 \text{ \AA}/\text{cycle}$ . The film thickness is much higher than the thickness measured for polypropylene which was 20  $\text{\AA}$  and 80  $\text{\AA}$  for the 10 and 50 microdose cycles, respectfully. The difference in thickness is likely a byproduct from the reaction between the nylon and TMA, which could lead to CVD growth on the silicon wafer. Since the reaction between polypropylene and TMA is minimal there are few byproducts to lead to excess growth on the silicon wafer. Moreover, the microdose and ALD-hold modulus for the polypropylene samples are similar even though the film thickness measured by silicon is different. The TMA on the silicon wafer was likely purged more

efficiently from the planar surface compared to the polypropylene resulting in a lower growth rate on the silicon. It is possible that the multiple TMA doses help promote TMA diffusion into the polypropylene, saturating the polymer matrix. When the sample is exposed to water it quickly reacts with the TMA in the polypropylene creating surface and subsurface aluminum oxide growth. Additionally, the processing time required for the microdose samples is much lower than for the holds, thus making it a more efficient treatment method compared to the ALD-hold treatment.

The strain at break for nylon and polypropylene, Figure 8.7a and 8.7b respectfully, shows a very large error bar for the uncoated samples. The large error is due to polymer necking during testing. It is interesting to note that as the number of ALD and ALD-hold cycles is increased the error bars become smaller, indicating that necking occurs less in these samples. The breaking behavior is more consistent within the samples, as well as more abrupt, which is similar to what would be expected for a more ceramic material such as aluminum oxide. In comparison, the elastomeric P55D samples do not show a decrease in the strain at break, and therefore maintain their flexibility.

#### **8.3.4 Effect of Molecular Weight**

The effect of the aluminum oxide film on the elastic modulus of PEO samples is shown in Figure 8.8. The uncoated modulus is  $520 \pm 25$  MPa for low MW PEO and  $545 \pm 34$  MPa for high MW PEO, which is slightly higher than the elastic modulus of 200 MPa for pristine PEO thin films as measured by AFM nanoindentation <sup>25</sup>. Similar studies using nanoindentation on PEO fibers have measured the modulus to be higher at  $7 \pm 0.5$  GPa <sup>26</sup> and  $1.39 \pm 0.35$  GPa <sup>27</sup>. Variations in modulus between the may be due to differences in the

method used for sample creation, crystallinity, and testing method. The elastic modulus for the low MW PEO increases nearly 35% compared to the uncoated material after 500 cycles or  $\sim 600 \text{ \AA}$  of aluminum oxide. The modulus for the heat treated samples also increases to  $\sim 37\%$  compared to the room temperature treated samples. After heat treatment, the samples were removed from the reactor and allowed to cool to room temperature. The sample may have an increased modulus due to molecular movement during heat treatment and a slow cooling rate leading to a higher degree of crystallinity. The high MW samples only show a slight increase in modulus after the deposition of  $\sim 800 \text{ \AA}$  of aluminum oxide. Heat treatment does not change the modulus for the high MW PEO samples. The data for strain at break for PEO is included in Figure 8.8. The strain at break for the high MW PEO shows little change and is unaffected by ALD and heat treatment. The low MW PEO shows a slight decrease in strain at break with increasing film thickness. A decrease in the strain at break may be a result of the samples becoming more brittle due to the ceramic nature of the ALD coating. It would be expected that as the thickness of the alumina layer increases, the PEO samples would begin to have bulk properties more similar to the alumina. The increase in alumina would be marked by an increase in modulus and a decrease in the strain at break. It is also possible, given the reactive nature of the PEO backbone that TMA and water are reacting with the polymer chains causing chain scission. Chain scission causes the polymer chain length to decrease so the sample will not be able to stretch as far compared to the untreated samples. Since the low molecular weight samples have shorter chains, they will also have more hydroxyl terminated chain ends for the nucleation of aluminum oxide. In contrast, the higher molecular weight sample has longer polymer chains and fewer hydroxyl ends for

nucleation compared to the low molecular weight sample which may lead to slower aluminum oxide growth. There may also be differences in the density of the films. If the high molecular weight film is denser the ALD precursors may not diffuse into the sample as easily as in the low molecular weight sample. If the precursors diffuse further into the material it would increase the number of reactive sites available and therefore increase the number of shortened polymer chains, as well as the degree of subsurface growth of alumina. A larger percentage of alumina in the low MW PEO sample would explain the greater increase in elastic modulus compared to the high MW samples.

The effect of aluminum oxide deposition on the elastic modulus and strain at break of polypropylene is shown in Figure 8.9. For the polypropylene samples, there is little change in elastic modulus after aluminum oxide deposition. While there is some variation from the uncoated samples it is not outside of the measured error. The results are similar for the strain at break where there is a slightly larger decrease in strain at break for the lower MW PP, but it is within error.

It is interesting to note the difference between the reactive PEO and inert PP samples. It is likely that TMA and water react with the polymer chains in the PEO. The reaction between the ALD precursors and the PEO would shorten the polymer chains and have a larger effect on the bulk material properties. In comparison, TMA and water have little reaction with polypropylene leading to slower growth and nucleation. Moreover, ALD reaction with PP would have little to no effect on the polymer chain length. The slower growth and lack of reaction would mean that the aluminum oxide would not have as great of an effect on the polypropylene compared to reactive substrates such as PEO.

### 8.3.5 Water Resistance

Table 8.3 describes the mass changes for the high MW PEO samples. There was only a slight mass increase after treatment with atomic layer deposition. Due to the small surface area of the samples, a large increase in mass is not expected. All coated samples are similar to the uncoated samples in terms of size and color except for the samples coated with 200 cycles of aluminum oxide followed by 600 cycles of titanium dioxide which are darker in color as shown in Figure 8.10. The change in color is likely due to the increased thickness of the laminate film. After the samples were removed from water, the films increased in volume by approximately 160%. Figure 8.10 also shows an example of a sample ~30 minutes after water exposure. The more transparent portions of the sample highlight the effect of sample swelling. Moreover, the mass increase due to swelling for all samples after ~30 minutes of drying is high. It is surprising that the sample coated with only 100 cycles of titanium dioxide show the smallest percent mass increase due to swelling, especially since it is likely the sample will have the thinnest metal oxide film. Increasing the number of aluminum oxide cycles to 100 and the titanium dioxide cycles to 400 decreases the mass uptake slightly, but not to the same degree as 100 cycles of titanium dioxide alone. It may be that the aluminum oxide seed layer damages or roughens the surface of the sample. There could also be differences in film densities. A less dense film will be more likely to allow water to diffuse into the sample. The density of titanium dioxide is higher than that of aluminum oxide at  $\sim 4.23 \text{ g/cm}^3$  compared to  $3.95 \text{ g/cm}^3$  for aluminum oxide. The deposition of titanium dioxide alone may create a more dense film compared to a laminate film. By

changing the laminate material or increasing the number of cycles a better diffusion barrier may be achieved.

#### **8.4 Conclusion**

Atomic layer deposition using short precursor doses and extended precursor dose and holds were used to coat nylon 6, polypropylene, and P55D polymers with aluminum oxide. Film growth on the polymers and the affect of the film on the mechanical properties were analyzed. Using TEM, subsurface growth is seen on all samples after treatment with ALD, especially the P55D samples. The TEM images of the samples coated using ALD-holds do not show any subsurface aluminum oxide growth, which indicates either that there was no subsurface growth or that the precursors diffused throughout the polymer such that no contrast is observed by TEM. The samples treated using the ALD-hold method have larger film thicknesses and increased moduli compared to their ALD counterparts. The addition of the aluminum oxide coating increases the modulus of the P55D samples while the flexibility is maintained. Additionally, using a microdose method more efficiently increased the modulus to the same degree as the ALD-holds, whereby longer processing times were required. The molecular weight of the polymer also has an effect on the degree to which ALD affects the mechanical properties when using a reactive polymer. It was demonstrated that precursor exposure order and precursor exposure time are important factors that affect film growth on the substrate as well as the mechanical properties of the substrate. Additionally, the reactivity of the substrate and physical properties such as molecular weight

play an important role in the effect of ALD thin films and the mechanical properties of the composite material.

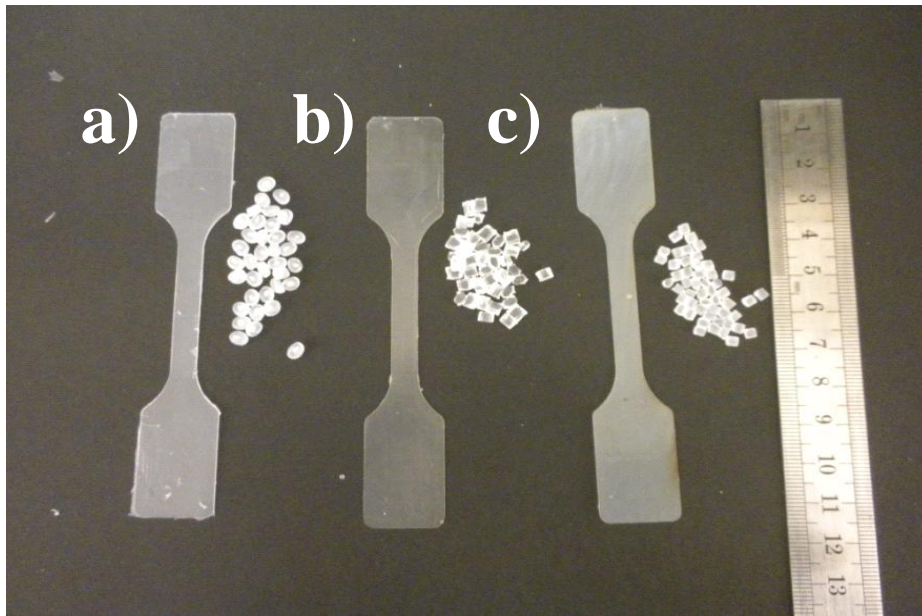


**Figure 8.1:** Melt-pressed (a) polypropylene (b) P55D and (c) nylon 6 and the beads used for melt-pressing.

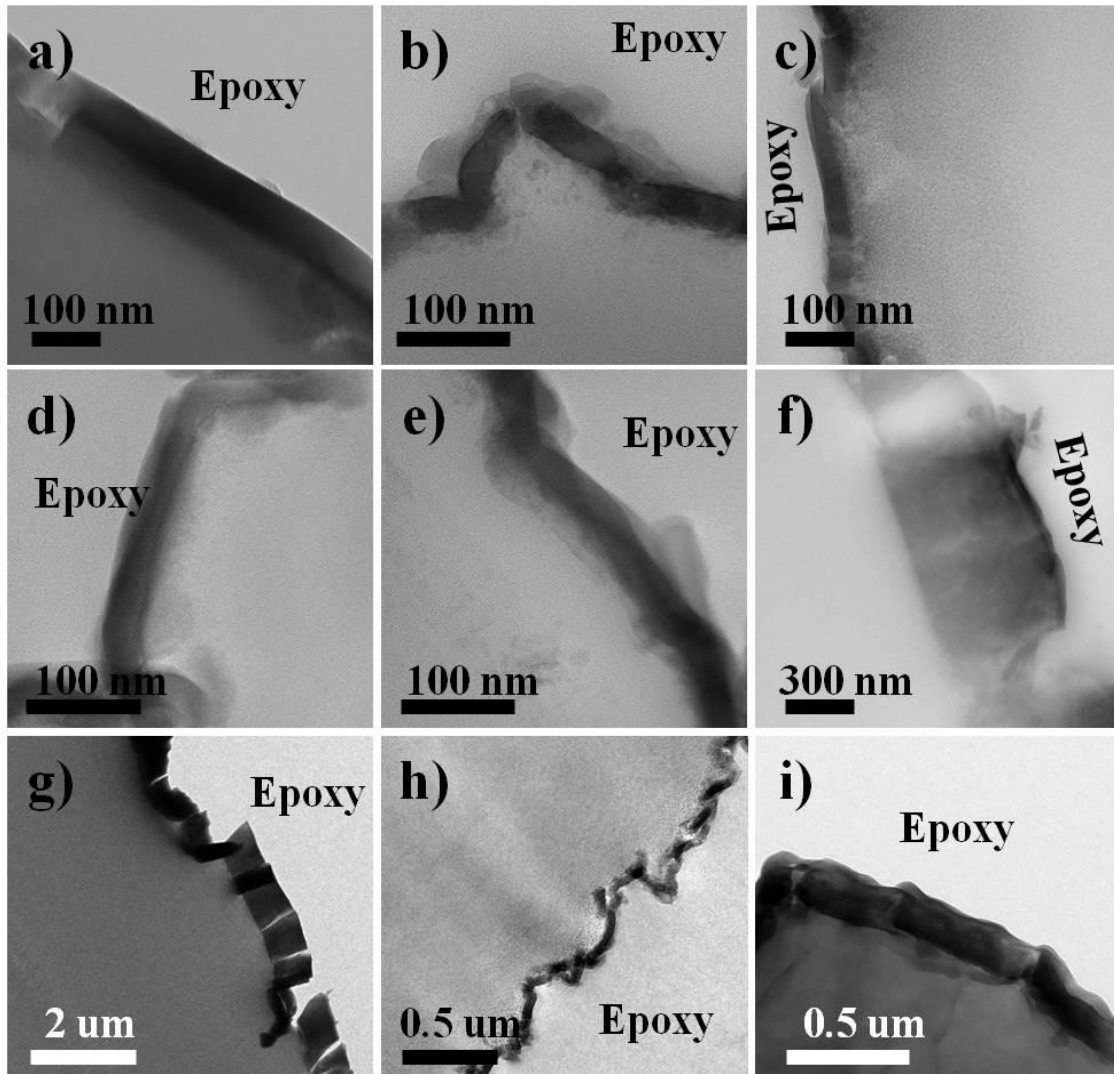


**Figure 8.2:** Cross-sectional TEM images of aluminum oxide coated nylon (a, d, g), polypropylene (b, e, h), and P55D (c, f, i). Samples (a)-(c) were coated at 50°C with 200 ALD cycles whereas samples (d)-(f) were coated at 100°C. Longer precursor exposures were used for panels (g)-(I) which were coated with 200 ALD-hold cycles at 50°C.

**Table 8.1:** Film thicknesses measured on polymer samples after 200 cycles of either ALD or ALD-holds as measured by TEM and the film thicknesses on the silicon wafer monitor measured by ellipsometry.

<b>ALD</b>				
<b>Polymer</b>	<b>Temperature (°C)</b>	<b>Film Thickness (nm)</b>	<b>Subsurface Thickness (nm)</b>	<b>Thickness on Si (nm)</b>
PA6	50	66 ± 4	66 ± 9	35.2 ± 0.4
PA6	100	33 ± 3	25 ± 10	29.5 ± 0.2
PP	50	27 ± 4	14 ± 6	34.9 ± 0.4
PP	100	29 ± 6	18 ± 6	28.5 ± 0.1
P55D	50	30 ± 5	252 ± 20	32.4 ± 0.4
P55D	100	37 ± 4	610 ± 80	29.3 ± 0.2
<b>ALD-Holds</b>				
<b>Polymer</b>	<b>Temperature (°C)</b>	<b>Film Thickness (nm)</b>	<b>Subsurface Thickness (nm)</b>	<b>Thickness on Si (nm)</b>
PA6	50	760 ± 50	-	43.7 ± 0.6
PP	50	45 ± 4	-	45.3 ± 0.3
P55D	50	170 ± 21	-	45 ± 1

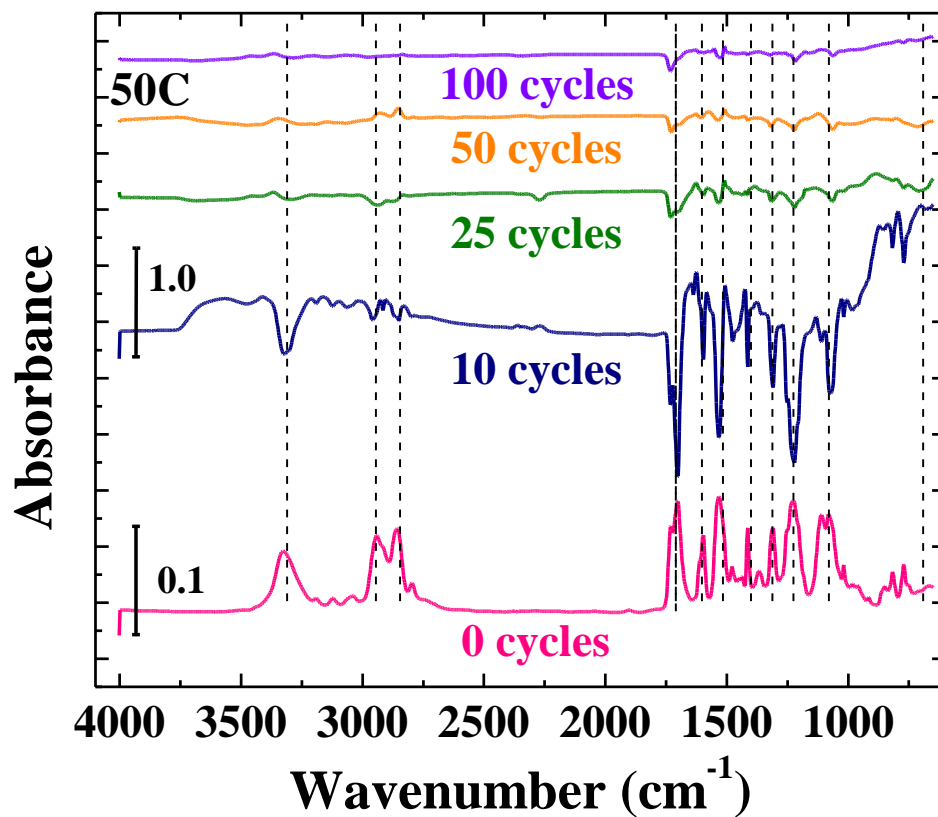


**Figure 8.3:** FTIR difference spectra of P55D coated with aluminum oxide using ALD at 50C. A large change occurs after the first 10 ALD cycles, but the precursors continue to react with the P55D even after 100 cycles. The bare spectrum has been normalized by a factor of 0.1 compared to the coated spectra.

**Table 8.2:** FTIR peak assignments for the P55D spectra shown in Figure 8.3.

<b>Band (cm<sup>-1</sup>)</b>	<b>Assignment</b>
3326	N-H stretch
2940	CH <sub>2</sub> asymmetric stretch
2858	CH <sub>2</sub> symmetric stretch
1730	Non-hydrogen bonded urethane C=O stretch
1703	Hydrogen bonded urethane stretch
1597	N-H bend
1533	Urethane N-H bend and C-N stretch
1413	C-H bend
1311	Urethane N-H bend and C-N stretch
1227	Urethane C-N stretch
1110	Ether C-O-C stretch
1080	Urethane C-O-C stretch
700	Al-O

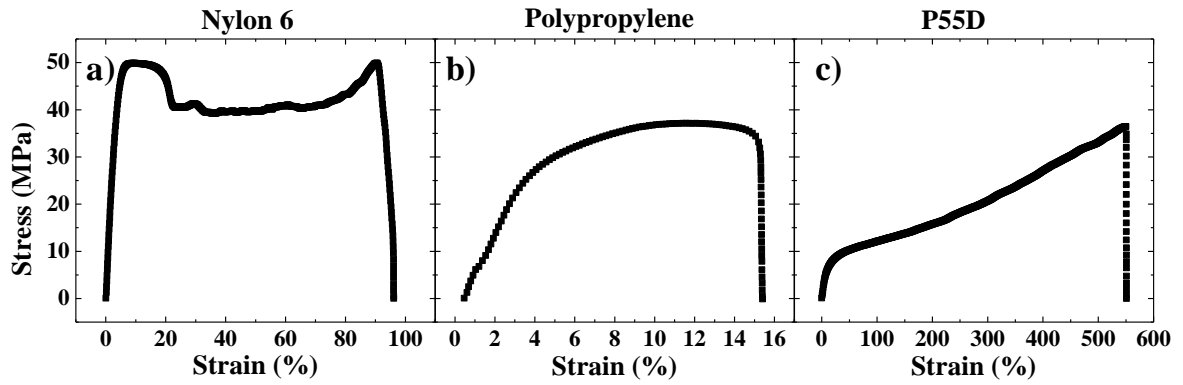


**Figure 8.4:** Examples of stress-strain curves from uncoated (a) nylon 6, (b) polypropylene and (c) P55D. Several uncoated nylon 6 and polypropylene samples necked during testing as shown in panel (a).

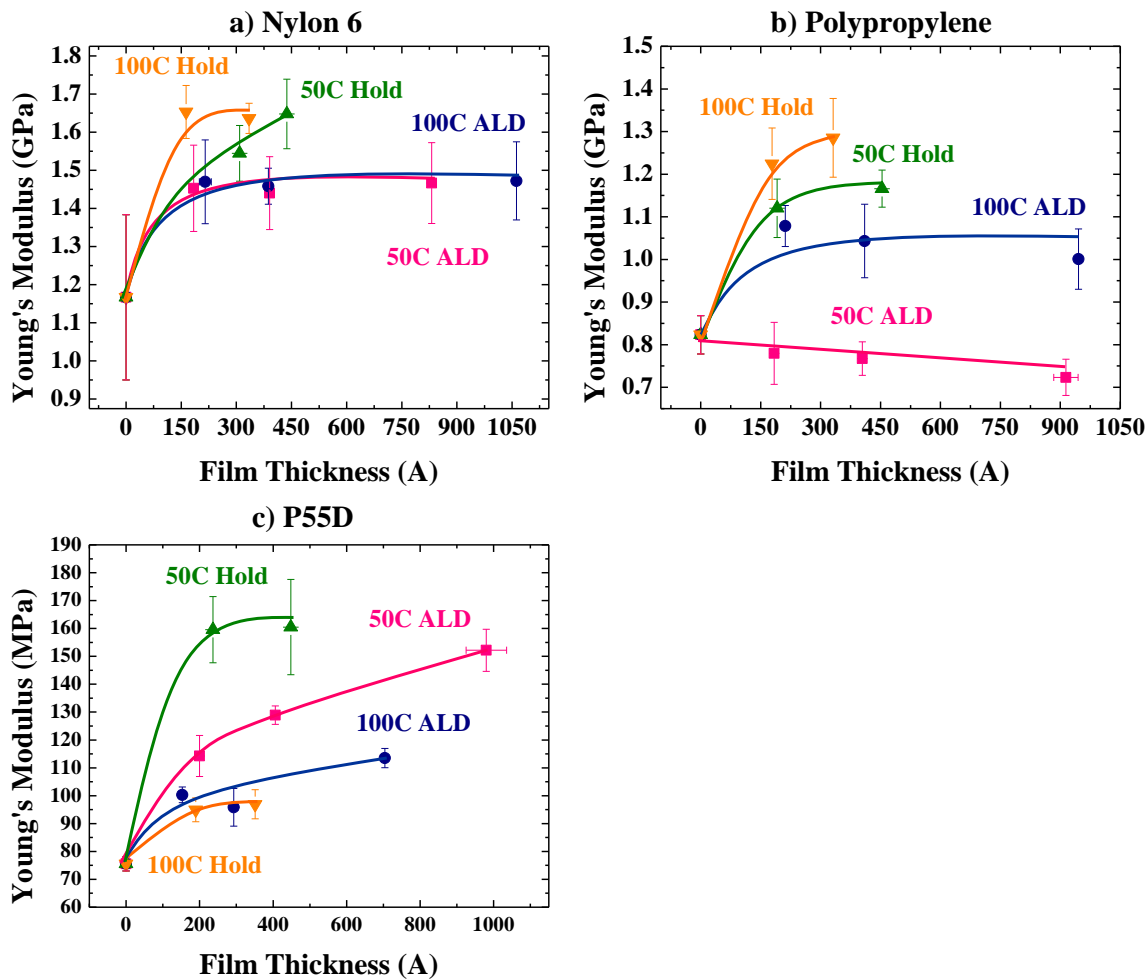


**Figure 8.5:** Young's modulus for (a) nylon 6, (b) polypropylene and (c) P55d after being treated with either ALD or ALD-holds at 50C and 100C. The ALD-hold treated samples have a larger increase in modulus compared to the ALD treated samples. The P55D samples have the largest increase with the modulus being more than doubled after 100 ALD-hold cycles at 50C.

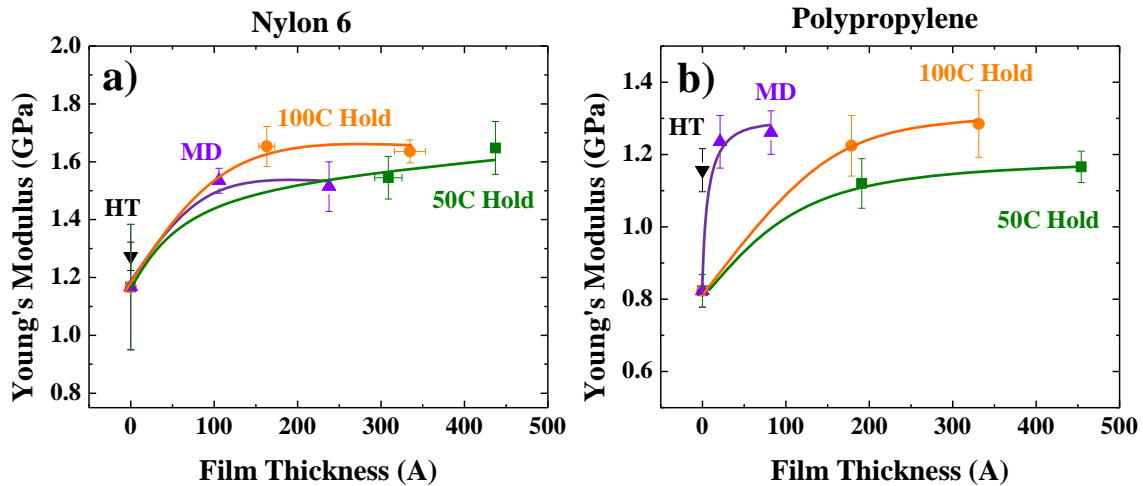


**Figure 8.6:** Comparison in Young's Modulus for (a) nylon 6 and (b) polypropylene treated using a microdose (MD) method versus ALD-holds and heat treated (HT) samples. The microdose method is as effective at the hold method with nearly equivalent increases in modulus with less processing time. While the heat treatment had little effect on the nylon 6, the modulus of polypropylene was largely increased.

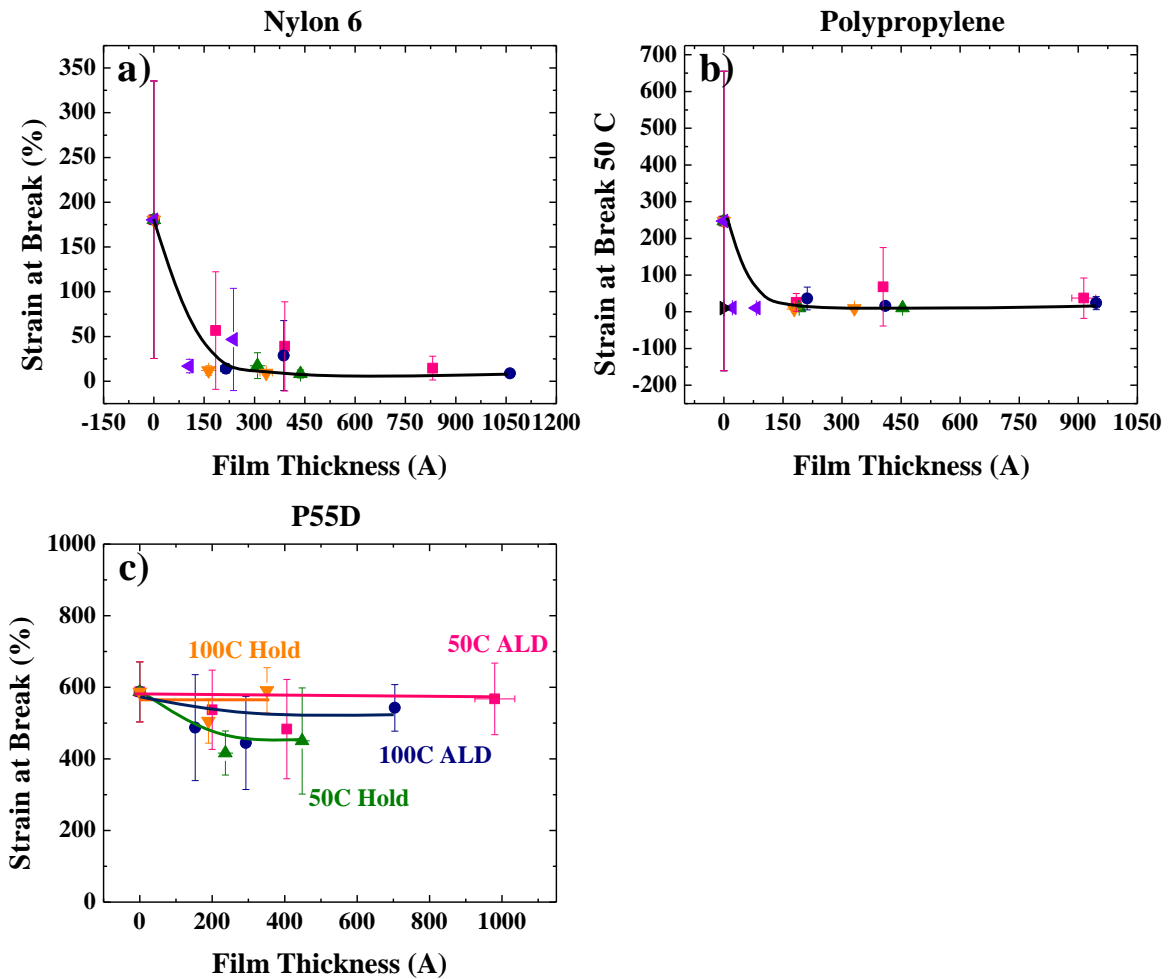


**Figure 8.7:** Strain at break for (a) nylon 6, (b) polypropylene, and (c) P55D for all treatments. The strain at break for nylon 6 and polypropylene has large error bars for the uncoated sample due to necking during testing. As the number film thickness as measured on silicon increased, the occurrence of necking decreased leading to smaller error bars. The aluminum oxide coatings have little effect on the strain at break for the P55D samples indicating that they retain their flexibility.

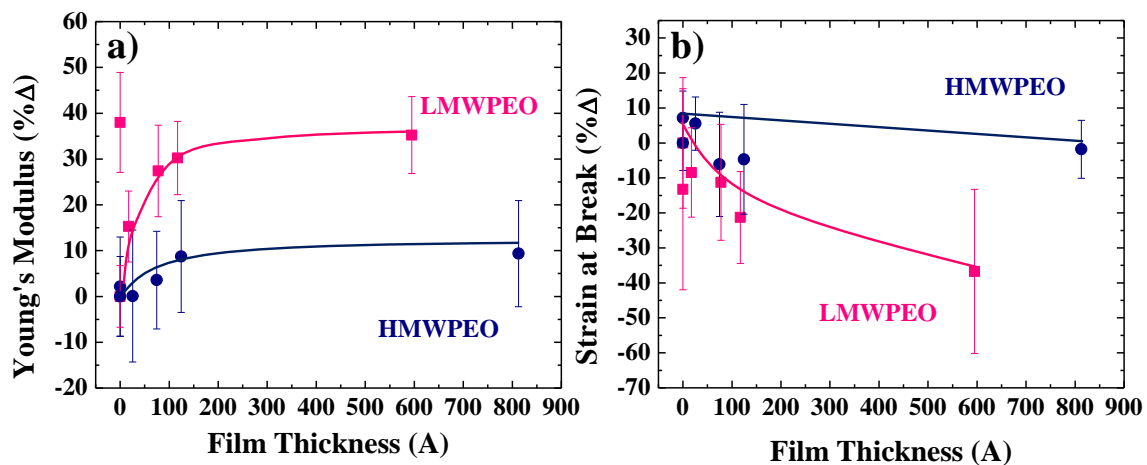


**Figure 8.8:** Percent change in (a) elastic modulus and (b) strain at break for low and high molecular weight PEO. The aluminum oxide increases the modulus and decreases the strain at break for the low molecular weight PEO, but has little effect on the high molecular weight PEO.

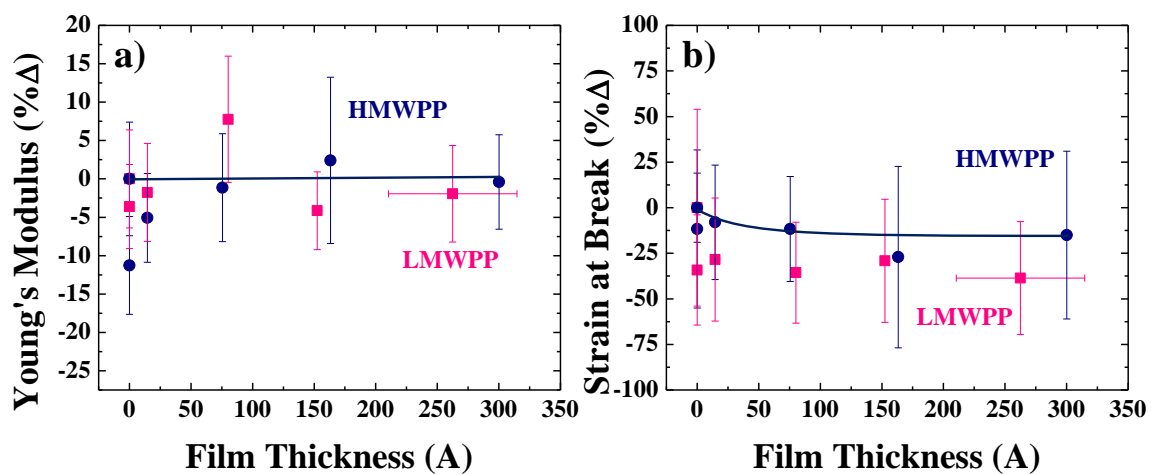


**Figure 8.9:** Percent change in (a) elastic modulus and (b) strain at break for low and high molecular weight PP. Little change in modulus and strain at break is observed for both samples.

**Table 8.3: Mass increase for high molecular PEO samples after treatment with ALD and ~30 minutes after water resistance testing.**

ALD Treatment	% Mass Increase after ALD		% Mass Increase after 30 min	
100 TiO <sub>2</sub>	0.18	0.02	84.81	4.05
25Al <sub>2</sub> O <sub>3</sub> -100TiO <sub>2</sub>	1.15	0.08	103.87	4.89
100 Al <sub>2</sub> O <sub>3</sub> -400 TiO <sub>2</sub>	0.88	0.10	95.54	8.09
200 Al <sub>2</sub> O <sub>3</sub> -600 TiO <sub>2</sub>	0.18	0.02	97.83	9.58

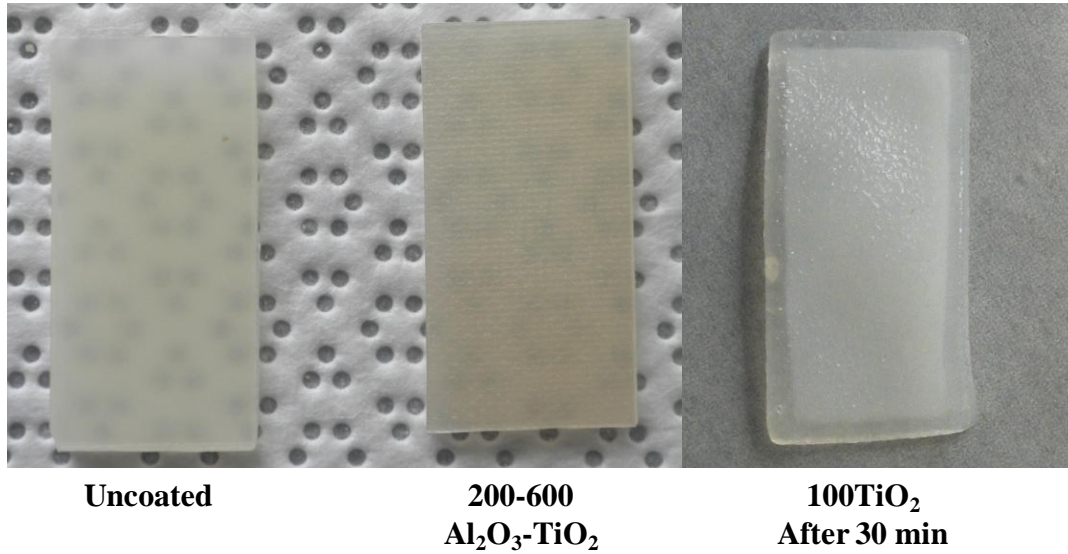


**Figure 8.10:** The uncoated high molecular weight sample for water resistance testing is much lighter than the sample coated with 200 cycles of an aluminum oxide seed layer followed by 600 cycles of titanium dioxide. After water testing the samples swelled

## References

1. M. Minelli, M. G. De Angelis, F. Doghieri, M. Marini, M. Toselli and F. Pilati, *Eur. Polym. J.* **44** (8), 2581-2588 (2008).
2. S. Logothetidis and A. Laskarakis, *Thin Solid Films* **518** (4), 1245-1249 (2009).
3. M. Pagliaro, R. Ciriminna and G. Palmisano, *ChemSusChem* **1** (11), 880-891 (2008).
4. S. R. Wang, Y. F. Kang, L. W. Wang, H. X. Zhang, Y. S. Wang and Y. Wang, *Sens. Actuator B-Chem.* **182**, 467-481 (2013).
5. T. Ogoshi and Y. Chujo, *Compos. Interfaces* **11** (8-9), 539-566 (2005).
6. X. F. Meng, N. Luo, S. L. Cao, S. M. Zhang, M. S. Yang and X. Hu, *Mater. Lett.* **63** (16), 1401-1403 (2009).
7. M. D. Groner, F. H. Fabreguette, J. W. Elam and S. M. George, *Chemistry of Materials* **16** (4), 639-645 (2004).
8. A. A. Dameron, S. D. Davidson, B. B. Burton, P. F. Carcia, R. S. McLean and S. M. George, *J. Phys. Chem. C* **112** (12), 4573-4580 (2008).
9. M. D. Groner, S. M. George, R. S. McLean and P. F. Carcia, *Appl. Phys. Lett.* **88** (5) (2006).
10. W. J. Sweet, J. S. Jur and G. N. Parsons, *J. Appl. Phys.* **113** (19) (2013).
11. J. S. Jur, W. J. Sweet, C. J. Oldham and G. N. Parsons, *Adv. Funct. Mater.* **21** (11), 1993-2002 (2011).
12. G. K. Hyde, G. Scarel, J. C. Spagnola, Q. Peng, K. Lee, B. Gong, K. G. Roberts, K. M. Roth, C. A. Hanson, C. K. Devine, S. M. Stewart, D. Hojo, J. S. Na, J. S. Jur and G. N. Parsons, *Langmuir* **26** (4), 2550-2558 (2010).

13. K. Lee, J. S. Jur, D. H. Kim and G. N. Parsons, *J. Vac. Sci. Technol. A* **30** (1) (2012).
14. Q. Peng, X. Y. Sun, J. C. Spagnola, G. K. Hyde, R. J. Spontak and G. N. Parsons, *Nano Lett.* **7** (3), 719-722 (2007).
15. B. Gong, Q. Peng, J. S. Jur, C. K. Devine, K. Lee and G. N. Parsons, *Chemistry of Materials* **23** (15), 3476-3485 (2011).
16. E. Santala, M. Kemell, M. Leskela and M. Ritala, *Nanotechnology* **20** (3) (2009).
17. J. C. Spagnola, B. Gong, S. A. Arvidson, J. S. Jur, S. A. Khan and G. N. Parsons, *J. Mater. Chem.* **20** (20), 4213-4222 (2010).
18. J. S. Jur, J. C. Spagnola, K. Lee, B. Gong, Q. Peng and G. N. Parsons, *Langmuir* **26** (11), 8239-8244 (2010).
19. H. I. Akyildiz, R. P. Padbury, G. N. Parsons and J. S. Jur, *Langmuir* **28** (44), 15697-15704 (2012).
20. S. M. Lee, E. Pippel, U. Gosele, C. Dresbach, Y. Qin, C. V. Chandran, T. Brauniger, G. Hause and M. Knez, *Science* **324** (5926), 488-492 (2009).
21. C. A. Wilson, R. K. Grubbs and S. M. George, *Chemistry of Materials* **17** (23), 5625-5634 (2005).
22. A. Simmons, J. Hyvarinen, R. A. Odell, D. J. Martin, P. A. Gunatillake, K. R. Noble and L. A. Poole-Warren, *Biomaterials* **25** (20), 4887-4900 (2004).
23. C. J. Oldham, B. Gong, J. C. Spagnola, J. S. Jur, K. J. Senecal, T. A. Godfrey and G. N. Parsons, *J. Electrochem. Soc.* **158** (9), D549-D556 (2011).
24. B. Gong and G. N. Parsons, *J. Mater. Chem.* **22** (31), 15672-15682 (2012).

25. H. Y. Nie, M. Motomatsu, W. Mizutani and H. Tokumoto, *J. Vac. Sci. Technol. B* **13** (3), 1163-1166 (1995).
26. L. M. Bellan, J. Kameoka and H. G. Craighead, *Nanotechnology* **16** (8), 1095-1099 (2005).
27. W. Wang, T. Peijs and A. H. Barber, *Nanotechnology* **21** (3) (2010).

## APPENDIX

## **APPENDIX A1. Co-Authored Works**

### **A1.1 “Sequential Vapor Infiltration of Metal Oxides into Sacrificial Polyester Fibers: Shape Replication and Controlled Porosity of Microporous/Mesoporous Oxide Monoliths”<sup>1</sup>**

In this work I helped with the differential scanning calorimetry (DSC) and thermal gravimetric analysis (TGA) experiments.

### **A1.2 “Stable anatase TiO<sub>2</sub> coating on quartz fibers by atomic layer deposition for photoactive light-scattering in dye-sensitized solar cells”<sup>2</sup>**

My contribution to this work was TEM imaging of the TiO<sub>2</sub> coated quartz fibers.

### **A1.3 “Oxygen Electroreduction on Ti- and Fe-Containing Carbon Fibers”<sup>3</sup>**

My contribution to this work was coating the nanofibers with titanium dioxide using atomic layer deposition.

### **A1.4 “Solid Electrolyte Interphase on Lithium-ion Carbon Nanofiber Electrodes by Atomic and Molecular Layer Deposition”<sup>4</sup>**

My contribution to this work was helping with the ALD coating of the carbon nanofibers.

### **A1.5 “Atomic Layer Deposition Coating of Multi-Walled Carbon Nanotubes with Aluminum Oxide Alters Innate Immune Responses of Human Macrophages In vitro”<sup>5</sup>**

My contribution was depositing the ALD coating on the carbon nanotubes.

## References

1. B. Gong, Q. Peng, J. S. Jur, C. K. Devine, K. Lee and G. N. Parsons, *Chemistry of Materials* **23** (15), 3476-3485 (2011).
2. D. H. Kim, H. J. Koo, J. S. Jur, M. Woodroof, B. Kalanyan, K. Lee, C. K. Devine and G. N. Parsons, *Nanoscale* **4** (15), 4731-4738 (2012).
3. J. P. McClure, C. K. Devine, R. Jiang, D. Chu, J. J. Cuomo, G. N. Parsons and P. S. Fedkiw, *J. Electrochem. Soc.* **160** (8), F769-F778 (2013).
4. A.J. Loebl, C.J. Oldham, C.K. Devine, B. Gong, S.E. Anatosov, G.N. Parsons, and P.S. Fedkiw, *J. Electrochem. Soc.* (under revision)
5. A.J. Taylor, C.K. Devine, J.K. Shipley-Phillips, G.N. Parsons, and J.C. Bonner. *ACS Nano.* (under revision)